National Library of Canada

Bibliothèque nationale du Canada

Acquisitions and Bibliographic Services Branch

Direction des acquisitions et des services bibliographiques

395 Wellington Street
Ottawa, Ontario
K1A 0N4

395, rue Wellington
Ottawa (Ontario)
K1A 0N4

Your file Votre référence

Our file Notre référence

NOTICE

The quality of this microform is heavily dependent upon the quality of the original thesis submitted for microfilming. Every effort has been made to ensure the highest quality of reproduction possible.

If pages are missing, contact the university which granted the degree.

Some pages may have indistinct print especially if the original pages were typed with a poor typewriter ribbon or if the university sent us an inferior photocopy.

Reproduction in full or in part of this microform is governed by the Canadian Copyright Act, R.S.C. 1970, c. C-30, and subsequent amendments.

AVIS

La qualité de cette microforme dépend grandement de la qualité de la thèse soumise au microfilmage. Nous avons tout fait pour assurer une qualité supérieure de reproduction.

S'il manque des pages, veuillez communiquer avec l'université qui a conféré le grade.

La qualité d'impression de certaines pages peut laisser à désirer, surtout si les pages originales ont été dactylographiées à l'aide d'un ruban usé ou si l'université nous a fait parvenir une photocopie de qualité inférieure.

La reproduction, même partielle, de cette microforme est soumise à la Loi canadienne sur le droit d'auteur, SRC 1970, c. C-30, et ses amendements subséquents.

Canada

Opto-Electrical Properties of $In_{1-x}Ga_xAs_yP_{1-y}$ Quaternary Epilayers and Multiple Quantum Wells Lattice Matched to InP

by

Penka Demerdjiev

A thesis

submitted to the Faculty of Graduate Studies and Research

in partial fulfillment of the requirements for the degree of

Master of Science in Physics

Department of Physics

University of Ottawa

150 Louis Pasteur

Ottawa, Ontario

K1N 6N5

©Penka Demerdjiev, Ottawa, Canada, 1995

National Library of Canada

Bibliothèque nationale du Canada

Acquisitions and Bibliographic Services Branch

Direction des acquisitions et des services bibliographiques

395 Wellington Street
Ottawa, Ontario
K1A 0N4

395, rue Wellington
Ottawa (Ontario)
K1A 0N4

Your file Votre référence

Our file Notre référence

The author has granted an irrevocable non-exclusive licence allowing the National Library of Canada to reproduce, loan, distribute or sell copies of his/her thesis by any means and in any form or format, making this thesis available to interested persons.

L'auteur a accordé une licence irrévocable et non exclusive permettant à la Bibliothèque nationale du Canada de reproduire, prêter, distribuer ou vendre des copies de sa thèse de quelque manière et sous quelque forme que ce soit pour mettre des exemplaires de cette thèse à la disposition des personnes intéressées.

The author retains ownership of the copyright in his/her thesis. Neither the thesis nor substantial extracts from it may be printed or otherwise reproduced without his/her permission.

L'auteur conserve la propriété du droit d'auteur qui protège sa thèse. Ni la thèse ni des extraits substantiels de celle-ci ne doivent être imprimés ou autrement reproduits sans son autorisation.

ISBN 0-612-07843-4

Canadä

UNIVERSITÉ D'OTTAWA
UNIVERSITY OF OTTAWA

Abstract

The purpose of this research project is to study the opto-electrical properties of *InGaAsP* quaternary systems. $In_{1-x}Ga_xAs_yP_{1-y}$ epilayers lattice matched to *InP* and $In_{1-x}Ga_xAs_yP_{1-y}/InP$ Multiple Quantum Wells (MQWs) grown by Chemical-Beam Epitaxy (CBE) are being studied systematically using the Photovoltaic (PV) effect. At first, the Schottky barriers on the interfaces (metal-semiconductor, metal-insulator-semiconductor) are determined as an important factor for the electrical and optical properties of the samples. The *Au/InP* and *Au/InGaAsP* barrier heights for the $In_{0.7}Ga_{0.3}As_{0.64}P_{0.36}$ quaternary epilayer are experimentally observed and the values for ϕ_B directly derived from the PV spectra below 200K. The current-voltage (I-V) characteristics for two $Au/In_{0.72}Ga_{0.28}As_{0.68}P_{0.32}/InP$ MQW samples are plotted to evaluate the leakage current contribution to ϕ_B in the formed Schottky contacts. Samples with identical Schottky contact deposition but with an insulating layer on the front surface, have shown much smaller leakage current and yield enhanced barrier heights. Several well-defined spectral structures in the PV spectra of the MQWs, interpreted in terms of sample characteristics, are studied as function of temperature. The photovoltaic signal in the temperature interval 4-300K has maximum amplitude at about 150-180K for the MQW samples and at about 190K for the epilayer. An applied electric field changes the integrated intensity and spectrally shifts the allowed and forbidden transitions observed in bias dependent PV spectra of various *InGaAsP/InP* MQWs. The combined effect of two external factors, the thermal ionization and the electric field on the shape and magnitude of the *11H* exciton peak, are discussed in terms of exciton binding energy and field ionization. The optically induced changes and energy shifting of the *11H* exciton peak are observed, when excitation dependent double beam experiments are conducted on the $In_{0.72}Ga_{0.28}As_{0.68}P_{0.32}/InP$ MQWs. The photomodulation of the internal fields through carrier transport results in observing effective nonlinearities at milliwatt power levels. The

experimentally measured transition energies for the MQWs show good agreement with the envelope wave function calculations. The observed Schottky barrier heights and band gap energies are consistent with the interpolation scheme estimations.

Sommaire

L'objectif de ce travail de recherche est d'étudier les propriétés optiques et électriques des systèmes quarternaires de *InGaAsP*. Des couches épitaxiales de $In_{1-x}Ga_xAs_yP_{1-y}$ sur *InP* et des puits quantiques multiples creés par croissance épitaxiale par jets chimiques sont soumis à une étude systématique en utilisant l'effet photovoltaique. Initialement, les barrières de Schottky aux l'interfaces métal-semiconducteur, métal-isolant-semiconducteur sont determinées comme un facteur important pour les propriétés optiques et électriques des échantillons. Les hauteurs de barrière de *Au/InP* et *Au/InGaAsP* pour la couche épitaxiale $In_{0.7}Ga_{0.3}As_{0.64}P_{0.36}$ sont observées expérimentalment et les valeurs de ϕ_B sont directement dérivées des spectres photovoltaiques au-dessous de 200K. Les caractéristiques courant-voltage (I-V) de deux échantillons de puits quantiques multiples de $In_{0.72}Ga_{0.28}As_{0.68}P_{0.32}/InP$ sont tracées pour évaluer ϕ_B à partir du courant de fuite dans les contacts de Schottky. Les échantillons avec une couche isolante sur la surface avant et une deposition de contact Schottky identique montre beaucoup moins de courant de fuite et donnent des hauteurs de barrière plus élevées. Plusieurs structures spectrales bien definies dans les spectres photovoltaiques des puits quantiques multiples sont interprétées par rapport aux caractéristiques des échantillons et etudiées en fonction de la température. Le signal photovoltaique dans l'intervalle 4-300K a une amplitude maximale aux environs de 150-180K pour les puits quantiques multiples, et 190K pour la couche épitaxiale. Un champ électrique appliqué change l'intensité intégrée et déplace spectralement les transitions permises et interdites observées dans les spectres photovoltaiques. L'effet de deux facteurs externes combinés, l'ionisation thermique et le champ électrique, sur la forme et l'amplitude du pic excitonique *11H*, est discuté par rapport a l'énergie de liason des excitons et de ionisation par champ. Les changements provoqués optiquement et le déplacement énergétique du pic exctonique *11H* sont observés, quand deux faisceaux

lumineux sont incidents simultanément sur les puits quantiques multiples de $In_{0.72}Ga_{0.28}As_{0.68}P_{0.32}/InP$. La photomodulation des champs internes ainsi produite aboutit à l' observation d'effets nonlinéaires au niveau du milliwatt. Les énergies de transition mesurées expérimentalement sont en accord avec les calculs de la fonction d'onde d'enveloppe. Les hauteurs de barrières de Schottky et les énergies de la bande interdite obsevées sont compatible avec les estimations obtenues par interpolation.

Acknowledgments

First of all, I would like to thank Dr. Emery Fortin, without whom the completion of this thesis would not have been possible and express my sincere gratitude for giving me the unique opportunity to work under his supervision in a state of the art lab, for his suggestion of the thesis topic, helpful advices, expertise and help in the course of the project. I am very grateful to Dr. Alain Roth of the Institute of Microstructural Science at NRCC, for providing the *InGaAsP* samples for this study and the computer program for the calculation of the energy transitions of the quaternaries.

I am also thankful to Dr. R. Hodgson and Dr. B. Joos for their understanding and assistance with various matters in the course of my studies. I am appreciative to Mr. Eric Benson and Ms. Geneviève Lafrenière for their help on numerous occasions during the research process and to the staff of the workshops and Department of Physics of the University of Ottawa.

Finally, I wish to express my gratitude to my husband for his continuous encouragement, support and help in completing this project.

Table of Contents

Abstract ii

Sommaire iv

Acknowledgments vi

Table of Contents vii

List of Figures ix

List of Tables xii

Introduction 1

I. Quaternary Compounds 3

1.1 Lattice parameters and composition of $In_{1-x}Ga_xAs_yP_{1-y}$ lattice matched to InP 3

1.2 Band gap variation with composition 6

II. Theoretical background 8

2.1 Quantum Well energy levels 8

2.2 Excitons 14

2.2.1 Excitons in quasi-two dimensional systems 15

2.3 The photovoltaic effect 17

2.4 The effect of an applied electric field on the QW structures 21

2.4.1 Displacement of the spectral structures 22

2.4.2 Selection rules change and appearance of forbidden transitions 23

2.4.3 Broadening of the excitonic peaks 24

2.4.4 Ionization of the exciton 24

2.5 The effect of temperature on the optical transitions 25

2.5.1 Temperature dependence of the optical transitions 26

2.5.2 The effect of electron-phonon interactions 26

2.5.3 Excitonic effects: temperature dependence 27

III. Experimental techniques 29
3.1 Sample preparation 29
3.2 The Photovoltaic experiment 33
3.3 The double beam experiment 36
3.4 Temperature control of the sample 37
IV. Experimental results and discussions 38
4.1 Measuring the Schottky-barrier heights 38
4.1.1 The Schottky-barrier heights of the $Au/In_{0.7}Ga_{0.3}As_{0.64}P_{0.36}$ epilayer 39
4.1.2 The Schottky-barrier heights of the $Au/In_{0.72}Ga_{0.28}As_{0.68}P_{0.32}/InP$ MQWs 42
4.2 PV spectra at different temperatures 47
4.2.1 *InP* substrate: the PV signal evolution with temperature 47
4.2.2 *InGaAsP* epilayer: temperature dependence of the PV signal 49
4.2.3 *InGaAsP/InP* MQW: temperature dependence of the PV signal 51
4.3 Field dependent effects 58
4.3.1 Electric field dependence of the QW peaks 59
4.3.2 The integrated photovoltaic signal as function of the applied voltage and temperature 68
4.4 The double beam experiment 71
V. Conclusions 78
VI. References 80

List of Figures

1.1. Three dimensional representation of the lattice constant. The bold line covers the region where the quaternary is lattice matched to *InP* 5

1.2. Three dimensional representation of the $In_{1-x}Ga_xAs_yP_{1-y}$ energy gap. The dotted curve covers the band gaps for compositions lattice matched to *InP* 6

2.1. Schematic views of a single and a multiple quantum well 9

2.2. Energy profile of a square well 10

2.3. a.-Possible electron-hole transitions in a quantum well; b.-Possible electron-hole transitions as a result of splitting between heavy and light hole states 13

2.4. Metal/n-type semiconductor energy band diagram: a.-thermal equilibrium; b.-forward bias; c.-reverse bias 18

2.5. The effect of an applied electric field on the QW energy levels and wave functions 22

3.1. Schematic views of: a.-the *InGaAsP* quaternary epilayer, sample 4 and b.-*InGaAsP/InP*MQWs, samples 1 and 2 30

3.2. Schematic view of sample 3 30

3.3. Electrical contacts for: a.-the epilayer and b.-a typical MQW 31

3.4. Set-up diagram for the PV experiment 34

3.5. Schematic view of the bias unit 35

3.6. Schematic view of the set-up for I-V measurements 35

3.7. Set-up diagram for the double beam experiment 36

4.1. PV spectra for the epilayer in the band gap region 39

4.2. PV spectra for the epilayer in the region of the barrier heights 40

4.3. Barrier heights of: a.-*Au/InP* and b.-*InGaAsP* at 96K and 160K 41

4.4. Current-voltage characteristics of: a.-*Au* Schottky diodes made on sample 1 at 212K and 300K; b.-expanded linear region, sample 1 at 212K and 300K 43

4.5. Current-voltage characteristics for sample 2 at 212K and 300K 45

4.6. Expanded linear region of the current-voltage characteristics, sample 2: a.-at 212K and b.-at 300K 46

4.7. PV spectra of the *InP* substrate at 22K, 96K, and 300K 48

4.8. Spectral response of $In_{0.7}Ga_{0.3}As_{0.64}P_{0.36}$ epilayer lattice matched to *InP* (sample 4) 50

4.9. Temperature variation of the direct band gap of the epilayer 51

4.10. PV spectra of $In_{0.72}Ga_{0.28}As_{0.68}P_{0.32}/InP$ MQW in the 4K-129K temperature interval (sample 1) 52

4.11. PV spectra of $In_{0.72}Ga_{0.28}As_{0.68}P_{0.32}/InP$ MQW in the 159K-275K temperature interval (sample 1) 53

4.12. PV spectra of $In_{0.68}Ga_{0.32}As_{0.56}P_{0.44}/InP$ MQW at 100K and at 300K (sample 3) 55

4.13. Position shift of the spectral structures observed in the PV spectra of sample 1(MQWs) 56

4.14. Excitonic *11H* peak shift with temperature for sample 1 (MQW) 57

4.15. Field dependence of the PV spectra structures of sample 1 at: a.-at 200K and b.-at 96K 60

4.16. The effect of an applied electric field on the PV spectra in the *11H* excitonic region at 212K for sample 1 61

4.17. The effect of an applied electric field on the PV spectra in the *11H* excitonic region for sample 1: a.-at 96K and b.-at 300K 62

4.18. Broadening of the excitonic *11H* peak of sample 1 at 212K 63

4.19. Position shifts of the excitonic *11H* peak with an applied electric field for sample 1 at 96K 64

4.20. Position shifts of the excitonic *11H* peak with an applied electric field for sample 1 at 212K 64

4.21. The effect of an applied electric field on the *11H* excitonic peak for sample 2 at: a.-at 300K and b.-at 212K 66

4.22. PV signal of sample 3 for different applied voltages 67

4.23. PV signal maximum at the *11H* peak of sample 1 as function of the applied voltage 68

4.24. Area change of the excitonic *11H* peak with an applied voltage for sample 1 at 96K, 212K and 300K 69

4.25. Area change of the excitonic *11H* peak with temperature, at zero applied voltage for sample 1 70

4.26. The excitonic *11H* peak dependence on the pump beam intensity for sample 1 a.-212K and b.-300K; i-I=6mW/cm^2; ii-I=13mW/cm^2; iii-I=0.13W/cm^2; iv-I=1.3W/cm^2 73

4.27. PV signal dependence on the pump beam intensity for: a.-sample 1 and b.-sample 2 74

4.28. The open-circuit PV signal vs. the illumination intensity $I_{tr}=I/I_o$, where I_o is the intensity given by the 10mW *He-Ne* laser, a.-sample 1; b.-sample 2 75

4.29. The *11H* excitonic peak dependence on the pump intensity for sample 2: a.-212K; i-I=3mW/cm^2; ii-I=33mW/cm^2; iii-I=0.33W/cm^2; iv-I=.82W/cm^2 ; v-I=1.3W/cm^{2}and b.-300K i-I=3mW/cm^2; ii-I=13mW/cm^2; iii-I=0.41W/cm^2; iv-I=1.3W/cm^2. 76

List of Tables

3.1. Sample characteristics 32

4.1. Summarized barrier heights of the quaternary epilayer and the MQWs 47

4.2. Positions and identification of the experimental and calculated values for the energy transitions of sample 1 54

4.3. Spectral features identification of sample 3 55

Introduction

The recent advances in ultrathin structure preparation techniques have made possible the production of new electronic semiconductor devices with higher performance, based on variations of the potential in series of barriers and wells, along a direction perpendicular to the layers of growth. All of these semiconductor quantum heterostructures can be designed with the desired physical properties by adjusting the composition of the materials and the thickness of the layers. The research and development of device fabrication have also been extended from III–V binary and ternary to III-V quaternary systems, which offer the possibility to independently control the band gap and the lattice constant with minimum lattice mismatch. Since the early 1970s, when the first growth of $In_{1-x}Ga_xAs_yP_{1-y}$ lattice matched to InP was realized[1], the quaternary systems has attracted great interest and become widely used in various applications, such as lasers, light emitting diodes, photo-detectors etc. The reasons for $InGaAsP$ being so attractive for device fabrication are:

- the possibility to change the composition y over a wide range of band gaps varying from 1.35eV (.92μm) to .75eV (1.65μm)
- the spectral range of the band gaps contains the region of lowest loss and dispersion for optical fibers presently used in communications
- the possibility to grow well controlled thin films and multiple quantum well structures.

A number of opto-electronic and transport devices based on the semiconducting quaternary $In_{1-x}Ga_xAs_yP_{1-y}$ have previously been reported [2-7], however the physical properties of this system are the object of many recent studies[8-14]. The research on the excitonic effects in $In_{1-x}Ga_xAs_yP_{1-y}$ based MQWs has been conducted using electroabsorption and photoconductivity techniques[2,6,12]; the electric field effects on lattice matched $InGaAsP/InP$ QWs have been studied and the Stark shift on the ground state exciton has been measured[2, 12]. Experimental research, interpolation with the

material parameters for the related binaries *InP*, *InAs*, *GaAs*, and *GaP* has been used to obtain their various physical parameters[15-18]. Although the interpolation scheme is an approximation, it still provides useful material parameters over a wide range of alloy compositions. Based on it, the band gap variations are extrapolated[18] and different optical constants calculated[16, 17].

This study does a parallel research on the opto-electrical properties of *InGaAsP* quaternaries, with emphasis on the opto-electrical and carrier transport properties of the excitons in various $In_{1-x}Ga_xAs_yP_{1-y}/InP$ MQWs. We use the photovoltaic detection as a fairly simple and powerful method to study the photovoltaic signal as function of temperature, the external electric field, and the varied intensity excitation in *InGaAsP* quaternaries.

The thesis is organized in five chapters. The first chapter briefly describes the lattice constant variation with x and y composition, based on Vegard's law for *InGaAsP* lattice matched to *InP* system and discusses the energy band gaps of $In_{1-x}Ga_xAs_yP_{1-y}$ quaternaries and their dependence on the binaries composition. The second chapter gives a theoretical evaluation of the energy levels as well as the exciton binding energy in quasi-bidimensional structures. It also reviews the theory of the photovoltaic effect used to study the Quantum Well (QW) transitions and the effect of an applied electric field on the energy levels. The description of the samples, the preparation techniques and the experimental methods used to analyze them are outlined and discussed in the third chapter as experimental techniques. In the fourth chapter, the experimental results are presented and analyzed. The experimental data collected for the quaternary epilayer, the slightly mismatched sample and the lattice matched samples with same x and y composition, but different contact deposition is compared and the possibilities for future device applications discussed.

I. Quaternary Compounds

The quaternary material $A_{1-x}B_xC_yD_{1-y}$ is constructed of four binary compounds *AC*, *AD*, *BC*, and *BD*, using an interpolation scheme. Thus, the quaternary material parameter Q, as a function of the quaternary alloy composition (x,y) can be formulated as a combination of the constituent binaries:

$$Q(x,y) = (1-x)yB_{AC} + (1-x)(1-y)B_{AD} + xyB_{BC} + x(1-y)B_{BD} \qquad (1.1)$$

This interpolation relation is used to derive different material parameters of the quaternaries by giving B_{ij} some physical basis (such as band gap, lattice constant, deformation potential, etc.).

If we consider the binary material parameters of *GaAs*, *InP*, *InAs*, and *GaP*, then from eq.(1.1), the quaternary parameter $Q(x,y)$, of $In_{1-x}Ga_xAs_yP_{1-y}$ will be:

$$Q(x,y) = (1-x)yB_{InAs} + (1-x)(1-y)B_{InP} + xyB_{GaAs} + x(1-y)B_{GaP} \qquad (1.2)$$

Equation (1.2) will be considered for the theoretical evaluation of some of *InGaAsP* parameters and compared with the experimental results.

1.1 Lattice parameters and composition of $In_{1-x}Ga_xAs_yP_{1-y}$ lattice matched to *InP*

The term "lattice matching" means that both materials *InGaAsP* and *InP* have the same lattice constant and expansion coefficient. In multilayered semiconducting structures, where very thin epitaxial films are deposited , it is of great importance to obtain small or no mismatch between the layers. All of their optical and electrical properties depend on the quality of the heteroepitaxial growth. The effect of lattice mismatch strain can be considered as reasonable, if $\left|\frac{\Delta a}{a_q}\right| \leq 0.2\%$ [18],where a_q is the lattice constant of the quaternary and Δa is the difference $|a_{InGaAsP} - a_{InP}|$.

The lattice constant a_q for the quaternaries is known to obey Vegard's law for lattice matched systems, i. e. to vary linearly with the alloy composition, and can be deduced from that of the former binaries. For $In_{1-x}Ga_xAs_yP_{1-y}$ (using eq.1.2), we obtain:

$$a_q(x,y) = (1-x)ya_{InAs} + (1-x)(1-y)a_{InP} + xya_{GaAs} + x(1-y)a_{GaP}. \qquad (1.3)$$

Taking the following binary constants from ref. 18: a_{InAs}=6.0584Å, a_{GaP}=5.412Å, a_{GaAs}=5.6535Å, and a_{InP}=5.86875Å, eq.1.3 is reduced to:

$$a_q(x,y) = 0.1896y - 0.4176x + 0.0125xy + 5.86875 \ \mathring{A}. \qquad (1.4)$$

The lattice matching relation between x and y compositions then can be written as:

$$x = \frac{0.1896y}{0.4176 - 0.0125y}, \quad (0 \le y \le 1). \qquad (1.5)$$

For the lattice matched MQWs (x=0.28, and y=0.68) in our study we find $\left|\frac{\Delta a}{a_q}\right| \le 0.24\%$ at 300K, which is on the limits of lattice matched samples. The epilayer (x=0.3, y=0.64) is a structure relatively easier to grow and shows almost perfect lattice match of $\left|\frac{\Delta a}{a_q}\right| \le 0.026\%$ at 300K. For one of the MQW sample we have studied (x=0.32, y=0.56) the lattice mismatch is bigger: $\left|\frac{\Delta a}{a_q}\right| \le 0.43\%$ at 300K, which shows that it is strained.

The statement of Vegard's law appears to be valid for the *InGaAsP* quaternary over the range of compositions $0 \le x \le 0.47$, $0 \le y \le 1$. Figure 1.1 shows a three-dimensional representation of the lattice constant a_q, over this range.

The second parameter playing an important role in the fabrication and performance of *InGaAsP* heterostructures is the thermal expansion coefficient α. A small fraction of mismatch caused by the difference in α for the different layers is present in most growth conditions. S. Adachi[19, p.54] has derived the dependence of this difference with the y composition, which is: $\alpha_q - \alpha_{InP} = 1.18y$, where α_q is the thermal expansion coefficient of the quaternary, and $\alpha_{InP} = 4.56 \times 10^{-6} C^{\circ -1}$. Therefore for the most studied composition

in this research (y=0.68), the thermal expansion coefficient for the quaternary is $\alpha_q=5.36\times10^{-6}C^{o-1}$. Assuming a linear relation between the lattice constant and the temperature, the dependence of the lattice constant on the thermal expansion coefficient can be formulated as[20, p.55]:

$$a_q(T) = a_q(0)(1+\alpha_q T), \tag{1.6}$$

where a_q(T) is the lattice constant at any given temperature and a_q(0) is the lattice constant at 0K. Considering eq.(1.4) and eq.(1.6), for $In_{0.72}Ga_{0.28}As_{0.68}P_{.32}/InP$ MQW (sample 1), the lattice mismatch is smaller at lower temperatures , of the order of $\left|\frac{\Delta a}{a_q}\right| \leq 0.1\%$ at 4K.

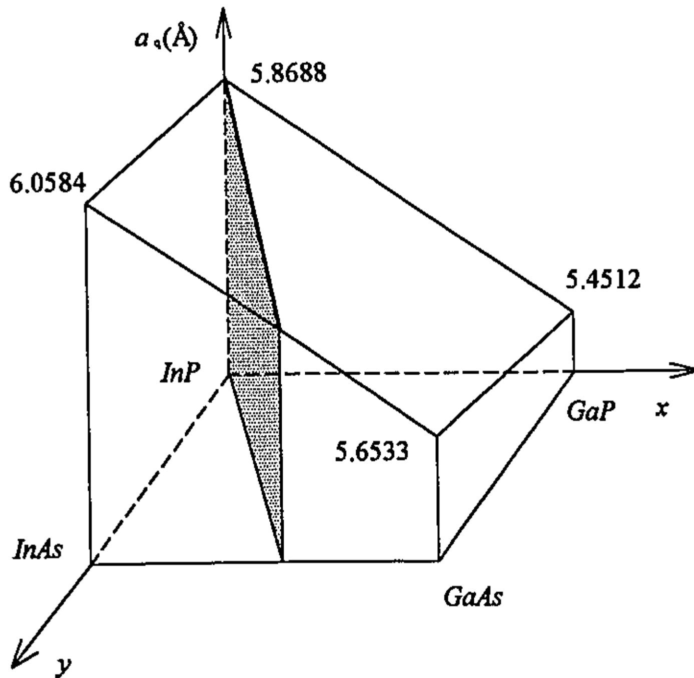

Fig. 1.1 Three dimensional representation of the lattice constant. The bold line covers the region where the quaternary is lattice matched to InP.

1.2 Band gap variation with composition

Extending to further simplification the relation between x and y for lattice matched system, relation (1.5) can be given in the approximated form [19, p.5]:

$$x = 0.47y, \quad (0 \le y \le 1) \tag{1.7}$$

Then combining eq.(1.4) and eq.(1.7) with a good degree of accuracy the quaternary material parameter can be written:

$$Q(x,y) = Q(y) = a + by + cy^2, \tag{1.8}$$

where a and b are determined by the end-point materials and c is the bowing parameter. The bowing is a measure of the change in the crystal potential across the alloy field. The direct band gap energy E_g is the most important parameter for device application. The variation of the band gap energy with composition (from eq.(1.8) may be written in the form:

$$E_g(y) = a + by + cy^2 \tag{1.9}$$

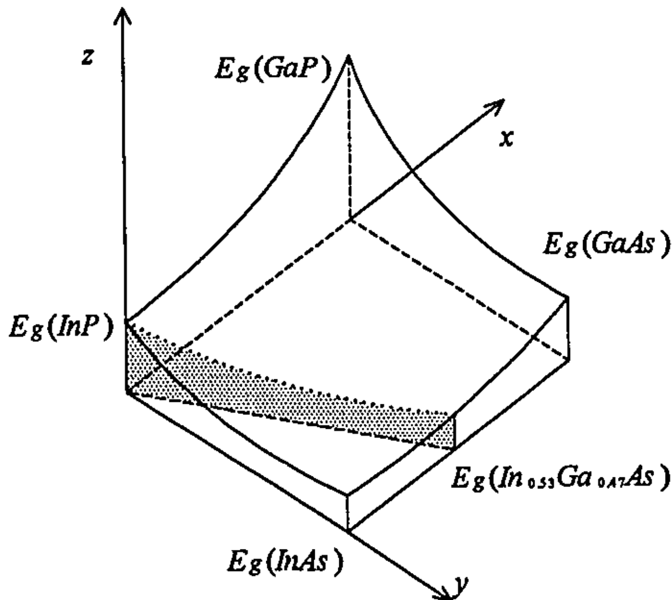

Fig. 1.2 Three dimensional representation of the $In_{1-x}Ga_xAs_yP_{1-y}$ energy gap. The dotted curve covers the band gaps for compositions lattice matched to InP.

The E_g gap for $InGaAsP$ lattice matched to InP has been measured by different techniques such as photoluminescence [21], electroreflectivity [22], and summarized by S. Adachi (ref.19, p.81), and the experimental data fitted to the relation:

$$E_g(y) = 1.35 - 0.72y + 0.12y^2, \quad eV \qquad (1.10)$$

For the MQW (sample 1) with y=0.68, eq.(1.10) gives $E_g(0.68)=0.916eV(1.350\mu m)$ at 300K. For the quaternary epilayer $E_g(0.64)=0.938eV(1.318\mu m)$ at 300K. The comparison of these results to our experimental values of $E_g(0.68)=0.915eV(1.351\mu m)$ and $E_g(0.64)=0.903eV(1.369\mu m)$ respectively, shows reasonable agreement with the approximated general relation.

A visualized model of the three-dimensional surface of the band gap energy E_g versus x and y is shown in fig.1.2. The corners represent the direct gaps of the binaries: E_g(InP), E_g(InAs), E_g(GaP), E_g(GaAs), and the curves can be obtained from the interpolation scheme using equation(1.1). The dotted curve connecting the band gaps of InP and $In_{0.53}Ga_{0.47}As$ represents the lattice matched quaternary system.

II. Theoretical background

This chapter reviews the theoretical background necessary for understanding the opto-electrical properties of layered semiconductor heterostructures. The envelope function approximation method is being used to calculate the energy levels of the quantum wells. For the theoretical calculations we consider a model with finite potential barriers and give analytical solutions for the energy levels of a well with a given width. We also discuss the excitonic effects in two-dimensional systems and show that the binding energy of the two-dimensional exciton may be up to four times larger than in the three-dimensional case. This energy increase becomes important when the thickness of the well is less than the bulk exciton diameter. The basic concepts of the photovoltaic effect are outlined and the dependence of the photogenerated current on the absorption coefficient derived. At the end of this chapter we show the influence of an external electric field on the ground state exciton and discuss the related Quantum Confined Stark effect. The relations giving the temperature dependence of the band gap and the exciton in QWs are also outlined.

2.1. Quantum well energy levels

The fabrication of semiconductor quantum heterostructures has three basic configurations: a single heterojunction separated by an interface, a single quantum well, and a multiple quantum well, or a superlattice. By adjusting the composition and thicknesses of the layers, these configurations can be designed with the desired optical properties. A single quantum well consists of ultrathin layer with thickness of $d_W \leq 100$Å, sandwiched between thicker layers (d_B) of a semiconductor with larger band gap ($d_W << d_B$). A multiple quantum well is formed as an array of barriers and wells with a total number N ($d_W << d_B$) and displays the optical properties of a single quantum well, except

that the optical density of the structure along the growth axis z is multiplied by the number of periods, N -fig.2.1. Another important class of thin heterostructures is the superlattice, which consists of ultrathin layers of wells and barriers. In superlattices, the electronic wave functions of the wells overlap and their properties differ from those of MQWs. All these structures with reduced dimensionality, offer the possibility of adjusting their optical properties for different practical applications[23].

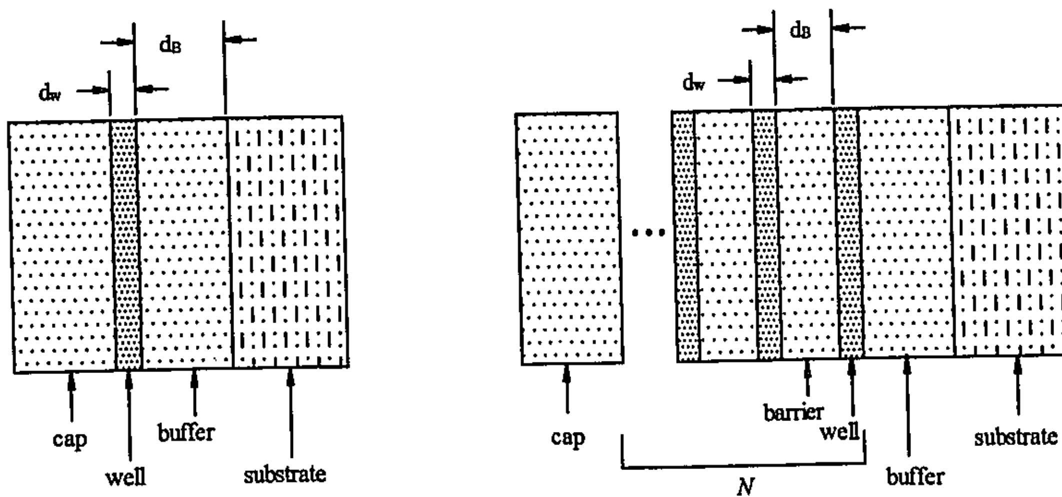

Fig.2.1 Schematic views of a single and a multiple quantum well.

For the interpretation of the experimental findings, the knowledge of the energy structure is necessary. To describe the electronic states in quantum wells and superlattices, different methods were developed in the 1980s. They can be summarized as tight-binding calculations[24], pseudo-potential formalism[25], and envelope function approximation[26,27]. In our study we use the envelope function approximation as an accurate and flexible method to describe the electronic states in QWs. Since it has been reviewed before, in the following section we outline its statements without going into deep discussions.

To derive the energy states in the QW we will consider a rectangular quantum well with finite barrier heights . A semiconductor heterostructure formed by material A is sandwiched between two layers of material B with band gap energy larger than A. A and B are assumed to be perfectly lattice matched and to have the same crystallographic structure -fig.2.2. In this theoretical model the matching for *InGaAsP* is considered to be perfect. In the envelope function description, the problem is finding the boundary condition of the slowly varying wave functions of the heterostructures, taken as identical in both host materials. Then the electron wave function will have approximately the form[26 p.67]:

$$\Psi = \sum_{A,B} e^{ik_\perp \cdot r} u_{ck}^{A,B}(r)\chi_n(z), \tag{2.1}$$

where $u_{ck}(r)$ is the Bloch function in material A or B, z is the growth direction, $k_\perp$ is the transverse electron wave vector, and $\chi_n(z)$ is the envelope wave function, considering the potential in the well as given by:

$$V(z) = \begin{cases} 0, & |z| < \frac{L_z}{2} \\ V_o, & |z| > \frac{L_z}{2} \end{cases}, \tag{2.2}$$

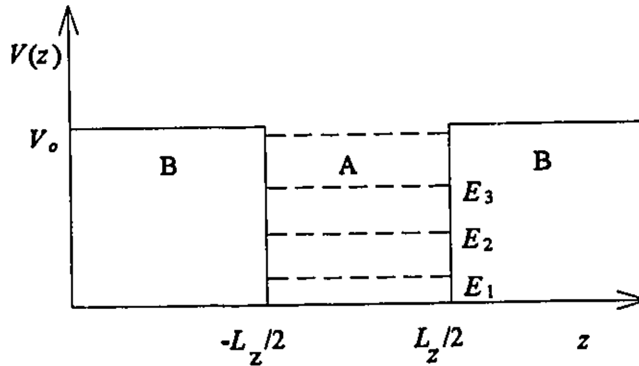

Fig.2.2 Energy profile of a square well.

where L_z is the thickness of the quantum well, the Schrödinger equation describing the motion of the particles along z, can be written as:

$$\left[-\frac{\hbar^2}{2m^*}\cdot\frac{\partial^2}{\partial z^2}+V(z)\right]\chi(z)=E\chi(z), \tag{2.3}$$

where m^* is the electron effective mass, E is the confinement energy of the carrier. $\chi(z)$ is continuous everywhere and $\lim_{z\to\pm\infty}|\chi(z)|$ is finite. Since $V(z)$ has a known value, the solutions of eq.2.1 can be obtained. For both cases in eq.2.1, $\chi(z)$ is the sum of the two plane waves with opposite wave vectors. Inside the wells, where $V(z)$=0, these vectors are $\pm k_A$:

$$k_A=\sqrt{\frac{2m_A^*}{\hbar^2}E} \tag{2.4}$$

Outside the well, $V(z)=V_0$ and the vectors are $\pm k_B$:

$$k_B=\sqrt{\frac{2m_B^*}{\hbar^2}(V_0-E)} \tag{2.5}$$

In the case of a symmetric potential the wave function $\chi(z)$ can be chosen either even or odd, then for both types of states, inside the wells $\chi(z)$,the solutions of eq. 2.3 can be written:

$$\chi(z)=B\cos k_A z,\ \textit{for even states} \tag{2.6}$$

$$\chi(z)=A\sin k_A z,\ \textit{for odd states,} \tag{2.7}$$

where A and B are constants. Outside the well, the wave functions $\chi(z)$ have to be normalized and $|\chi(z)|$ not to diverge, when $z\to\pm\infty$, and the solutions are:

$$\chi(z)=Ce^{-k_B z},\ \textit{for even states} \tag{2.8}$$

$$\chi(z)=De^{k_B z},\ \textit{for odd states,} \tag{2.9}$$

where C and D are constants. The relations between both wave vectors k_A and k_B are:

$$\frac{1}{m_A^*}k_A\tan\left(k_A\frac{L_z}{2}\right)=\frac{1}{m_B^*}k_B,\ \textit{for even states} \tag{2.10}$$

$$\frac{1}{m_A^*} k_A \cot\left(k_A \tfrac{L_z}{2}\right) = \frac{1}{m_B^*} - k_B, \text{ for odd states} \tag{2.11}$$

Inserting the values for k_A and k_B from eq.2.5 and eq.2.6 to eq.2.9 and eq.2.10, the discrete values of the energy *E*, are:

$$\tan\left(\sqrt{\frac{2m_A^* E}{\hbar^2}}\frac{L_z}{2}\right) = \sqrt{\frac{m_A^*}{m_B^*}\left(\frac{V_o}{E}-1\right)}, \text{ for even states} \tag{2.12}$$

$$\cot\left(\sqrt{\frac{2m_A^* E}{\hbar^2}}\frac{L_z}{2}\right) = -\sqrt{\frac{m_A^*}{m_B^*}\left(\frac{V_o}{E}-1\right)}, \text{ for odd states} \tag{2.13}$$

The last two equations give the dependence of the energy of the bound and continuum states on the width of the quantum well with a particular V_O chosen. The energy eigenvalues *E*, may be determined from eq.2.12 and eq.2.13 if we know the effective masses m^*_B and m^*_A , V_O and L_Z.

The above expressions are obtained under the assumption of nondegenerate bands for both electrons and holes and the allowed transitions being those, that occur between a quantized electron and a hole states with the same quantum number *j* (Δj=0)- fig.2.3a.. In quantum wells the conduction band electron energy states are similar to eq.2.12 and eq.2.13., but the valence band is degenerate at k=0, which makes more complicated the energy and wave functions associated with them. The upper two states of the valence band can be referred to, as heavy and light hole bands. Since any perturbation can lift the degeneracy, there are different confinement energies and the heavy and light hole states split in two sets of levels. Also when the perturbation breaks the symmetry of the system, the selection rules are relaxed, transitions can occur from either of the hole states to the conduction band; thus transitions with different quantum number $\Delta j \neq 0$ may become allowed- fig.2.3b. This is the case for instance when an electric field perpendicular to the layers is present in the quantum wells. The splitting decreases with the increase in the thickness of the well and can not always be optically observed. The light and heavy hole

components are easily observed in narrow well QW samples, where the exciton binding energy is larger and the Bohr radius smaller.

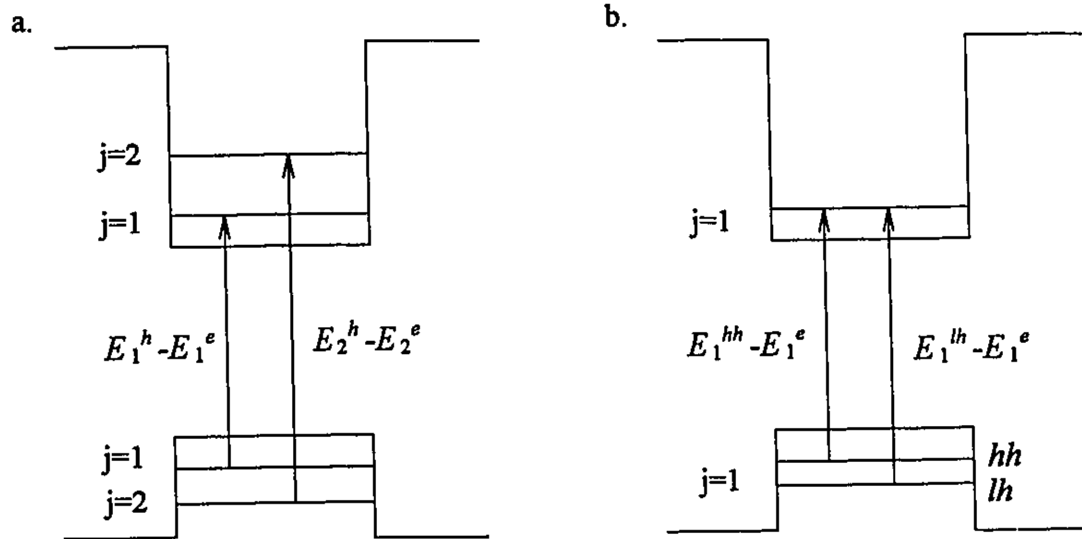

Fig.2.3 a.-Possible electron-hole transitions in a quantum well; b.-Possible electron-hole transitions as a result of splitting between heavy and light hole states.

By applying eq.(2.12) and eq.(2.13) to a *InGaAsP* quaternary system, the energy levels for different transitions at any given temperature can be obtained. In our case for *InGaAsP/InP* MQWs, where x=0.28 and y=0.68 and the well width is L=80Å, computer program calculations give the possible transitions at 4K with the following energies[28]:

11H - 998 meV

11L - 1042 meV

21H - 1116 meV

12L - 1154 meV etc.

Here *11H* means a transition from the first electron state, E_1^e, to the first heavy hole state, E_1^{hh}, *11L* is a transition from the first electron state, E_1^e, to the first light hole state-E_1^{lh}. Later, in the experimental part the observed transitions will be compared to the calculated results.

2.2 Excitons

The concept of excitons in semiconducting crystals has been the subject of considerable interest in the past [29-33]. In general, optical transitions in undoped semiconductors are dominated by the electron-hole Coulomb interaction, forming bound electron-hole pairs, called excitons. The existence of pronounced narrow peaks in the lower energy side of the band gap in the absorption spectrum is evidence of the excitonic nature of the various transitions. Therefore, the process of absorption of a photon corresponds to the creation of an exciton, which can move as a whole through the crystal with zero net charge transfer. An exciton has a set of energy levels analogous to those in a hydrogen atom, with a binding energy of a few millielectron volts. This slightly reduces the energy of the excited state and explains why less photon energy is required for the exciton transition than for band to band transitions.

The effects of the formation of exciton states are most directly observed in the optical properties of a crystal in the vicinity of its various absorption edges. In the following section we will consider the theory of excitons involving the electron and hole interaction, without discussing in detail the framework of the theory, which is thoroughly reviewed in ref.30. The envelope function, Ψ_{ex}, describing the electron and hole motion and the influence of all other atoms is a solution of the two-particle Schrödinger equation:

$$\left(-\frac{\hbar^2}{2m_e^*}\nabla_e^2-\frac{\hbar^2}{2m_h^*}\nabla_h^2-\frac{e^2}{\varepsilon(0)|r_e-r_h|}\right)\Psi_{ex}=E_n\Psi_{ex}, \tag{2.14}$$

where $\varepsilon(0)$ is the static dielectric constant of the crystal, m_e^* and m_h^* are the effective masses of the electron and hole, respectively, and $|r_e-r_h|$ is the distance of separation. The solutions of equation (1.14) give a series of bound states with energies:

$$E_n=E_g-\frac{R_{ex}}{n^2},\quad n=1,2,3,..., \tag{2.15}$$

where R_{ex} is the exciton Rydberg energy given by:

$$R_{ex} = \frac{\hbar^2}{2m_{ex}^* a_{o_{ex}}^2}, \quad eV \qquad (2.16)$$

and the exciton Bohr radius, $a_{o_{ex}}^2$,is:

$$a_{o_{ex}}^2 = \frac{\varepsilon(0)\hbar^2}{m_{ex}^* e^2}, \quad \mathring{A} \qquad (2.17)$$

where ε(0) is the static dielectric constant, and m_{ex}^* is the exciton reduced mass written by:

$$\frac{1}{m_{ex}^*} = \frac{1}{m_e^*} + \frac{1}{m_h^*} \qquad (2.18)$$

The exciton makes a dominant contribution to the band edge of the PV spectrum , which we discuss in the experimental section 4.3.2.

2.2.1 Excitons in quasi-two-dimensional systems

In QWs, in contrast to bulk materials, the excitons are confined to the direction perpendicular to the layers. This confinement makes the excitonic effects stronger in QWs. The total Hamiltonian for the relative motion of the electron-hole pairs can be written[34,p.210]:

$$H = -\frac{\hbar^2}{2m_e^*}\nabla_e^2 - \frac{\hbar^2}{2m_h^*}\nabla_h^2 + V_{conf} + V_{Coulomb}, \qquad (2.19)$$

where the first two terms are the kinetic energy of the electron and the hole, $V_{Coulomb}$ is the Coulomb potential, and V_{conf} is the confinement potential. The two-dimensional Schrödinger equation associated with this Hamiltonian, has solutions in the plane perpendicular to the layers as a series of bound excitonic lines at positions [35, p.70]:

$$E_n^{2D} = h\nu^{h,e,i,j} = E_g + E_{conf}^{h,e,i} + E_{ex} \qquad (2.20)$$

Prominent peaks are those with $i=j$, then eq.(2.20) becomes:

$$E_n^{2D} = E_g + \frac{\hbar^2 \pi^2 j^2}{2m_{ex}^* L_z^2} - \frac{R_{ex}}{\left(n_j - \frac{1}{2}\right)^2}, \quad j = 1,2,3,... \tag{2.21}$$

where R_{ex} is the three-dimensional exciton Rydberg energy, given by eq.(2.16), and the second term is the confinement energy of the electron - hole pair, where m_{ex}^* is the reduced exciton mass.

In comparison to the three-dimensional binding energy, the two-dimensional binding energy will result from the substitution of $n \rightarrow n - \frac{1}{2}$ in eq.(2.15):

$$R_{ex}^{2D} = \frac{R_{ex}}{\left(n - \frac{1}{2}\right)^2} \tag{2.22}$$

We can see that the lowest two-dimensional exciton energy associated with n=1 may be up to four times larger in a two-dimensional system, than it is in a three dimensional one:

$$R_{ex,n=1}^{2D} = 4R_{ex,n=1}^{3D} \tag{2.23}$$

This effect becomes important, when the thickness of the well is less than the bulk exciton radius. Equation(2.23) also shows that the exciton ground state in the two-dimensional case is farther from the band gap than in the three dimensional one:

$$E_n^{2D} = E_g - \frac{R_{ex}}{(n - \frac{1}{2})^2}, \quad \text{n} = 1,2,3,... \tag{2.24}$$

From eq. (2.17) and eq. (2.23) the 2D Bohr radius will be:

$$a_{o_{ex}}^{2D} = \frac{a_{o_{ex}}^{3D}}{2} \tag{2.25}$$

In the calculations above for simplicity, we have assumed that the static dielectric constants of the well $\varepsilon(0)_w$, and the barrier $\varepsilon(0)_B$, are the same. However, when $\varepsilon(0)_w > \varepsilon(0)_B$, the two dimensional binding energy will have the form[34, p.213]:

$$R_{ex}^{2D} = \left(\frac{\varepsilon(0)_w}{\varepsilon(0)_B}\right)^2 \frac{R_{ex}}{(n - \frac{1}{2})^2}, \tag{2.26}$$

and the increase in the exciton binding energy can be considerable. We will demonstrate this effect in our samples. Adachi (ref. 19, p.157) had summarized the experimental data for *InGaAsP* lattice matched to *InP* quaternary and made an interpolation of R_{ex} as function of the y composition in the quadratic form:

$$R_{ex}^{3D}(y) = 4.8 - 2.9y + 1.0y^2 \qquad (2.27)$$

The application of eq.2.27 to sample 1; the three-dimensional excitonic Rydberg energy can be calculated and has a value of $R_{exc}^{3D} = 2.7 \div 3.3 meV$ and the corresponding two-dimensional is $R_{ex}^{2D} = 11 \div 13 meV$. Taking into account the dielectric constant of the quaternary $\varepsilon_w(0) = 13.48$ [28] and $\varepsilon_{InP}(0)=12.5$ [19, p.66] , the two-dimensional exciton Rydberg energy is : $R_{ex}^{2D} = 12.8 \div 15.3 meV$, which correspond to a characteristic temperature interval 149-179K ($kT = \varepsilon_{exc}^{2D}$, where k=8.6x10^{-5}eV/K, is the Boltzman constant). These values are close to the maximum of the excitonic signal that we find around 150-180K for the MQWs and 190K for the quaternary epilayer and discuss later in section 4.3.2.

In summary, in the two-dimensional case the exciton ground state energy is up to four times larger than in the three-dimensional one, where the relative separation between the electron and the hole is $a_{o_{ex}}^{2D} = \frac{a_{o_{ex}}}{2}$. This results in a relatively large binding energy and enhanced exciton oscillator strength in quasi-bidimensional heterostructures.

2.3 The photovoltaic effect

The photovoltaic effect (PV) is a general expression indicating the appearance of an external voltage in an illuminated solid(semiconductor). The PV in semiconductors can be associated with the variation of the electronic structure at a *p-n* junction or a metal-semiconductor surface barrier. The photogenerated carriers move in response to local fields establishing a potential difference. We will only consider the internal fields at the

Schottky barrier. The direct contact between metal and semiconductor results in redistribution of charges. This deformation of the band edge at the interface is called "Schottky barrier". To illustrate the barrier, at the metal-semiconductor contact, we take the work functions for the metal and the semiconductor to be Φ_m, and Φ_s, respectively, and consider the case of n-type semiconductor, where $\Phi_m > \Phi_s$ -fig. 2.4a. After contact, the electrons must leave the semiconductor surface in direction to the metal and an equilibrium is established, when the Fermi levels of both sides line up. The potential difference between the two work functions, $qV_D=\Phi_m-\Phi_s$, is called contact potential. The barrier defined by the difference of the metal work function, Φ_m , and the electron affinity, χ , will be:

$$\phi_B = \Phi_m - \chi_s = qV_D + \delta . \tag{2.28}$$

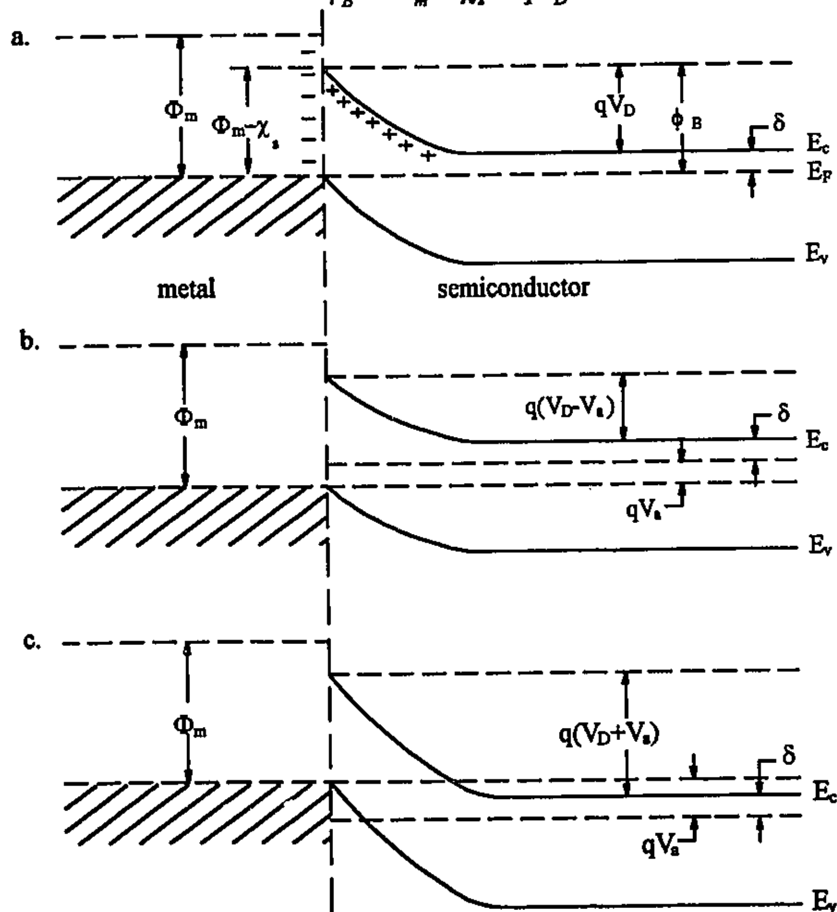

Fig.2.4 Metal/n-type semiconductor energy band diagram: a.-thermal equilibrium; b.-forward bias; c.-reverse bias.

The last equation shows that the barrier height is determined by the potential difference qV_D and the doping step δ of the semiconductor.

To describe the current-transport properties in the metal-semiconductor barrier, different approaches have been used [36-38]. In our study we assume that the carrier flow is caused by thermionic emission only. At zero bias, the electron flux from the semiconductor into the metal is given by the standard thermionic equation [36, p.171]:

$$J_s = qN_D\left(\frac{kT}{2\pi m_s^*}\right)^{\frac{1}{2}} e^{-\left(\frac{qV_D}{kT}\right)}, \qquad (2.29)$$

where m_s^* is the electron effective mass of the semiconductor, N_D is the donor density in the semiconductor, k is the Boltzman constant, and V_D is the built-in potential. From the theory of semiconductors $e^{-\frac{\delta}{kT}} = N_D / 2(2\pi m_s^* kT / \mathrm{h}^2)^{3/2}$. Then eq. (2.29) becomes:

$$J_s = \frac{4\pi}{h^3} q m_s^* k^2 T^2 e^{-\left(\frac{\phi_B}{kT}\right)} = A^* T^2 e^{-\left(\frac{\phi_B}{kT}\right)}, \qquad (2.30)$$

where $A^* = \frac{4\pi}{h^3} q m_s^* k^3$ is the Richardson constant and ϕ_B is the barrier height.

When a forward bias voltage V_a is applied to the junction (fig.2.4b), the effective barrier in the semiconductor becomes $q(V_D-V_a)$ and the electron flow from the semiconductor to the metal is enhanced by a factor of $\{e^{(qVa/kT)}\}$. The current-voltage relation for the junction is, therefore:

$$J = J_s\left[e^{\left(\frac{qV_a}{kT}\right)} - 1\right], \qquad (2.31)$$

where J_s is the diode saturation current, or the reverse bias leakage current.

When a measuring technique with a small resistance R, in series with the semiconductor is used (the measuring circuit is shown in section 3.1), the current-voltage relation is:

$$J = J_s\left[e\frac{q(V_a - JR)}{kT} - 1\right] \qquad (2.31')$$

Equations (2.31) and (2.31') refer to a situation, when the system is in the dark, with no incident radiation. However, under illumination with photon energies $\hbar\omega$, larger than the band gap of the semiconductor E_g, $\hbar\omega > E_g$, photon absorption generated electron-hole pairs in the depletion region lead to a generated current J_L. and the total current of the junction is modified to:

$$J = J_s\left[e\frac{q(V_a - JR)}{kT} - 1\right] - J_L \qquad (2.32)$$

Then, the open circuit photovoltage across the illuminated Schottky barrier is:

$$V_{PV} = \frac{kT}{q}\ln\left(1 + \frac{J_L}{J_s}\right). \qquad (2.33)$$

To derive the spectral responce of the junction, as a function of the wavelength in the region $\hbar\omega > E_g$, we assume the density of the photons in the semiconductor to vary according to the law: $\Phi = \Phi_o\, e^{-\alpha x}$, where α is the absorption coefficient, Φ_o is the total incident photon flux, and x is the distance within the semiconductor. The electron-hole generation rate by the photons has the general form[39,p.421]:

$$G(x) = -\eta d\Phi/dx = \eta\alpha\Phi_o e^{-\alpha x}, \qquad (2.34)$$

where η is the quantum efficiency, equal to the number of excited carrier per photon. Then, the current generated inside the depletion region can be written as[37, p.645]:

$$J_L = -\eta\int_0^W G(x)dx = \eta\Phi_o\left(1 - e^{-\alpha(\lambda)W}\right), \qquad (2.35)$$

where W is the boundary of the depletion region. Applying eq. (2.35) into eq. (2.33) for the photovoltage produced by the photon flux Φ_o, we obtain:

$$V_{PV}=\frac{kT}{q}\ln\left[1+\frac{\eta\Phi_o\left(1-e^{-\alpha(\lambda)W}\right)}{J_s}\right] \quad (2.36)$$

The last relation shows the dependence of the absorption coefficient, $\alpha(\lambda)$, on the photovoltage V_{PV} generated under the illumination of the Schottky junction. The variation of V_{PV} with temperature will depend on the variations of $\alpha(\lambda)$, W, and J_S with temperature. The influence of each of these factors on the photovoltaic spectra will be discussed in the experimental section.

2.4 The effect of an applied electric field on the QW structures

The effects of an applied electric field on the optical properties of quantum wells has been previously considered experimentally[40-45] and theoretically[40,46-48]. In this section we will outline the consequences of the application of an electric field to the MQW structures. We will consider the thickness of the barrier and the height of the potential step large enough, so that the wave functions of the first few levels do not overlap from one well to the other. With these assumptions the properties of the sample are the same, as those of a set of independent quasi-two-dimensional QWs. An applied electric field perpendicular to the QW layers has the following consequences: electrical heating (Ohm's law); widening of the excitonic line; displacement of the optical transitions; ionization of the exciton and selection rules change, followed by the appearance of forbidden transitions. The object of our interest are the last four effects and each of them will be discussed separately.

2.4.1 Displacement of the spectral structures

In QWs , in contrast to bulk materials, the excitons are confined to the direction perpendicular to the layers, which makes the excitonic effects stronger. Large energy shift occurs, due to a major change in the potential of the well -fig. 2.5. The field pushes the electrons and the holes to the opposite walls and modifies the corresponding wave functions. High electric fields can be applied, because the electron and hole wave functions

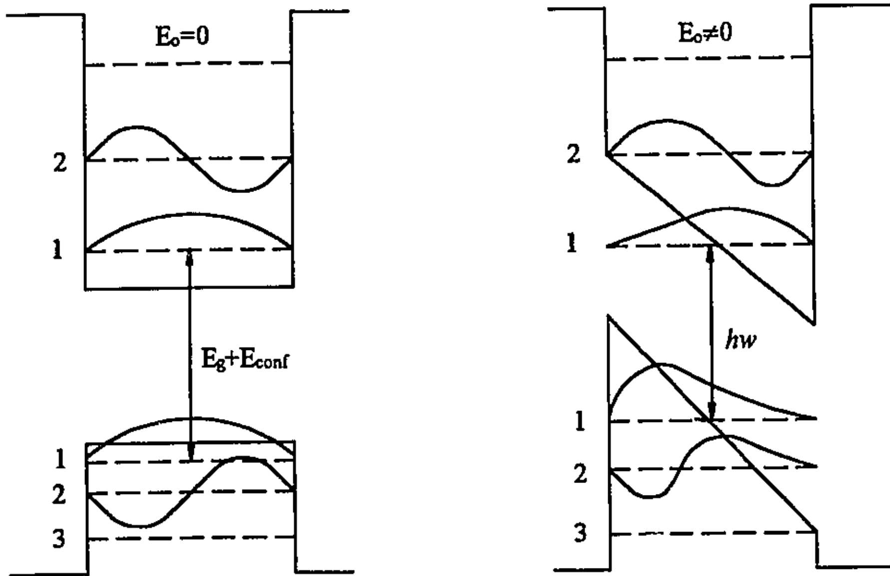

Fig.2.5 The effect of an applied electric field on the QW energy levels and wave functions.

deformation is suppressed by the walls of the QW and also high fields are possible at moderate applied voltages across small width wells. Due to the large exciton binding energy there is enough electron-hole correlation to retain most of the oscillator strengths up to fields of the order of 10^5V/cm.

The effect of an electric field perpendicular to the QWs represents the Quantum Confined Stark Effect (QCSE). To explain the energy shift, we consider the lowest lying heavy (E_1^e-E^{hh}_1) and light (E_1^e-E^{lh}_1) hole excitons, giving the transition position at energy:

$$\hbar w_{hh} = E_g + E_1^e(F) + E_1^{hh}(F) - R_{ex}. \qquad (2.37)$$

Here, $E^e{}_1(F)$ and $E^{hh}{}_1(F)$ are the ground state electron and heavy hole confinement energies under an applied field. The quantity $\hbar w_{hh}$ will be affected by the variations of the subband energies $E^e{}_1(F)$, $E^{hh}{}_1(F)$, and the exciton binding energy R_{ex}. Detailed analysis on the role of R_{ex} in *GaAs/AlGaAs* QWs have been completed by G. Bastard[26, p.315]. The derived dependence of the heavy hole binding energy on the applied electric field for different QW thicknesses, shows that in narrow QWs (quantum well width, L<100Å), the exciton wave function changes very little with the applied field F. The main source for the red shift of the exciton resonance is the dependence of $E^e{}_1(F)+E^{hh}{}_1(F)$ on the field source, whereas R_{ex} contributes little to this shift for narrow *GaAs/AlGaAs* QWs. This follows from experiments showing saturation of R_{ex} at higher fields [40]. So far, there is no experimental evidence for the contribution of R_{ex} in *InGaAsP/InP* MQWs. In general, we can say that the spectral shift of the ground state exciton is a super-position of $E^e{}_1(F)$, $E^{hh}{}_1(F)$, and R_{ex}. Therefore, the energy shift direction will depend on how each of this factors is affected by an applied electric field.

2.4.2 Selection rules change and appearance of forbidden transitions

When an electric field is applied to a quantum well, there is a secondary consequence related to the lowering of the symmetry, and thus the strict transition selection rules change. In addition to Stark shifting, the electric field may also result in Stark splitting of the degenerate exciton levels. Depending on the transition selection rules for p and s excitons under an applied electric field, the appearance of forbidden transitions may occur. In two-dimensional systems the selection rules state, that optical transitions occur between quantized electron and hole states in the valence and conduction bands of the same quantum number. Thus allowed transitions are those, which occur between quantized electron and hole with the same quantum number j, i.e. Δj=0 (fig.2.3). In the absence of an electric field, transitions with $\Delta j \neq 0$ are forbidden, however when an electric

field is applied, the wave functions of the electron and the hole change, their overlap is not exactly orthogonal and transitions with $\Delta j \neq 0$ become allowed. Their appearance can be derived from the selection rules for the interband transitions, which we will not discuss here.

2.4.3 Broadening of the excitonic peaks

Another consequence of an applied electric field to QWs is the broadening of the excitonic peaks. The field pushes the electron towards one and the hole towards the opposite wall of the well, which results in reduction of the Coulomb energy. However, when the thickness of the well is less than the three-dimensional exciton radius, the exciton is still bound up to high fields- 10^5V/cm. The walls of the well inhibit field ionization, and electrons and holes do not tunnel rapidly through the heterostructure barriers. The single-particle tunneling rate can be estimated from the widths of the tunneling resonances; if the resonance has half-width at half maximum of the energy response ΔE, then the life time of a particle in the state is $\propto \frac{\hbar}{\Delta E}$. The broadening can be observed experimentally in the QW spectra with different detecting techniques. In the present work we use the field dependent PV effect to study the broadening of the *11H* exciton.

2.4.4 Ionization of the exciton

To ionize an exciton into an unbound electron-hole pair, the electric field has to be of magnitude high enough to provide energy that is at least equal to the binding energy of the exciton across the Bohr radius, and the ionization field can be written as:

$$F_c \geq \frac{R_{ex}}{q a_{o_{ex}}}, \tag{2.38}$$

where R_{ex} given by eq. (2.16) is the excitonic energy, and $a_{0_{ex}}$ given by eq. (2.17) is the exciton Bohr radius. In two dimensions for n=1, the ionization field will be:

$$F_c \geq \frac{4R_{exc}}{q\left(\frac{a_{0_{exc}}}{2}\right)} = \frac{8R_{exc}}{qa_{0_{exc}}} \tag{2.39}$$

The last relation shows that in quasi-two dimensional structures the energy required to field-ionize the bound electron-hole pair is up to eight times higher than in three dimensional semiconductor. It also explains why strong excitonic features are present up to high electric fields in quantum wells. In our study the electric field required for the ionization of the exciton in *InGaAsP* at 212K was found to be of the order of $F_c \geq (1.02 \div 1.22) \times 10^4 V/cm$, where a_{0exc}=250Å (ref.17).

In summary, the electric field-induced changes on the ground state exciton lead to a variety of effects, including Stark shifting, Stark splitting, broadening of the excitonic peaks, and ionization of the excitons. All these effects are very important in understanding the optical properties of QW structures and their application in opto-electrical devices.

2.5 The effect of temperature on the optical transitions

The variation of the energy gap with temperature is believed to result from two mechanisms. First, there is a shift in the relative position of the conduction and valence bands of the crystal, as a result of a change in the interatomic distances, and second, there is a shift in the relative position of the conduction and valence bands, as a result of the temperature dependent electron(hole) - lattice interaction.

2.5.1 Temperature dependence of the optical transitions

First, we will consider the deviation of the lattice constant, which directly changes the energy level and the band gap energy position. For most semiconductors, at first approximation this effect is linear at high temperatures. For III-V semiconductors the dependence is non-linear at low temperatures and the temperature induced change in the band gap energy $E(T)$, can be expressed with the following empirical relation[49]:

$$E_g(T) = E_g(0) - \frac{\alpha T^2}{T+\beta}, \qquad (2.40)$$

where $E_g(0)$ is the value of the energy gap at 0K, and α and β are constants depending on the material. Experimentally, the temperature dependence of the energy gap for III-V compounds can be fitted well to Varshni's relation (eq.2.40), and for our MQW system (y=0.68) will have the form:

$$E_g(T) = 0.989 - \frac{4.4 \times 10^{-4} T^2}{T+270}, \qquad (2.41)$$

where α=4.4x10^{-4}eV/K and β=270K are Varshni's coefficients deduced in section 4.2. The last equation shows that with the increase in the temperature, the band gap shifts to lower energies.

2.5.2 The effect of electron-phonon interactions

The temperature dependence of the broadening function $\Gamma(T)$, which describes the influence of the electron-phonon interactions on the excitonic peak width, can be expressed as a sum of two components [50]:

$$\Gamma(T) = \Gamma_o + \frac{\Gamma_1}{e^{\frac{\hbar\omega_{Lo}}{kT}} - 1} \qquad (2.42)$$

where Γ_o is temperature independent and is affected by the fluctuations in the layer thickness, Γ_1 is a measure of the phonon broadening, and ω_{Lo} is the phonon frequency.

The excitonic linewidth increases as a function of temperature, but above ~150K the rate of increase is greater due to increase of the thermal population of phonons. Therefore, the temperature dependence of the excitonic linewidth is the sum of Γ_o and the temperature dependent term, proportional to the density of the thermally activated optical phonons. The broadening parameter for the MQWs is found less than the one for GaAs. For instance for *GaAs/AlGaAs* MQW, Γ_o is found to be of the order of 2meV and Γ_1=5.5meV[50].

At high temperatures, excitons are unstable against collisions with thermal phonons. The phonon energy can be much higher than the exciton binding energy. Thus a single exciton-phonon collision can ionize the exciton and release a free *e-h* pair. If the temperature broadening of the excitonic resonances is interpreted as a life time reduction, due to the thermal phonons scattering, the excitons lifetime may be as short as 0.4ps in *GaAs* at room temperature[50]. Due to the enhancement of the exciton binding energy in quasi-bidimensional systems, excitonic structures are still pronounced even at room temperature. The photovoltaic spectra of *InGaAsP* MQW materials show strong excitonic features at room temperature, (discussed in chapter four).

2.5.3. Excitonic effects: temperature dependence

The excitonic effects have strong temperature dependence, because the exciton line follows the band edge shifts. With the temperature increase the excitonic peak shifts to lower energies together with broadening of the half-width at half-maximum due to the increased role of the phonons. The excitons are thermally dissociated, when the thermal energy exceeds the exciton binding energy R_{ex}, or:

$$kT_{ion} \cong R_{ex} \qquad (2.43)$$

Therefore excitons are stable at temperatures T lower than the thermal ionization temperature T_{ion} or: $T < T_{ion}$. For the lattice matched *InGaAsP/InP* MQW samples our experimental value of the ionization temperature was found to be $T \approx 150-180K$.

This chapter describes the theory applied to the basic properties of quantum wells and their application to *InGaAsP/InP* MQWs and *InGaAsP* epilayers lattice matched to *InP*. The next chapter will deal with the description of the samples and the experimental techniques used in conducting the various experiments.

III. Experimental techniques

3.1 Sample preparation

This study is based on the experimental research of the *InP* substrate, the *InGaAsP* epilayer lattice matched to *InP*, and complete *InGaAsP/InP* MQWs grown by Chemical Beam Epitaxy (CBE). The deposition was completed by Dr. A. P. Roth at the Institute for Microstructural Sciences of the National Research Council of Canada (NRCC). The growth technique is described in detail in ref.20, pp.87-106 and will not be discussed in this chapter. The parameters of the epitaxial growth process are connected with the optical and structural properties of the QW heterostructures and their performance in device application[51]. The lattice matching between *InGaAsP* and InP is critical and defines the choice of x and y concentrations within the limits of $0 \leq x \leq 0.47$ and $0 \leq y \leq 1$. The samples that we have studied are mostly lattice matched, although when multiple quantum wells are grown it is very difficult to control exactly the same thickness of the layers, especially for ultrathin heterostructures. The quaternary epilayer and the MQWs were grown on the (100) side of *InP* substrates (*S*-doped) with good conductivity characteristics. The epilayer structure (sample 4) consists of 3000Å buffer layer of *InP* and 1500Å thick *InGaAsP* epilayer followed by 300Å thick *InP* cap layer. Figure 3.1a. shows the stacking of the layers. The complete MQW structure consists of a 3000Å buffer layer of *InP*, ten periods of 80Å thick *InGaAsP* wells separated by nine periods of 320Å thick *InP* barriers, and a cap layer of undoped *InP* with thickness of 320Å. Figure 3.1b shows the typical configuration of the MQW with x=0.28 and y=0.68 (sample 1 and sample 2). The strained sample (sample 3) with x=0.32 and y=0.56 has the same configuration as samples 1 and 2 except that the thickness of the *InGaAsP* wells are 82Å and the *InP* barriers are 330Å-fig.3.2.

To confirm the desired quantum well and epilayer thicknesses and the lattice matching of *InGaAsP* to *InP*, the grown samples were examined by Dr. A. Roth at NRCC

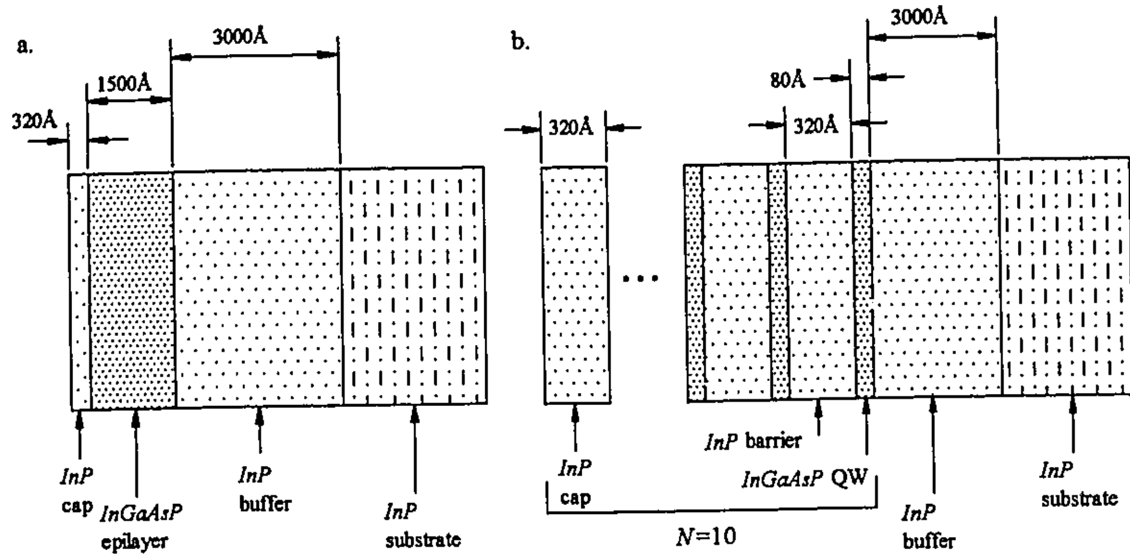

Fig. 3.1 Schematic views of: a.- the *InGaAsP* quaternary epilayer, sample 4 and b.-*InGaAsP/InP* MQWs, samples 1 and 2.

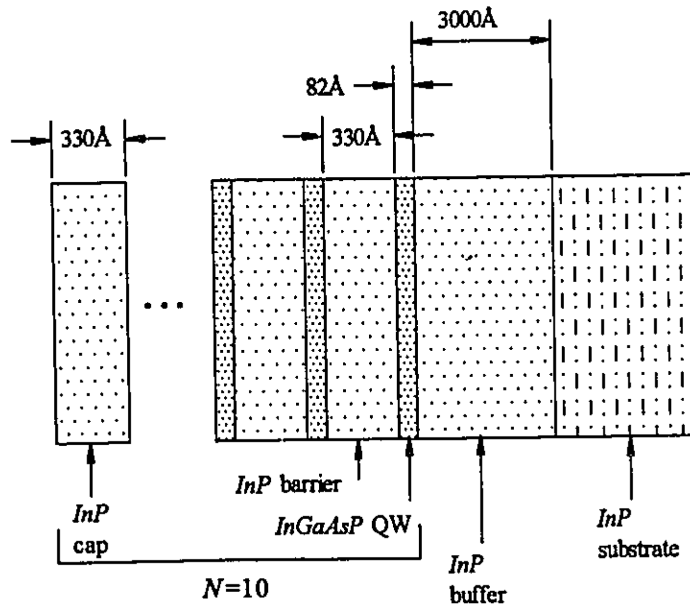

Fig. 3.2 Schematic view of sample 3.

using low temperature (4K) photoluminescence. Lattice mismatches of 0.1% at 4K (for sample 1 and 2) and 0.02% (for sample 4) were found, which can be considered close to perfect. The analysis of sample 3 gives 0.43% lattice mismatch between *InP* and the wells, which shows that they are strained. Later in the characterization of the energy transitions

the PV spectrum shows that the lower energy state of this sample is a transition from the first electron state E^e_1 to the first light hole level E^{lh}_1. X- ray double diffraction measurements were also conducted and a deviation of ±10Å from the intended thicknesses of the samples was found.

For all photo-electric experiments, electrical contacts are needed. The Schottky barrier contacts were made by evaporating gold (*Au*) droplets creating a semi-transparent 70Å film on the front surface of the sample. In order to protect the MQW sample from the diffusion of the electrically conducting silver (*Ag*) epoxy (used to fix the wires to the sample) and short circuit it, a thicker layer of *Au* (300Å) was deposited on the semi-transparent film, over an area approximately the size of the contact. The back contact was made by fixing *Au* wire with *Ag* epoxy to the back surface covered with thick indium (*In*) layer previously deposited during the growth of the sample. Fig.3.3 shows the

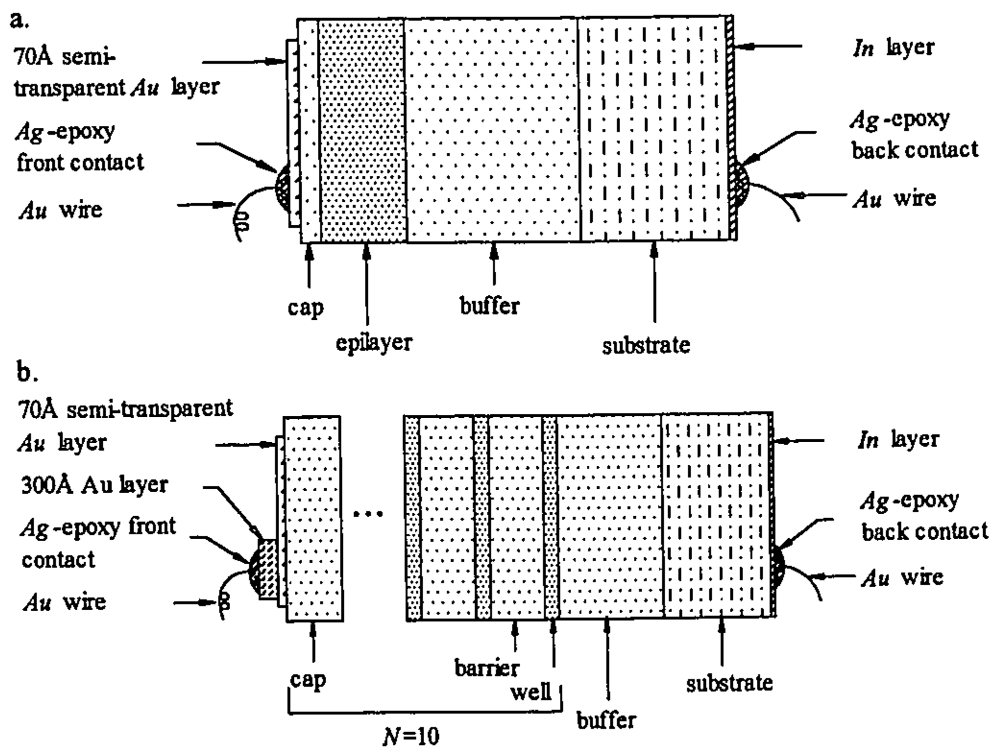

Fig. 3.3 Electrical contacts for: a.- the epilayer and b.-a typical MQW.

configuration of the contacts for the epilayer and for a typical MQW. Sample 2, with an additional insulating layer, was made in the same way, only before evaporating the semi-transparent *Au* electrode, a 50Å MgF_2 film was deposited to the approximate contact area. Such an interfacial film would increase the effective barrier heights. The room temperature I-V characteristics for the second type Schottky diodes indicate a built-in potential of 0.3V, compared to 0.1V for the first one. The characteristics of the samples are summarized in table 3.1.

Table 3.1 Sample characteristics

parameter	sample 1		sample 2		sample 3		sample 4	
	InGaAsP/InP MQW		*InGaAsP/InP* MQW		*InGaAsP/InP* MQW		*InGaAsP* epilayer	
	expected	real	expected	real	expected	real	expected	real
buffer, Å		3000	3000	3000	3000	3000	3000	3000
well, Å	80±10	80	80±10	80	72±10	82		
epilayer, Å							1500	1500
barrier, Å	320±10	320	320±10	320	340±10	340		
cap, Å	320±10	320	320±10	320	340±10	340	300±10	300
As, %	70±2	68	70±2	68	56±1	56	64±2	64
Ga, %	28±2	28	28±2	28	32±1	32	30±2	32
1. *Au* layer, Å	70	70	70	70	70	70	70	70
2. *Au* layer, Å	300	300	300	300	300	300		
M_gF_2 layer, Å			50	50				
lattice mismatch, %		0.24		0.24	0.43-0.45	0.43		0.03

3.2 The Photovoltaic experiment

In this work the photovoltaic technique is used to measure the energy levels of *InGaAsP*. The diode structure allows for high sensitivity photovoltaic measurements with A.C. modulation and at the same time with D.C. bias applied to observe the transition energy changes (electric field effects). Because the photovoltage is directly related to the absorption coefficient giving rise to the spectral features, excitation with photon energies $\hbar w$ below the band gap of *InP* E_g(InP) would lead to transitions between the quantum well conduction and valence band states. These effects will be observed as sharp peaks in the photovoltage spectrum. However, with light reaching the cap and the buffer layers the absorption will increase and may become dominating factor in the photogenerated signal. The photovoltaic measuring technique will also be used to study various transitions influenced by an applied electric field with direction perpendicular to the layers of growth. The applied field will produce changes in the absorption coefficient, due to perturbation in the bands of the heterostructure, effect that will be seen as spectral shifting of the various transitions.

The experimental set-up for the PV measurements is shown in fig.3.4. The light source is a 30W quartz iodine lamp with tungsten filament, focused with a mirror to the entrance slit of a 3/4 meter spectrometer. To eliminate the second order effects, the white light first passes through a red Hoya filter(starting to transmit at 800nm). The second element that the light beam passes through, is mechanical chopper with adjustable frequency, used as reference signal for the lock-in amplifier. The working frequencies are set between 17Hz and 470Hz, depending on the ratio: noise figure/sample resistance. The spectrometer accuracy is limited by the grating constant, stepper motor and the exit slit. In our case, the monochromatic beam that exits the spectrometer has resolution of 5Å at 1mm slit. With a second concave mirror the light is focused onto the sample, mounted in an optical cryostat and oriented in such a way, that the front electrode faces directly the

incoming beam. The photogenerated signal is detected by a standard lock-in amplifier and the data analyzed by computer.

For the realization of the experiment with external perturbation applied to the sample in the form of an electric field, the same experimental set-up is used as in fig.3.4, except that a bias unit is added to the experimental elements diagram (shown in dashed line in fig.3.4). A detailed view of this unit is shown in fig.3.5, where R_S is the sample and r is a small variable resistance, $r \ll R_S$, across which the potential drop is measured. Generally r is taken as 1% of the sample resistance. The bias voltage applied to the sample

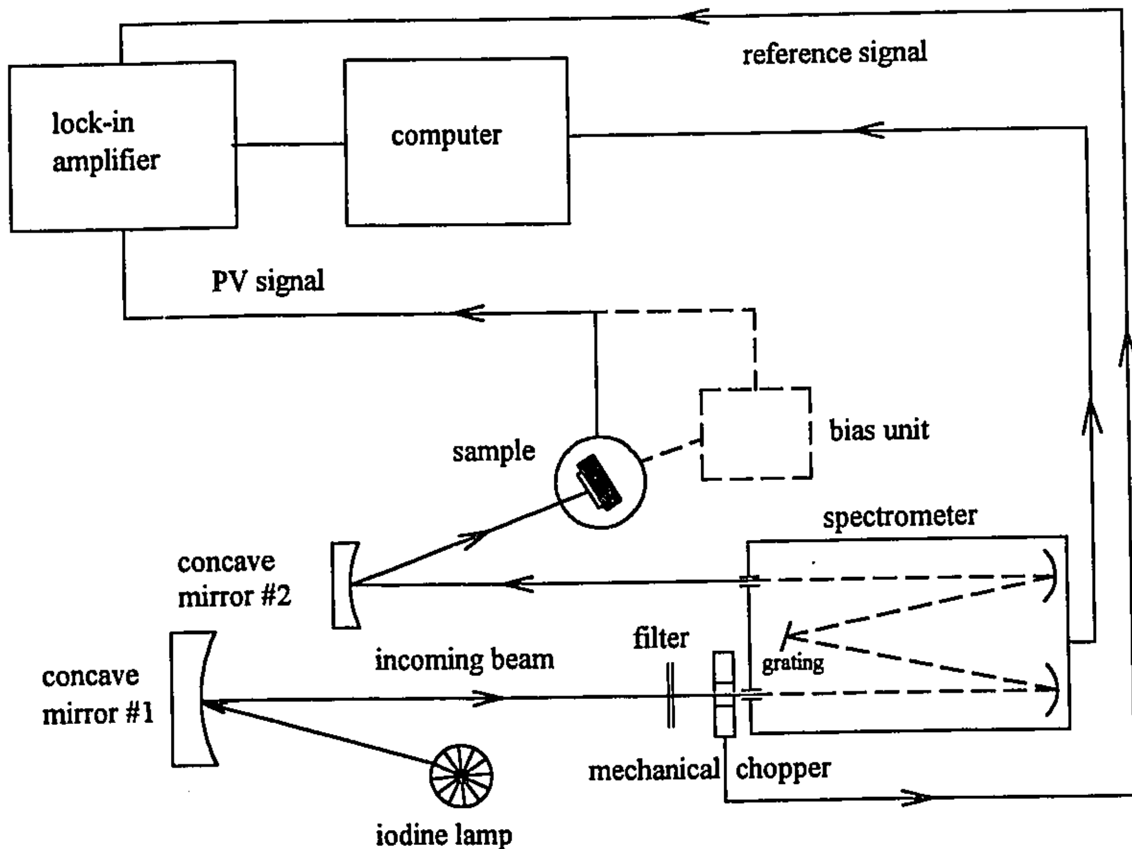

Fig. 3.4 Set-up diagram for the PV experiment.

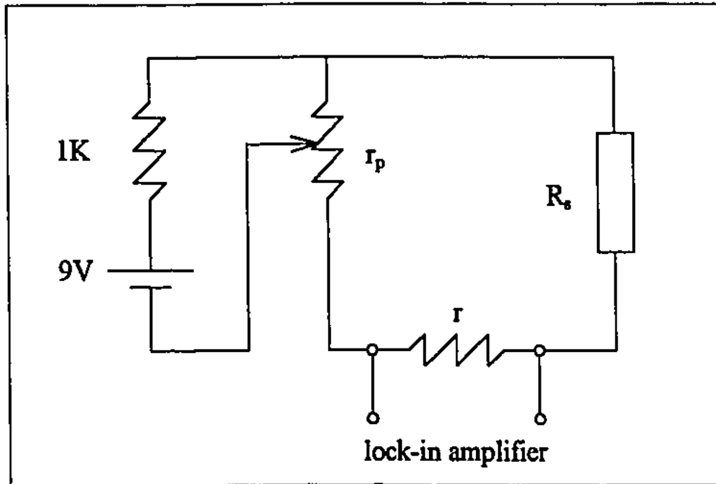

Fig. 3.5 Schematic view of the bias unit.

is varied from -1V to 0.2V (1.4×10^4V/cm to 2.9×10^3V/cm) by a potentiometer-r_p. A resistance of 1K in series with the battery provides current limiting protection.

For the I-V measurements needed for the determination of the barrier heights of sample 1 and sample 2, we use the set-up shown in fig.3.6. The sample is placed in the dark, allowing the I-V curve to pass through the origin at zero applied voltage. A Kythley155 microvoltmeter is used to measure the voltage drop across a standard 1K resistance. A DC power supply (Hewlett Packard-E3610A) is used to vary the voltage by steps of 0.05V.

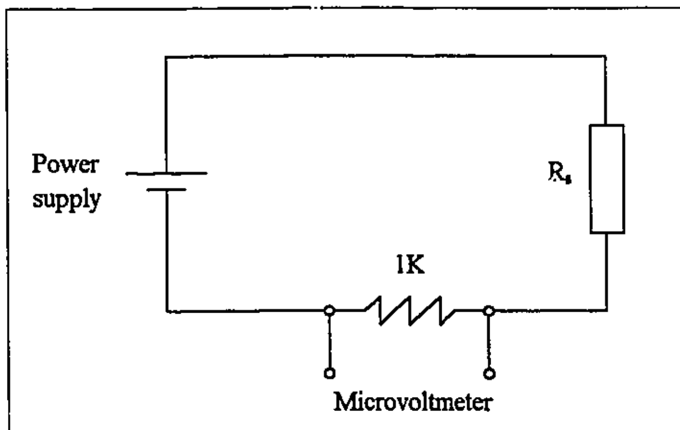

Fig.3.6 Schematic view of the set-up for I-V measurements.

3.3 The double beam experiment

In a typical nonlinear optical experiment the sample is excited by an intense laser beam, called pump beam. The secondary probe beam has very low intensity (I_p=1.5x10^{-5}W/cm^2), which does not introduce any nonlinearities and is used to measure the changes in the optical properties of the sample in nonlinear aspect, caused by the first beam. The photovoltaic signal generated in the presence of probe and pump beams is recorded and the spectrum compared to the photovoltaic spectrum of the probe beam only. In our experiment, a 10mW(I=1.3W/cm^2) *He-Ne* laser (λ=632.8nm) is used as pump beam and the standard photovoltaic detecting technique (shown in fig.3.4) to generate the probe beam. The intensity of the first beam is varied by neutral density filters. The positions of the beams falling onto the sample are shown in fig. 3.7. The photogenerated signal is characterized by an absorption coefficient α_o. When the pump beam is introduced, it changes the internal field of the sample and thus affects also the current transport and the related absorption coefficient. The photovoltaic spectrum is very sensitive to these changes and is used to monitor and analyze the pump beam influence on the optical properties of the sample.

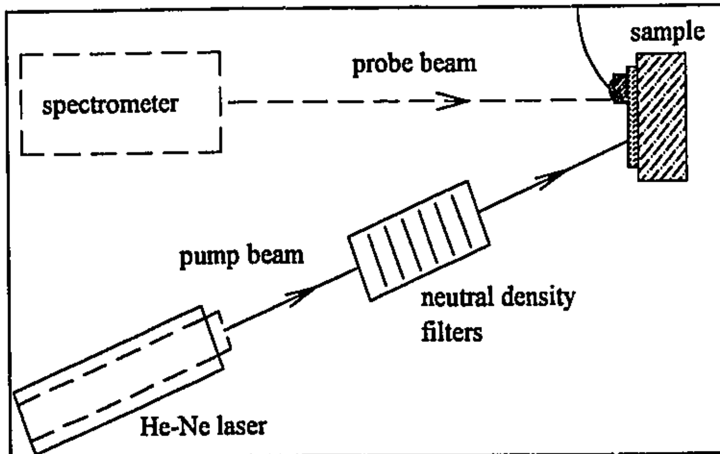

Fig.3.7 Set-up diagram for the double beam experiment.

3.4 Temperature control of the sample

For all experiments conducted in this study a range of temperatures is required and various techniques are used to obtain them. In order to study the optical transitions in the temperature interval 6-300K, the sample is mounted in a Janis Instruments optical cryostat. The temperature control is realized by a feed back and a current flow heating system, connected to two temperature sensors, placed close to the sample. Detected in such a way, the sample temperature was within 2% of the sensors readings. A simpler, cold finger type cryostat was used to study the excitonic signal at temperatures between 77-300K. To cool down the sample and control the temperature over a long period of time (required for some of the experiments), the liquid nitrogen (normally used) was replaced with a dry ice/acetone mixture. The freezing point of acetone is below that of the dry ice and thus ensures good thermal contact between the dry ice and the cold finger of the cryostat. A temperature of ≈210K was reached in this set-up and was kept stable for a few hours.

The next chapter will deal with the experimental results and discussions.

IV. Experimental results and discussion

The experimental results are presented in this chapter. The results obtained for the *InP* substrate, *InGaAsP* epilayer and *InGaAsP* MQWs will be compared, when the same experiments have been performed. The suitability of the material properties for device applications will be discussed. The chapter is divided in four main divisions. Section 4.1 describes the results obtained in a study which involves the photovoltaic effect to determine the quality of the barrier heights of *Au/InP* and *Au/InGaAsP* for the epilayer and the I-V characteristics for the barrier heights of *Au/InGaAsP* for the MQWs. Section 4.2 presents the PV signal as a function of the temperature of the substrate, the epilayer, and the MQWs. Section 4.3 deals with the results obtained for the MQW samples in an applied external electric field at different temperatures and also gives a comparison of the experimental and the calculated values for the thermal ionization energy. The last section gives experimental evidence for the photomodulation nonlinearities in *InGaAsP/InP* MQWs.

4.1 Measuring the Schottky-barrier heights

The existence of good Schottky barrier appears to be a very important factor for the generated PV signal. The barrier height determines the sample's built-in electric field. The application of an external bias voltage in addition to the internal field has influence in the quantum well features behavior. The barrier height of *Au/InGaAsP* epilayer lattice matched to *InP* was experimentally measured by the Photovoltaic technique at 96K and 160K. A different technique was applied in determining the barrier height of *Au/InGaAsP/InP* MQW samples. Current-voltage characteristics were scanned in the -1.5V to 1.5V interval of an applied biased voltage, and the dark leakage current was measured. Applying the findings for the leakage current to eq.2.31, the barrier heights can

be obtained. The enhancement of the barrier height of *Au/InGaAsP/InP* MQW sample with an interfacial film of 50Å M_gF_2 in addition to the formation of the standard Schottky contact (see section 3.3 for detailed description of the sample and contacts) will be analyzed as an important factor in the fabrication of opto-electronic devices (for example high frequency MESFETs).

4.1.1 The Schottky-barrier heights of the $Au/In_{0.7}Ga_{0.3}As_{0.64}P_{0.36}$ epilayer

In order to determine the barrier heights of the *Au/InGaAsP* epilayer the PV signal is collected at three different temperatures, 96K, 160K, and 300K. Figure 4.1 shows the spectra (corrected to flat detector) in the quaternary band gap region. The actual intensity of the PV signal at the different temperatures is presented in the figure. Relatively large signals were observed in the band gap region of the quaternary due to the photoexcitation

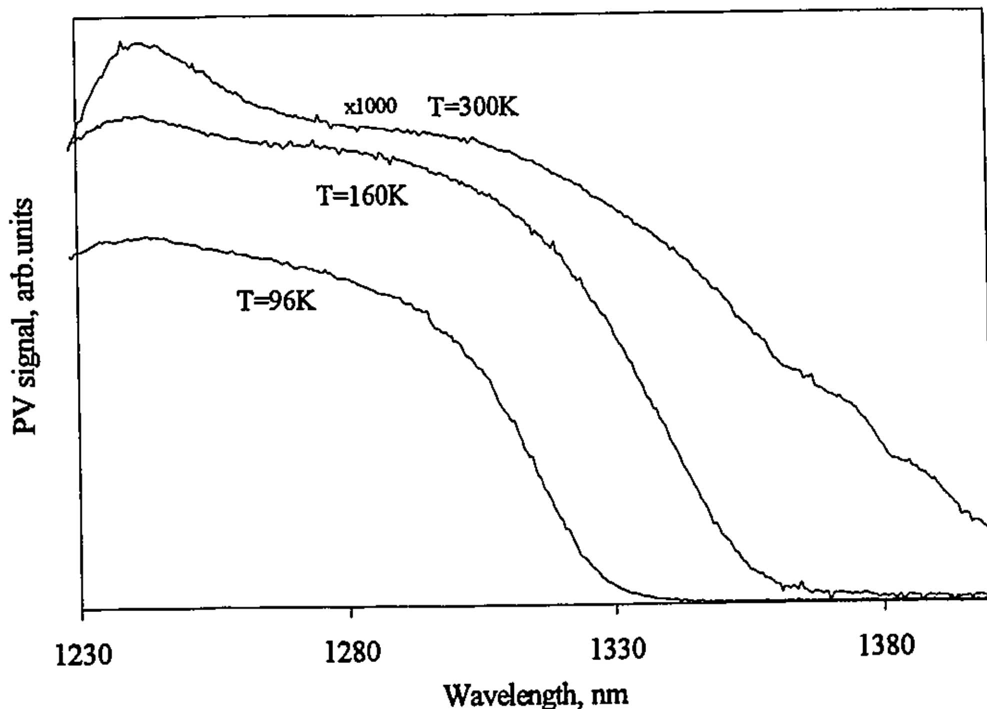

Fig.4.1 PV spectra for the epilayer in the band gap region.

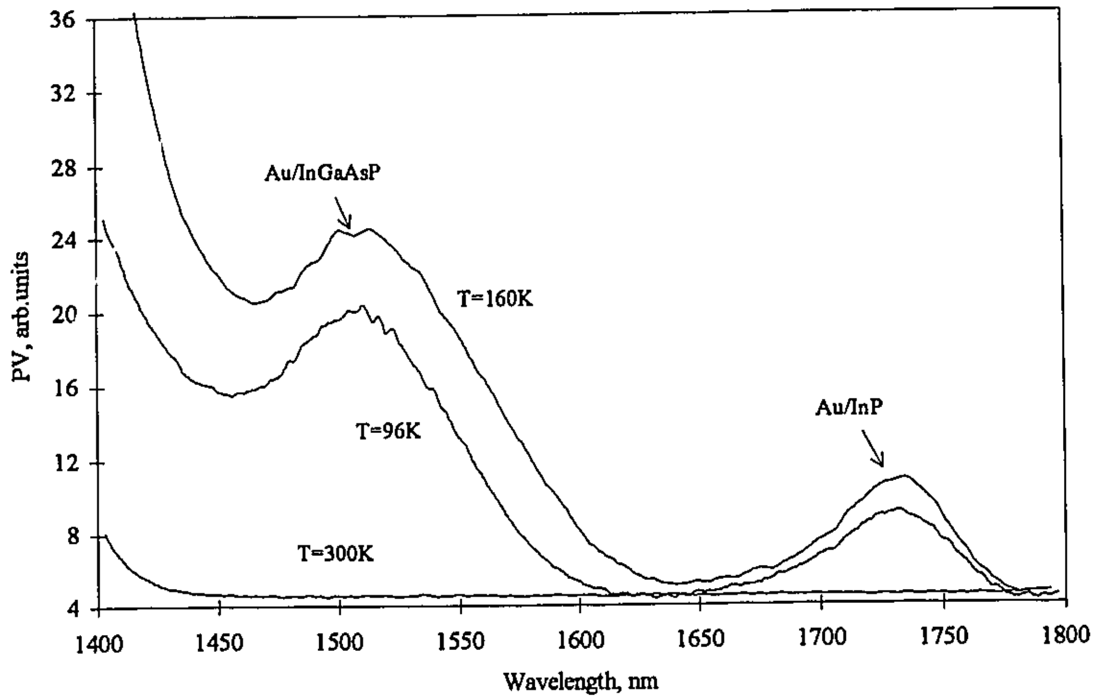

Fig. 4.2 PV spectra for the epilayer in the region of the barrier heights.

of the electrons from the valence to the conduction bands. For photon energies less than the band gap of *InGaAsP*, a signal about 100 times smaller was measured.

Upon careful examination of the PV signal in the spectral interval 1400-1800nm (0.88eV-0.69eV) two well resolved features are noticed- fig4.2. The two peaks observed at temperatures below 200K, correspond to the photoexcitated carrier overrunning the two barriers created by the *Au/InGaAsP* and *Au/InP* Schottky junctions. At temperatures T>200K the intensity of the photogenerated signal is very small and it is not possible to distinguish the barriers. The spectral position of the peaks does not change with temperature, indicating that the observed features can not be interpreted as impurity peaks. The barrier heights are directly derived from the PV spectra at 96K and 160K by a linear fit to the experimental data points in the peak regions. The square root of the spectral response, extrapolated to zero PV signal gives the value of the barrier height[52]. The observed barrier heights obtained in this way are ϕ_B=0.66±0.02eV for

$Au/In_{0.7}Ga_{0.3}As_{0.64}P_{0.36}$ and ϕ_B=0.74±0.02eV for *Au/InP* at 96K, and ϕ_B=0.68±0.02eV and ϕ_B=0.75±0.02eV for $Au/In_{0.7}Ga_{0.3}As_{0.64}P_{0.36}$ and *Au/InP*, respectively at 160K. The two temperature results are practically the same within an experimental error of 0.02eV.

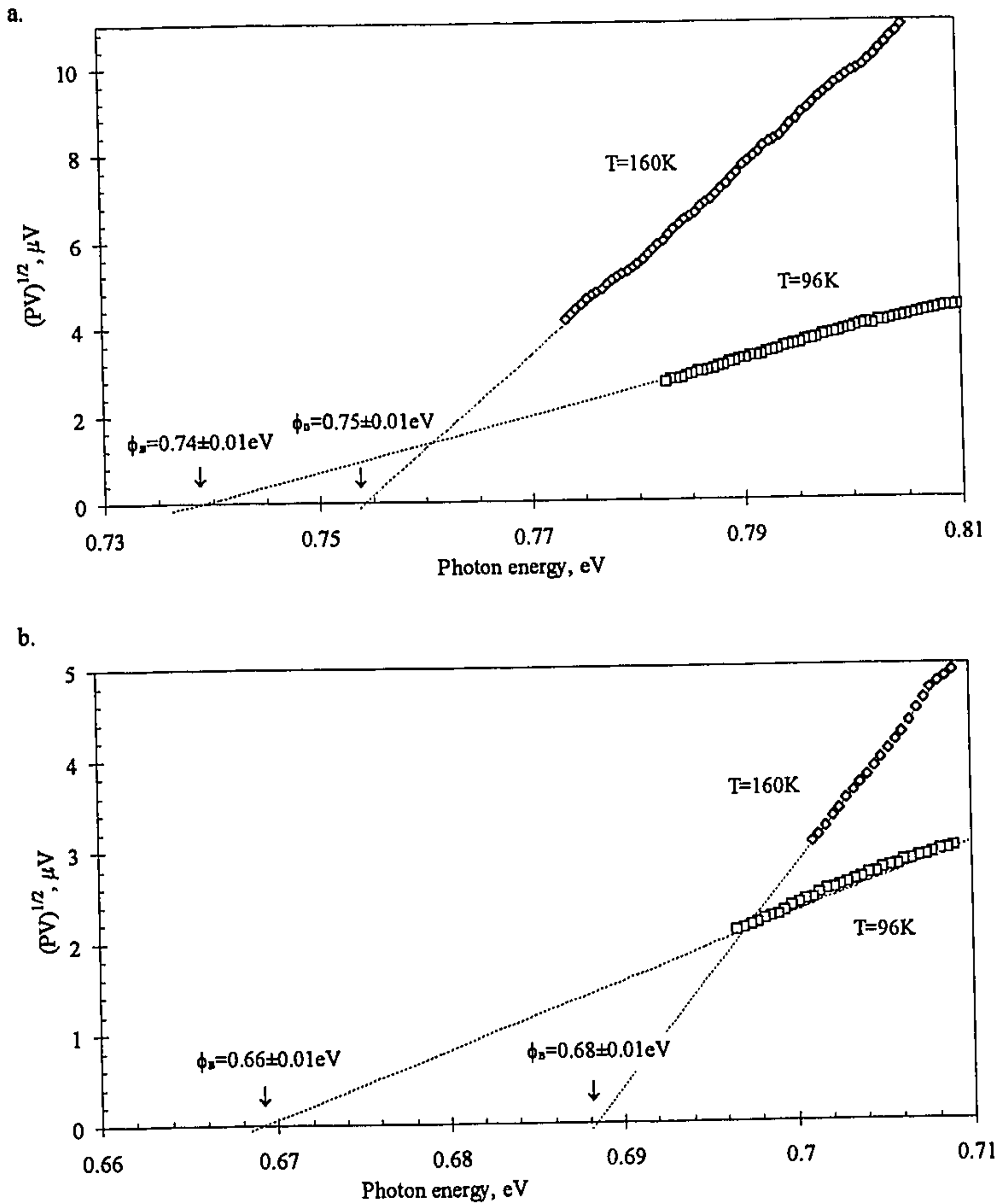

Fig. 4.3 Barrier heights of: a.- *Au/InP* and b.- *Au/InGaAsP* at 96K and 160K.

The results for the barrier heights correlate well with other published data, which summarize the barrier heights for different x and y compositions of *InGaAsP* quaternary system[52]. For *Au/InP* the value of 0.77+0.02eV at room temperature[52] is the same within the experimental error, as the one found in our study. From the composition dependence derived in ref.52 for $In_{0.7}Ga_{0.3}As_{0.64}P_{0.36}$, ϕ_B is deduced as ϕ_B=0.58±0.02eV. Our experimentally observed ϕ_B is slightly higher than this value, which could be an indication of the excellent surface of our sample, as our measuring technique is very sensitive to different surface effects.

4.1.2 The Schottky-barrier heights of the $Au/In_{0.72}Ga_{0.28}As_{0.68}P_{0.32}/InP$ MQWs

The second measuring technique for the determination of ϕ_B is applied to the MQW samples, because in the spectral region 1400nm-1800nm where the barrier heights are expected to appear the junction is not very active, making it impossible to determine ϕ_B directly. In order to obtain the barrier heights, the I-V curves for two *Au/InGaAsP/InP* MQW samples under different conditions of Schottky junction formation are measured at 212K and 300K. The voltage drop across the load resistor (see section 3.2 for the measuring circuit) caused by the change in the sample impedance is measured at different applied bias voltages.

Figure 4.4a shows the I-V curves for sample 1 at 212K and 300K, which has a diode like current-voltage characteristic. The data points are scanned in the dark and the curves go through the origin at zero applied voltage. The graphs define two regions, where at low applied voltages (between ≅ 0.4V- -0.8V) the current-voltage dependence is linear (Ohm's law) and for high applied voltages becomes exponential. For accurate determination of the leakage current, needed to calculate the barrier height, the linear region of the I-V characteristic was expanded and is shown in fig.4.4b. From there, we

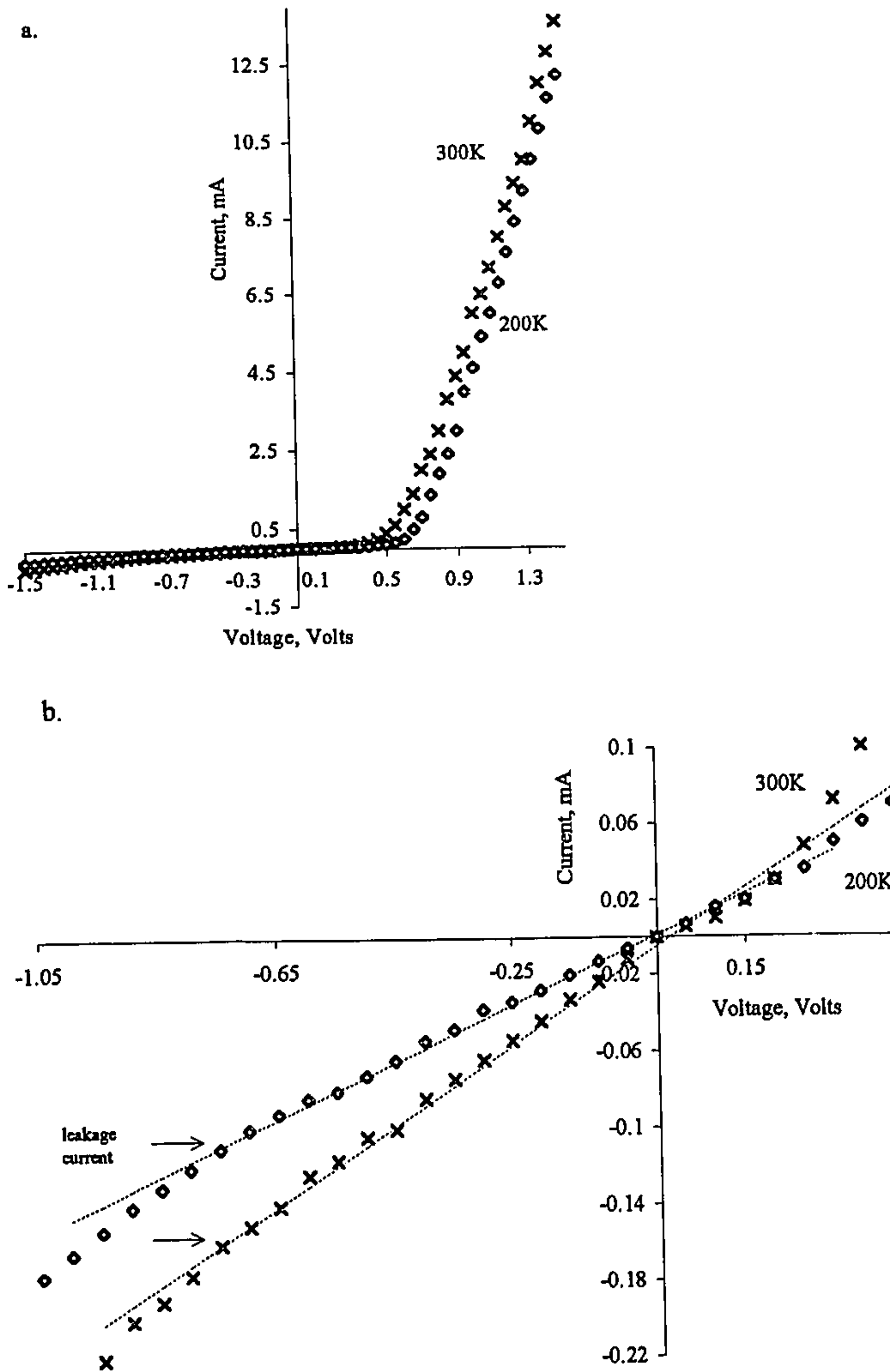

Fig.4.4 Current-voltage characteristics of *Au* Schottky diodes made on sample 1 at: a.- 300K and 212K, b.-expanded linear region, sample 1 at 212K and 300K.

measure reverse leakage currents of I_S=160μA at 300K and I_S=100μA at 212K. To determine ϕ_B for sample 1 the results for I_s are applied to equation 2.30, transformed in the form:

$$\phi_B = \frac{kT}{q}\ln\left(\frac{A^*T^2}{J_s}\right) \qquad (4.1)$$

where $J_S=I_S/A$, A is the area of the Schottky contact, A=0.2cm^2 for sample 1; I_s is the reverse leakage current determined above; A^* is the effective Richardson constant, $A^*=(4\pi m^* q k^2)/h^3$, m* is the effective mass of the $In_{0.72}Ga_{0.28}As_{0.68}P_{0.32}$ quaternary, m*=.052[28]; k is the Boltzman constant, therefore A*=6.23A.K^{-2}cm^{-2}. Applying these values in eq.(4.1), we obtain a barrier height of ϕ_B=0.53±0.02eV at 300K and a value of ϕ_B=0.37±0.02eV at 212K. The ϕ_B found here is similar to ϕ_B=0.4eV measured in ref.53 at 78K for a x and y composition yielding a band gap energy of 0.9eV, which is close to our x and y dependence for this sample.

The second sample has an additional 50Å M_gF_2 interfacial film, directly deposited on the surface of the QW before the formation of the Schottky junction. The current-voltage characteristics for this sample at 212K and 300K are shown in fig.4.5. The I-V curve at 300K shows softer reverse break down possibly due to the insulating layer influence, enhancing the electric field at the periphery of the diode[54].For an accurate determination of the reversed leakage current, the curves in the linear region are again expanded -fig.4.6. From a linear fit to the experimental points for sample 2 we obtain values of I_S=10μA at 300K and I_S=0.1μA at 212K. The existence of an insulating layer between the metal and the semiconductor in this case will change the Schottky barrier by a tunneling factor Dd,[54] where d is the thickness of the interfacial layer and D is a constant at constant temperature. The second sample has the same contact area as the first one, i.e. A=0.2cm^2. In a similar way, analyzing these values, taking into account the M_gF_2 interfacial layer, eq.2.31 can be written as:

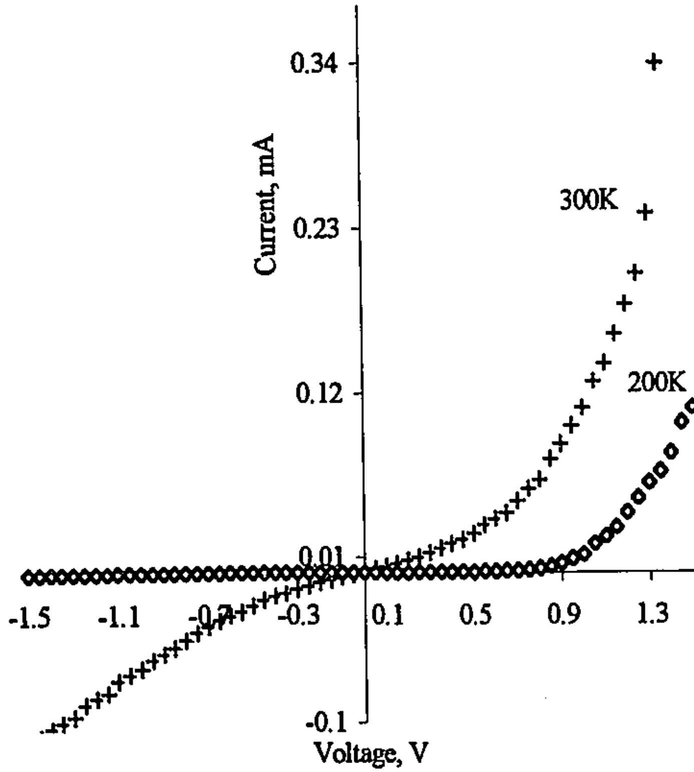

Fig 4.5 Current-voltage characteristics for sample 2 at 212K and 300K.

$$\phi'_B = \phi_B + Dd\frac{kT}{q} = \frac{kT}{q}\ln\left(\frac{A^*T^2}{J'_s}\right), \tag{4.2}$$

where $J'_S = I'_S/A$. Therefore, we obtain values of ϕ'_B=0.6±0.02eV at 300K and ϕ'_B=0.49±0.02eV at 212K for the barrier heights for sample 2. If we take the value of ϕ_B previously found for sample 1, where no interfacial film exists, the tunneling factor *Dd* can be evaluated. From equation 4.2 we obtain *Dd*=2.7, or *D*=5x10^{6}V/cm, which is of the same order as the value of *D*=1.3x10^{6}V/cm found in ref.54. It should be noted that the barrier height ϕ'_B , measured by the current-voltage technique includes the potential drop in the interfacial film. The value of the parameter *D* depends on the density of the surface-state in the insulating layer[55].

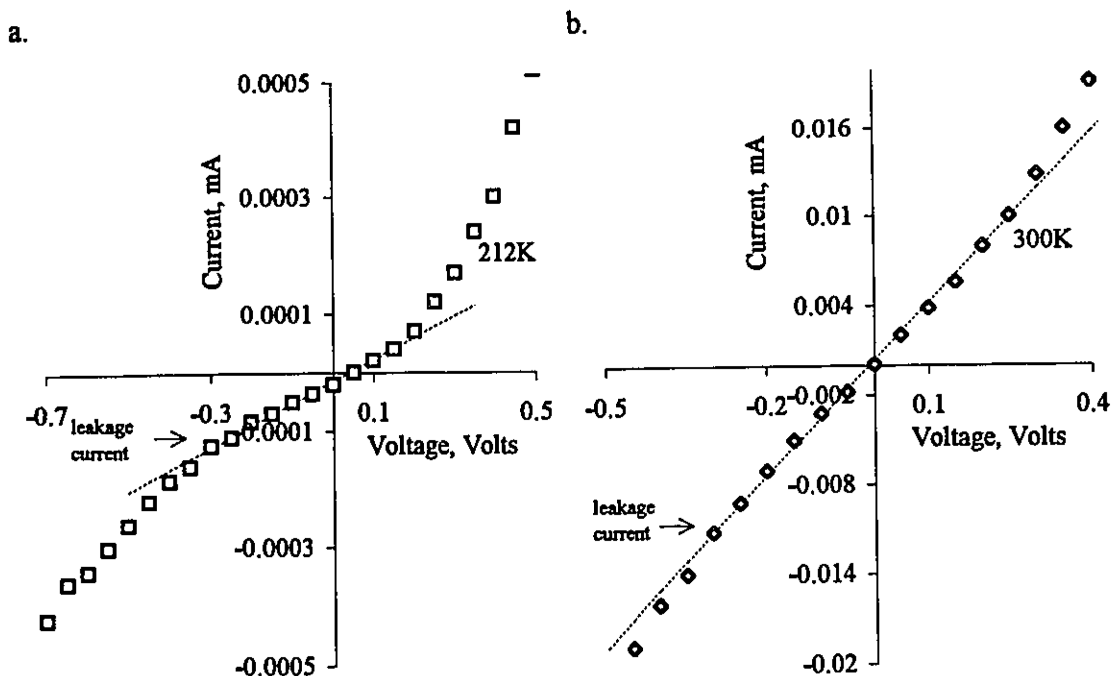

Fig. 4.6 Expanded linear region of the current-voltage characteristics, sample 2 at: a.- 212K., and b.- 300K.

The impedance of the samples has been measured at 212K and 300K in the linear part of the relationship between the current and the voltage; they are: R_S=10kΩ and R_S=5kΩ for sample 1, and R_S=2MΩ and Rs=30kΩ for sample 2. The impedance of both types of diodes is critically dependent on the leakage current, which is defined by the different layers deposited for the creation of the Schottky junction.

The results presented here appear to indicate that as expected the use of an interfacial film, leads to the enhancement of the barrier height of Schottky diodes. The experimental data for the current-voltage relationship shows that the leakage current at small applied voltages and low temperatures, becomes dominant factor in determining ϕ_B. In summary, the barrier heights for the $Au/In_{0.72}Ga_{0.28}As_{0.68}P_{0.32}/InP$ MQW samples and $Au/In_{0.7}Ga_{0.3}As_{0.64}P_{0.36}$ epilayer are presented in table 4.1.

Table 4.1 Summarized barrier heights of the quaternary epilayer and the MQWs

parameter	sample 1 MQW		sample 2 MQW with MgF_2 film		sample 4 epilayer	
	212K	300K	212K	300K	96K	160K
Au/InP barrier height, eV(±0.02)					0.74	0.75
Au/InGaAsP barrier height, eV(±0.02)	0.37	0.53	0.49	0.60	0.66	0.68
Internal field F_0, V/cm	$5.3x10^3$	$7.6x10^3$	$7x10^3$	$8.3x10^3$		

4.2 PV spectra at different temperatures

The effect of temperature on the different energy transitions observed in the photovoltaic spectra of the $In_{0.7}Ga_{0.3}As_{0.64}P_{0.36}$ epilayer lattice matched to *InP* and $In_{0.72}Ga_{0.28}As_{0.68}P_{0.32}/InP$ MQWs, is discussed in the following two sections. The evolution of each spectral feature is monitored as the temperature changes and the experimental data is fitted to Varshni's empirical relation[49] and the temperature coefficients α and β deduced (see section 2.5).

4.2.1 *InP* substrate: the PV signal evolution with temperature

First we will describe the measurement of the PV signal for the *InP* substrate, to detect the potential influence of the substrate on the optical response of the epilayer and later the complete MQW stacking. The substrate is expected to provide good electrical conductivity even at very low temperatures because of the heavy doping with sulfur. The

optical absorption within the substrate is expected to be small in the spectral region of appearance of the QW structures (900-1400nm for our samples). The energy level of the dopant impurity is usually within the band gap of the substrate, but could also occur at energies where other QW transitions are observed. To examine such a possibility, the optical response of the *InP* substrate is studied in the spectral range of 800nm-1350nm(1.55eV-0.92eV), using the photovoltaic measuring technique. The results presented in fig.4.7(for part of the studied spectrum) show a strong feature falling just above the band gap of *InP* with half-width of about 20meV. The peak appears at 22K at energy position of 1.40eV(885nm) and follows the band gap up to higher temperatures. This structure is associated with surface effects as explained by R.A. Smith in Semiconductors pp. 310-312. The substrate was carefully tested for other structures below the band gap of *InP* in the spectral region where the quantum well transitions are expected to occur. No other features were found and that is an indication of a good quality substrate, with *S* impurities showing no levels in the region of our interest. The

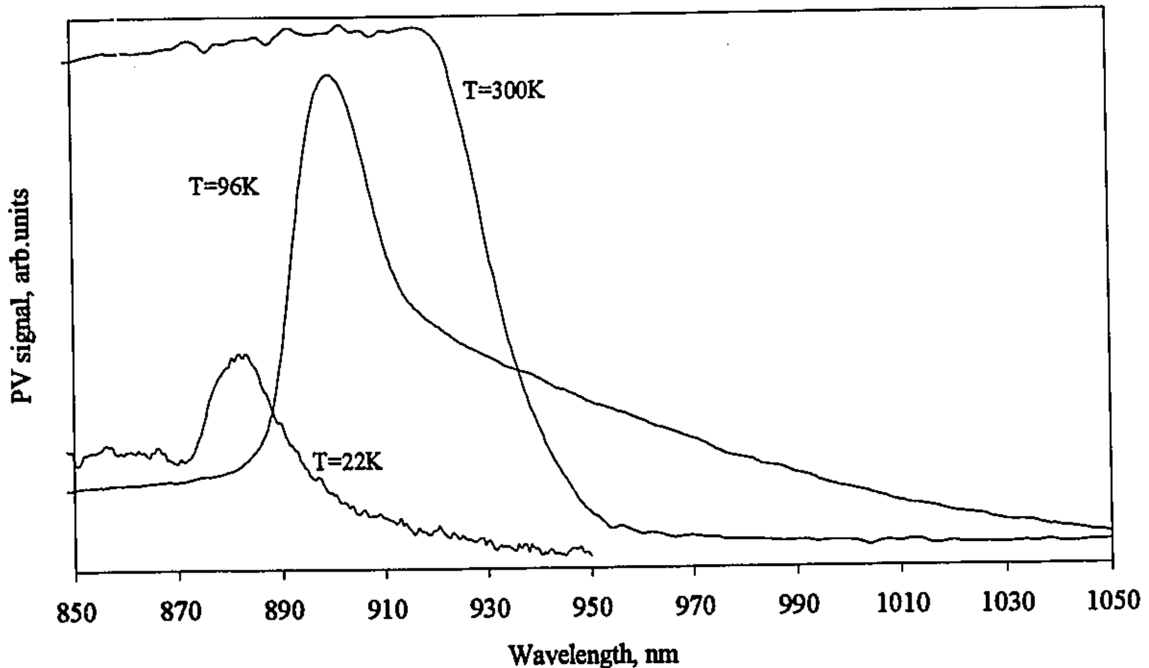

Fig. 4.7 PV spectra of the *InP* substrate at 22K, 96K, and 300K.

optical response of the complete QWs appears to have beengreatly influenced by the substrate in several studies[56,57]. It was found, that the substrate modifies the photoconductivity spectra of *InGaAs/GaAs* quantum wells and thus the interpretation of the QW peaks should be done with care.

The band gap of *InP* is evaluated from fig.4.7 to be 1.38eV at 22K. This value is consistent with the accepted value of 1.42eV at 4K[58].

In summary, we can conclude that the *InP* substrate, studied down to 22K, does not show the existence of features in the spectral region defined between the band gap of *InP*(1.4eV) and the *InGaAsP* quaternary band gap(0.9eV).

4.2.2 *InGaAsP* epilayer: temperature dependence of the PV signal

The results obtained for a 500nm thick $In_{0.7}Ga_{0.3}As_{0.64}P_{0.36}$ epilayer (sample 4) grown on *InP* substrate in the temperature interval 40K-300K are shown in fig.4.8. The PV spectra are corrected to a flat detector spectrum, to eliminate the influence of external factors, such as grating features, filters and the iodine lamp effects. The presence of water vapor band in the 1350nm-1380nm (0.92eV-0.9eV) spectral region increases the noise and makes difficult the accurate determination of the exact position of the band gap, evaluated at half of the maximum photoresponse, according to the Moss criteria [59]. For clarity the spectra are displaced, showing the shifting of the quaternary material band gap with the temperature change. The real photovoltaic signal has a maximum at about 190K. The absorption edge moves to lower energies, as the temperature increases, as expected from Varshni's equation (eq.2.40). Fig.4.9 represents the experimental results for the observed band gap energies as function of temperature. The solid curve represents a fit of the experimental data points to Varshni's equation. Because of difficulties in controlling the temperature, when two feed back systems are operating and the presence of water vapour

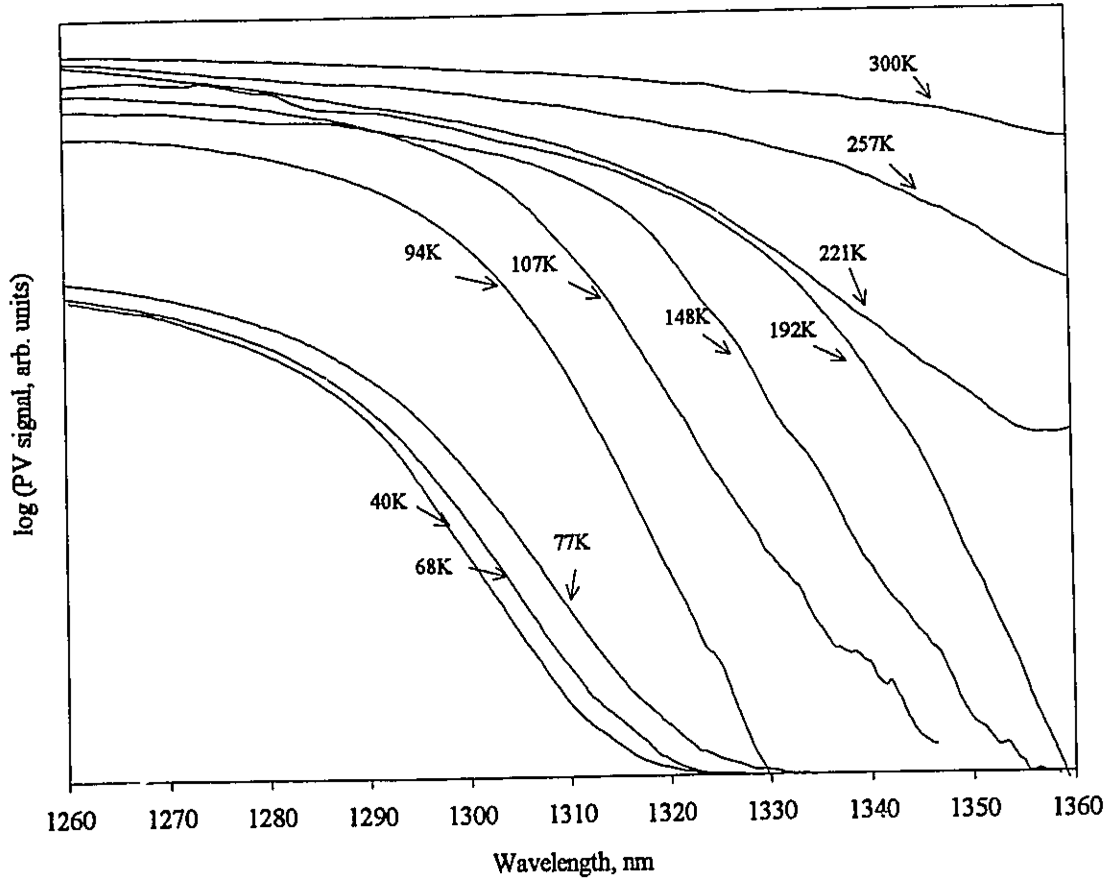

Fig. 4.8 Spectral response of $In_{0.7}Ga_{0.3}As_{0.64}P_{0.36}$ epilayer lattice matched to InP (sample 4).

band, as shown above, at T>100K the experimental determination of the band gap has a bigger degree of inaccuracy. From the fitting curve, the Varshni coefficients are deduced as follows: $\alpha=(-4.0\pm0.2)\times10^{-4} eV/K$ and $\beta=300\pm20K$.

The temperature coefficient of the band dE_g/dT is known to be almost linear for temperatures higher than 150K. From the linear fit to the experimental data in the temperature interval 150K-300K (shown with dashed line in fig.4.9), we obtain a value for $\frac{dE_{g(InGaAsP)}}{dT}=(-2.1\pm0.2)\times10^{-4} eV/K$. The epilayer was very carefully tested for any impurity peaks. Only the two barrier height features with an amplitude 1:100 to the band

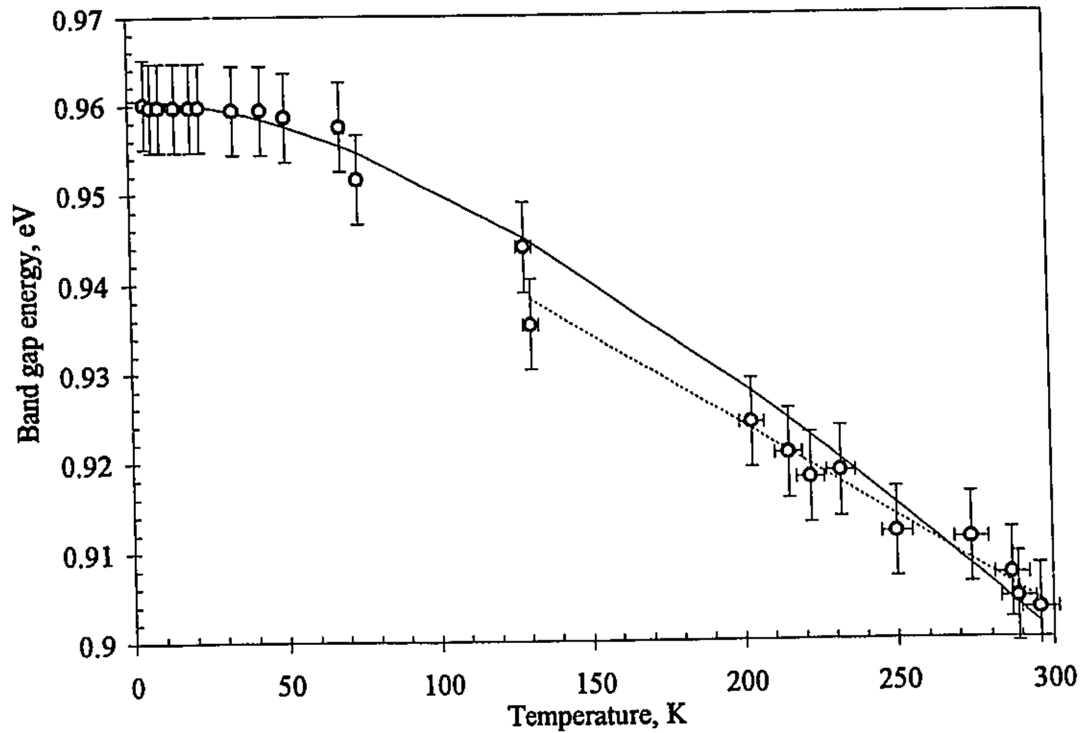

Fig. 4.9 Temperature variation of the direct band gap of the epilayer.

gap are present at very low energy side in the PV spectrum, well beyond the expected positions of the quantum well peaks.

4.2.3 *InGaAsP/InP* MQW: temperature dependence of the PV signal

The photovoltaic spectra for the complete MQW (sample 1) at different temperatures are shown in fig.4.10 for the temperature interval 4-129K and in fig. 4.11 for the temperature interval 159-275K. The MQW has complete stacking, consisting of an InP substrate, an *InP* buffer layer of 3000Å and ten periods of *InGaAsP* wells, separated by ten layers of *InP* barriers (the complete description is given in table 3.1). Four clear peaks labeled A, B, C, D, and a broad, not very well defined feature, labeled E, are present in the

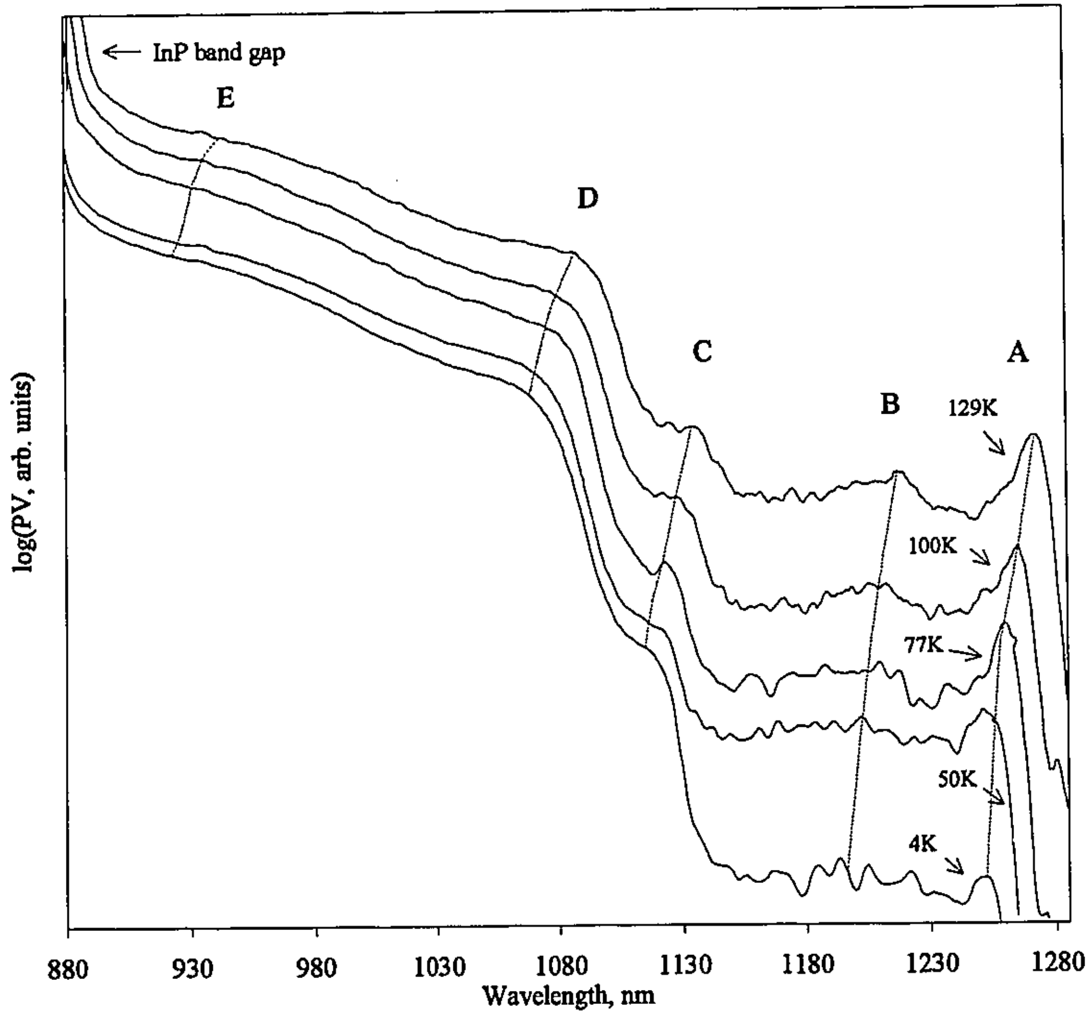

Fig. 4.10 PV spectra of $In_{0.72}Ga_{0.28}As_{0.68}P_{0.32}/InP$ MQW in the 4K-129K temperature interval (sample 1).

spectra. The evolution of each peak was observed, as the temperature was varied in the 4-275K temperature interval. For clarity the spectra are split in two different figures because the intensity of the photovoltaic signal is small at the 4-150K interval. The first peak "A" has an excitonic nature and is associated to the transition from the first heavy hole E^{hh}_1, to the first electronic state E^{e}_1, in the *InGaAsP* well. The identification of the other structures is done by fitting their positions to theoretically calculated energy transitions, through a

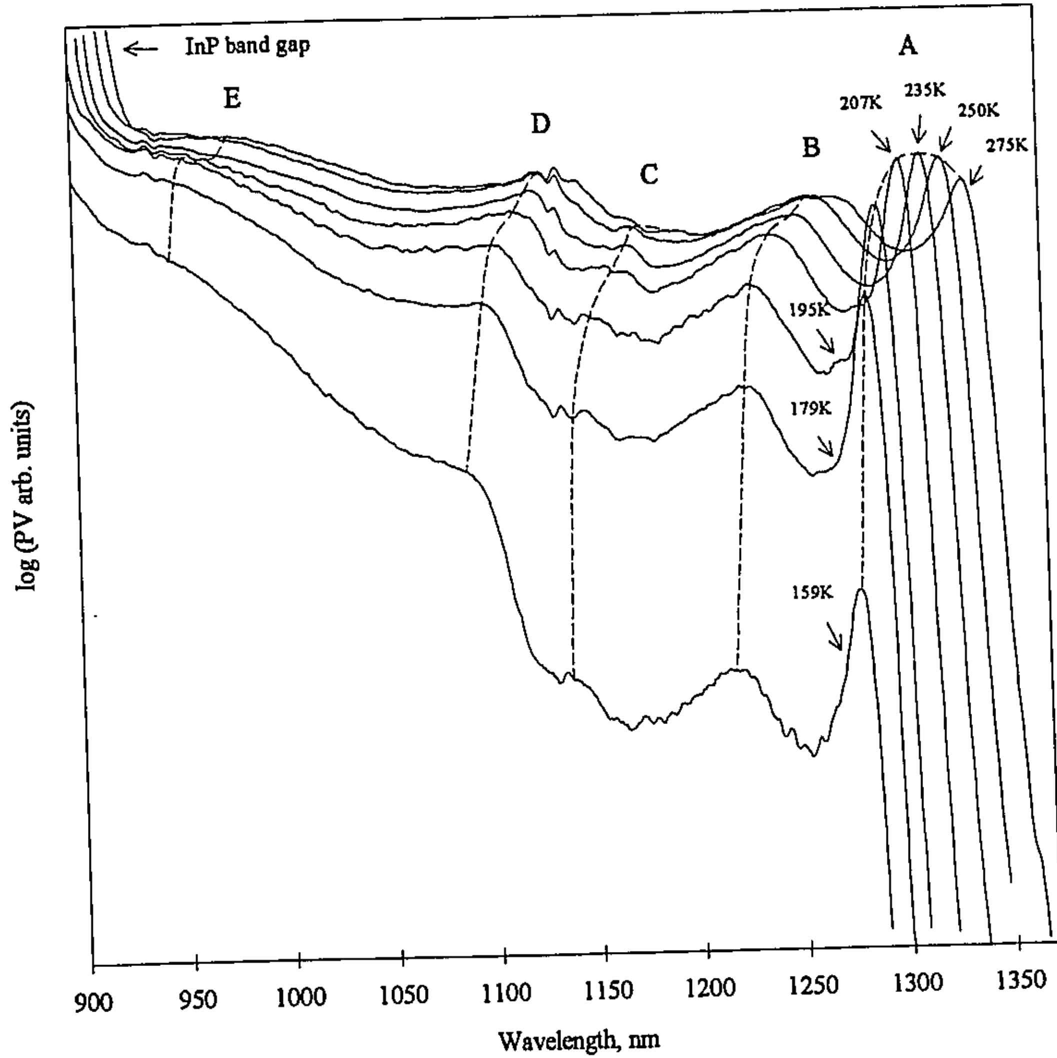

Fig. 4.11 PV spectra of $In_{0.72}Ga_{0.28}As_{0.68}P_{0.32}/InP$ MQW in the 159K-275K temperature interval (sample 1).

computer program, using the envelope function approach[28] (see section 2.2). The conduction band offset is taken as $\Delta E_c = 0.39 \pm 0.01 \Delta E_o$. There are several reports on band offsets in *InGaAsP* systems and the value we consider is the most recent one[19,p.96]. Taking also into account the barrier and the well widths, and the x and y compositions from table 3.1, the calculated and experimentally found transition energies at 4K are summarized in table 4.2. In the calculated energy values the exciton binding energy of

Table 4.2 Positions and identification of the experimental and calculated values for the energy transitions of sample 1.

Feature	Experimental position, ±0.005eV	Calculated position, ±0.005eV	Transition
A	0.989	0.998	*11H*
B	1.039	1.042	*11L*
C	1.106	1.116	*21H*
D	1.156	1.154	*12L*
E	1.331	1.350	*25H*

3meV[28] is included, so the energy of the transitions should be larger by this amount, compared to the experimental ones. The *mnH/L*(Γ/Π) refers to transitions from heavy(*H*) or light(*L*) holes of the *m* valence subband to the *n* conduction band; and Γ and Π corresponds to the center, or the edge of the minizone. For the MQW samples studied here we consider transitions at Γ point only. The identification of all structures is in good agreement with the envelope wave function calculations; peak E shows a slightly greater discrepancy between the experimental and calculated value. This is explained by the fact, that *25H* is not a very probable transition and appears in the experimental spectrum as a broad peak, close to the *InP* band gap whose exact position determination is not very accurate. The same procedures are used in the identification of the energy transitions in other QW systems and the experimental results show good agreement with the envelope wave function calculations [60,61].

The spectral response of sample 3 (the strained sample) at two temperatures is shown in fig.4.12. Two well defined structures labeled A and B are present in the PV spectrum at 100K. The computer program based on the envelope function approximation identifies the first peak A, as a transition from the first light hole state-E^{lh}_1 to the first electron state-E^{e}_1 and the second feature, as a transition from the first heavy hole state-E^{hh}_1 to the first electron state-E^{e}_1. The appearance of the light hole transition before the

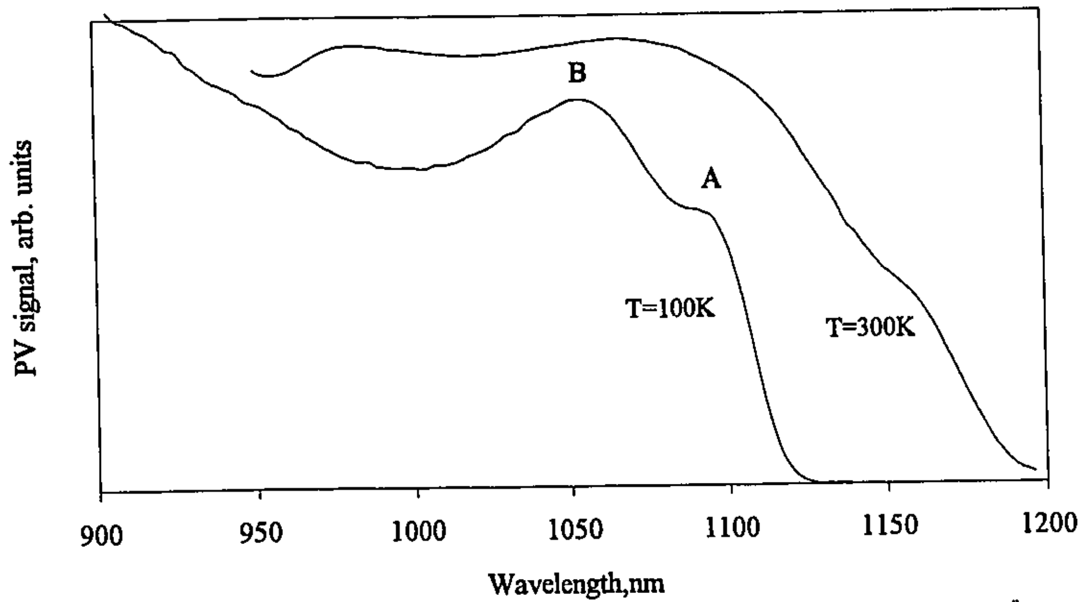

Fig. 4.12 PV spectra for $In_{0.68}Ga_{0.32}As_{0.56}P_{0.44}/InP$ MQW at 100K and at 300K (sample 3)

Table 4.3 Spectral features identification for sample 3

Feature	Calculated transition, ±0.005eV	Experimental transitionPL- 4K, ±0.005eV	Experimental transitionPV- 100K, ±0.005eV	Transition
A	1.123	1.119	1.129	*11L*
B	1.138	1.167	1.177	*11H*

heavy one is due to the larger mismatch of 0.43% between the *InGaAsP* wells and the *InP* barriers. The spectral features are identified and summarized in table 4.3, with again an exciton binding energy of 3.5meV included in the calculations. The experimental positions of each peak for sample 1 in the temperature interval 4K-275K are fitted to eq.2.40 (Varshni's equation) and shown in fig.4.13. The figure consists of all the experimental data points and the fitting curves for A through E structures and the *InP* band gap. The estimated errors for the temperature are 2% and 0.5meV for the spectral position

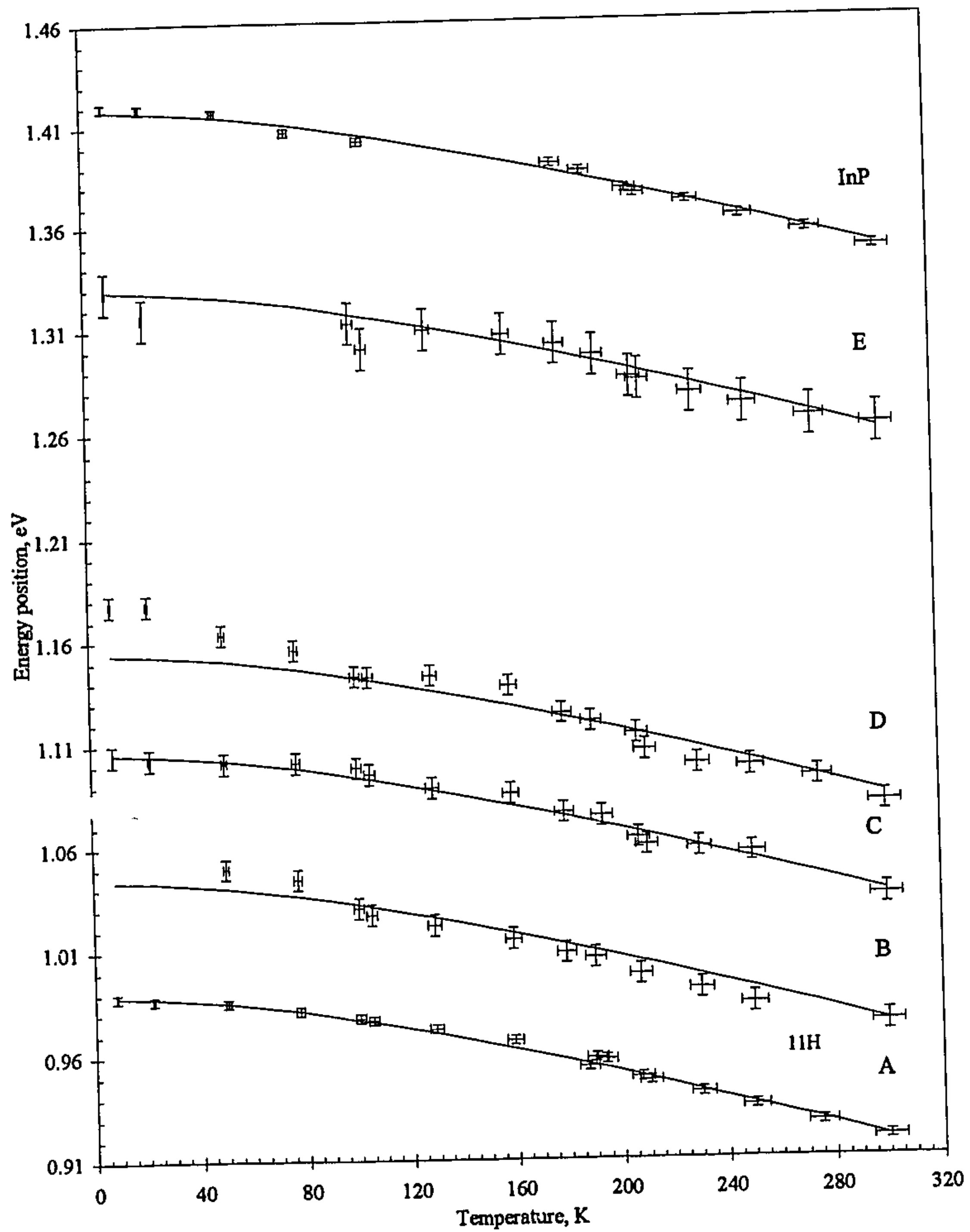

Fig. 4.13 Position shift of the spectral structures observed in the PV spectra of sample 1.

identification. Some of the experimental points have small fluctuations off the fitting curves for the same reasons as in the previous section. There were some difficulties with the position identification, because the spectrometer grating has a defect centered around 1178nm(1.05eV), and at temperatures higher than 180K the real peak position of feature C is mixed and broadened. To eliminate the influence of the grating structures and filters, all spectra are corrected to a flat detector spectrum, before determination of the peak positions. Fig.4.14 shows in greater detail the evolution of the excitonic peak "A" with temperature. The experimental data fit to eq.2.40 gives the following Varshni coefficients: $\alpha=(-4.4\pm0.2)\times10^{-4}eV/K$ and $\beta=270\pm20K$. From a linear fit in the temperature interval 150K-300K (shown with dashed line in fig. 4.14) the deduced linear temperature coefficient of the band gap is: $\frac{dE_{g(InGaAsP)}}{dT}=(-3.4\pm0.2)\times10^{-4}eV/K$. Applying the interpolation method for the linear temperature coefficient, eq.1.2 will have the form:

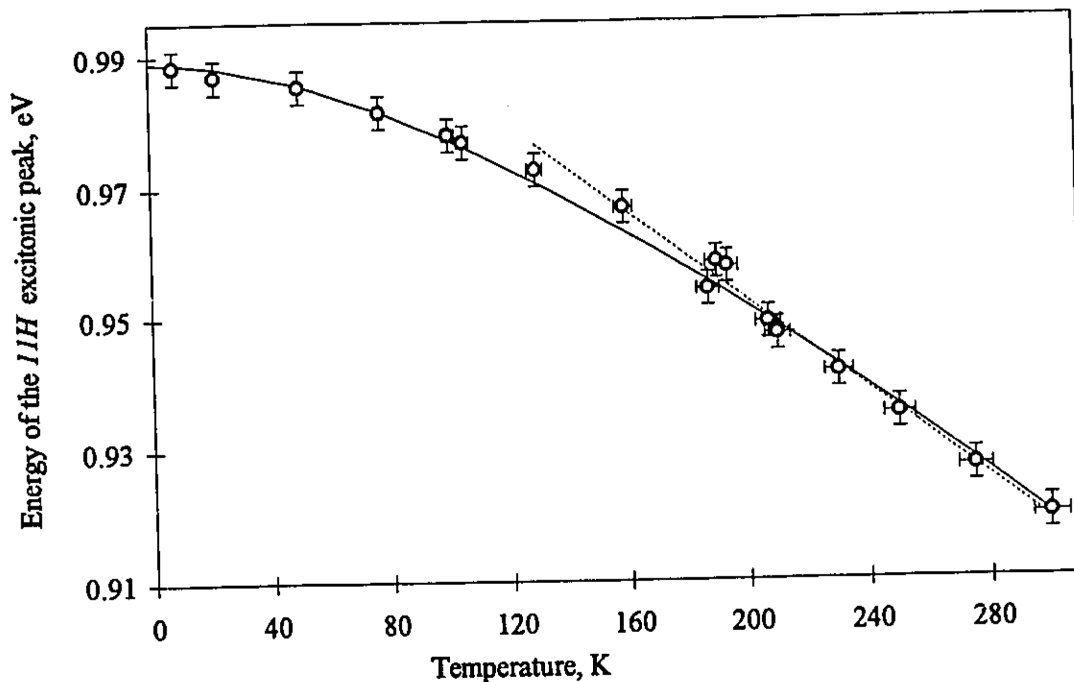

Fig. 4.14 Excitonic *11H* peak shift with temperature for sample 1(MQW).

$$\frac{dE_{g(InGaAsP)}}{dT} = (1-x)y\frac{dE_{g(InAs)}}{dT} + (1-x)(1-y)\frac{dE_{g(InP)}}{dT} + xy\frac{dE_{g(GaAs)}}{dT} + x(1-y)\frac{dE_{g(GaP)}}{dT}, \qquad (4.3)$$

where $dE_{g(xy)}/dT$ are the temperature coefficients for the former binaries. Taking the values for $dE_{g(xy)}/dT$ summarized by S. Adachi [19, p.104], the interpolation method gives: $\frac{dE_{g(InGaAP)}}{dT} = -3.8 \times 10^{-4} eV/K$ for x=0.28 and y=0.68 compositions. The last result shows good agreement with our experimental value. Varshni's coefficients have been compared to other works, the values obtained by Satzke et al.[14]: α=-4.3x10^{-4}eV/K and β=224K are also very close to the ones we found.

Structures B to E (fig.4.13), showing temperature shift of *11L*(Γ), *21H*(Γ), *21L*(Γ), and *25H*(Γ) transitions appear to follow the same fit as the excitonic *11H* line, and for all of them α=(-4.4±0.2)x10^{-4}*eV/K* and β=270±20*K*. This result is also consistent with α=(-4.0±0.2)x10^{-4}*eV/K* and β=300±20*K* found above (section 4.2.2) for the quaternary epilayer.

In conclusion to this section, we show that the quantum well peaks are not influenced by the *InP* substrate. All identified quantum well transitions are in good agreement with the theoretically calculated ones and also all features follow the same fit with the temperature variation, differing only by the zero Kelvin energy for each peak, which is an indication of the quality of the system growth.

4.3 Field dependent effects

The effect of an external electric field on the MQW samples will be presented in this section. The *Au* Schottky barrier deposited on each sample results in the formation of an internal field even in the absence of an externally applied voltage. This field can be determined from the barrier height of the MQW found in section 4.1.2 and is given by the formula[62,p.47]:

$$F_o = \frac{\phi_B}{qd} , \qquad (4.4)$$

where d is the nominal thickness of the layers, across which the voltage is applied. We assume that the field is evenly distributed across a nominal thickness of d=0.7μm (ten layers of *InGaAsP* wells with thickness 80Å each, separated by ten layers of *InP* barriers with thickness 3200Å each, and a buffer layer of *InP* with thickness 3000Å). The *InP* substrate is not included in d, because it is conducting even at low temperature. Taking our experimental values for ϕ_B=0.53eV at 300K and ϕ_B=0.37eV at 212K for sample 1, we have internal fields F_O=7.6x10^{3}V/cm at 300K and F_O=5.3x10^{3}V/cm at 212K. For sample 2, where the barrier heights are ϕ_B=0.60eV at 300K and ϕ_B=0.49eV at 212K eq.4.4 gives: F_O=8.6x10^{3}V/cm at 300K and F_O=7.0x10^{3}V/cm at 212K.

4.3.1 Electric field dependence of the QW peaks

The effect of external applied voltages on the quantum well transitions for sample 1 at two different temperatures are shown in fig. 4.15. The corresponding external electric fields can be calculated by the formula[62, p.47]:

$$\left|\vec{F}\right| = \left|\vec{F}_o\right| - \frac{V}{d} , \qquad (4.5)$$

where V is the applied bias voltage. From the last relation we can see that the field becomes stronger, when a negative voltage is applied to the *Au* electrode and becomes weaker, when a positive voltage is applied. From eq.4.5, the corresponding electric fields are calculated to vary from F=1.5x10^{4}V/cm to F=4.9x10^{3}V/cm, at 200K and from F=1.9x10^{4}V/cm to F=1.6x10^{3}V/cm, at 96K, for applied voltages ranging between V=-0.7V and V=0V, at 200K, and from V=-1V to V=0.23V, at 96K. The position of the quantum well peaks is examined at each applied voltage and the observations show small

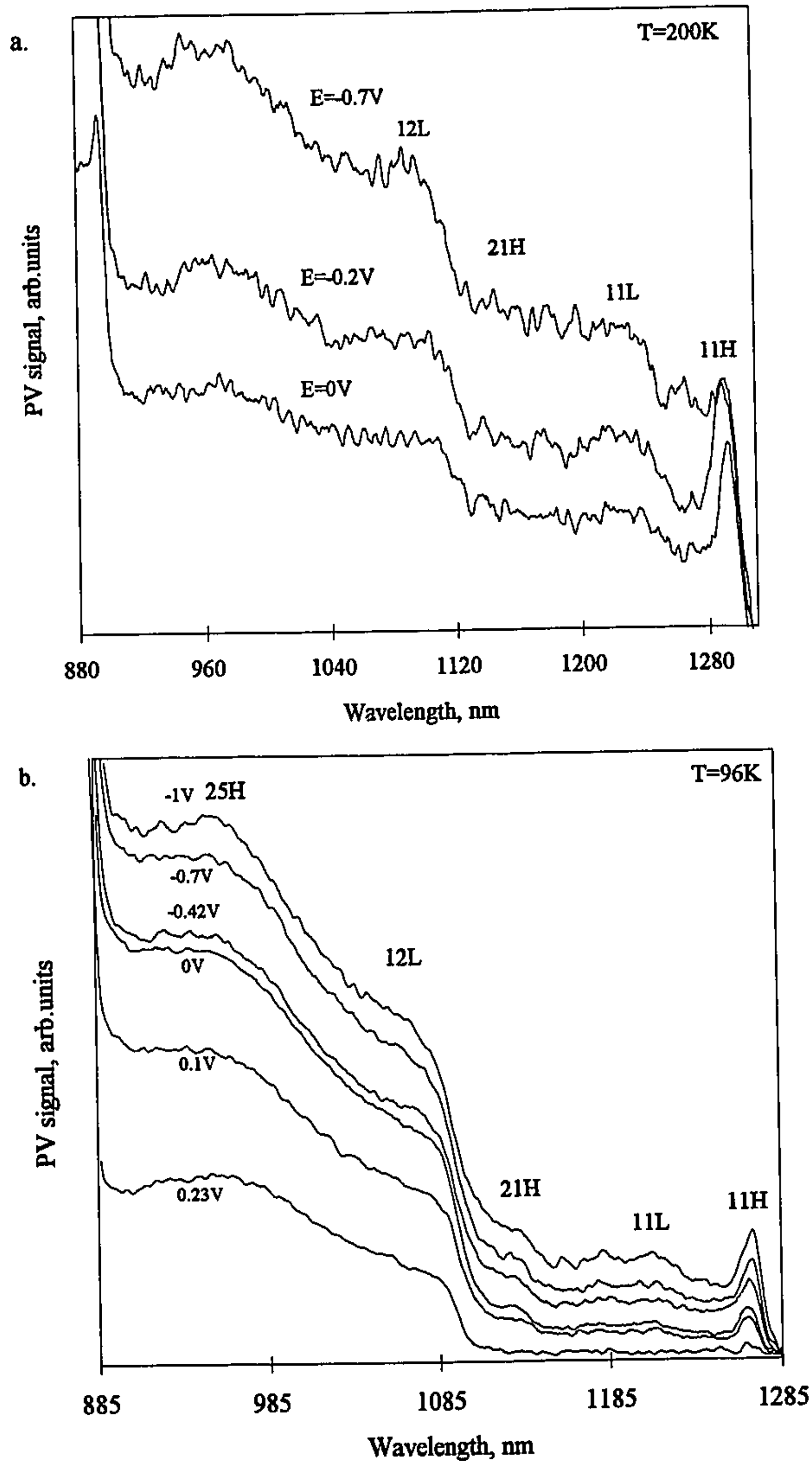

Fig. 4.15. Field dependence of the PV spectra structures of sample 1 at a.-200K and b.-96K

red shift for *25H*, and *21H* transitions at 96K. The *12H* and *12L* peaks get stronger with the increase in the field, but do not show significant energy shift. The behavior of these transitions at 200K, shown in fig.4.15a, indicates no significant change of the relative intensity and no significant spectral shifting. Only the collected photovoltaic signal increases with the reversed bias. The same observations for the QW transitions with energies higher than the *11H* exciton are found in ref.44 on *GaAs/AlGaAs* MQWs using photocurrent spectroscopy, and suggest that the subbands with higher energy show small changes in the peak energies for electric fields below $3x10^4$V/cm.

The spectral region of the *11H* excitonic transition is expanded to higher resolution for detailed observations- fig. 4.16-212K and fig.4.17-96K and 300K. The PV signal of

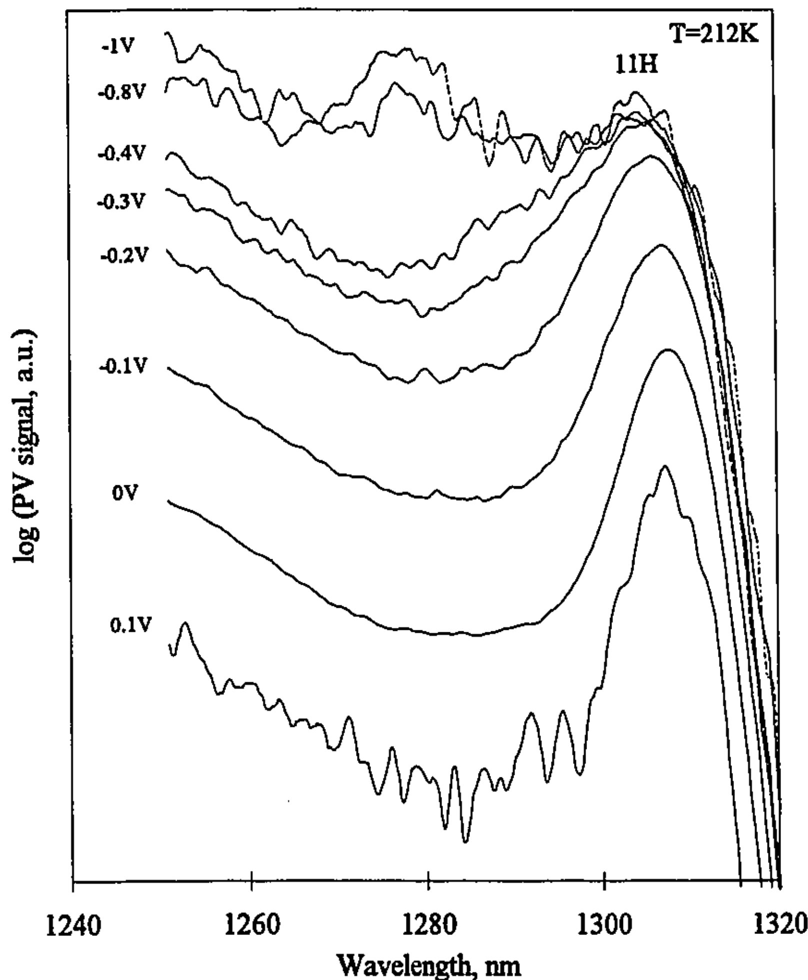

Fig.4.16. The effect of an applied electric field on the PV spectra in the *11H* excitonic region at 212K for sample 1.

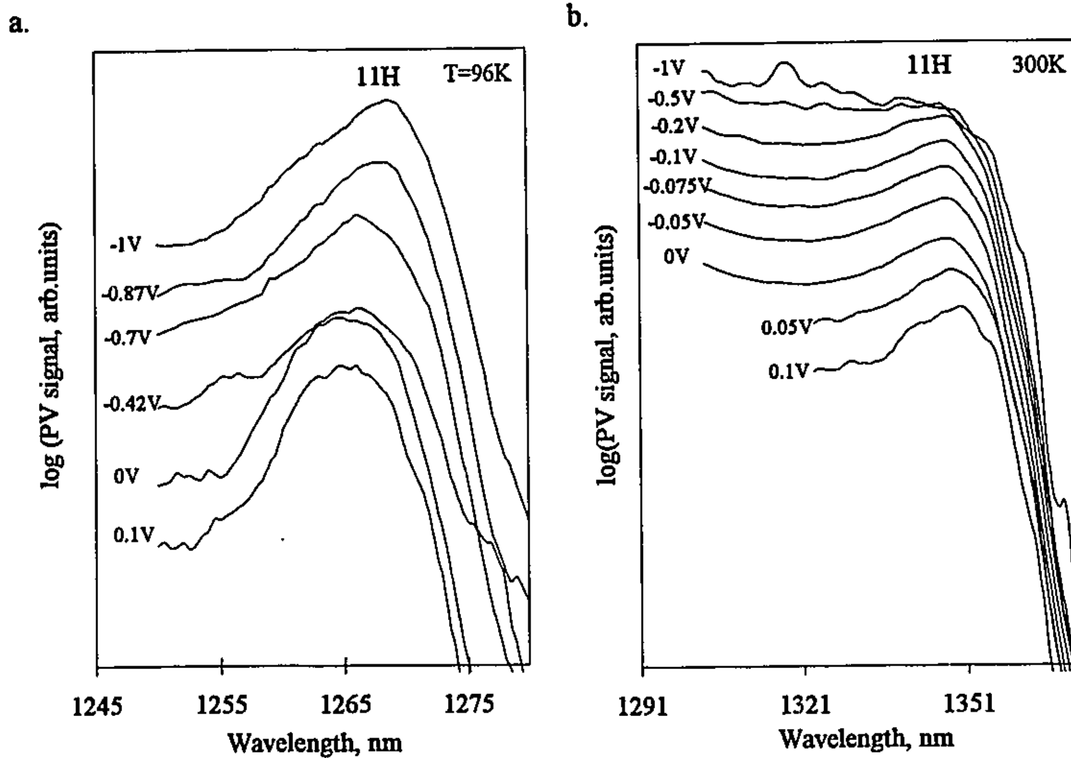

Fig. 4.17 The effect of the electric field on the PV spectra in the *11H* excitonic region for sample 1 a.-at 96K and b.-at 300K.

the *11H* peak is determined at each applied voltage. The field is varied by small steps, which allows for analyses of the shape and the spectral shifting of the excitonic line. The PV signal increases with the increase in the field. The effects of the electric field are best observed at T=212K because the maximum intensity of the PV signal is around this temperature. With the negative bias voltage increase the excitonic strength wakens; the peak gradually widens and disappears at about V=-0.45V(F=1.17x10^4V/cm). There is a spectral shift to higher energy side by approximately 3meV across the range. Also, at higher applied negative bias (above V=-0.8V) the appearance of a new peak is observed. Each of these effects will be discussed separately. First the broadening of the excitonic line with the applied electric field detected at 212K is shown in fig.4.18. The half width, at half maximum changes by a factor of two. The exciton oscillator strength weakens since the

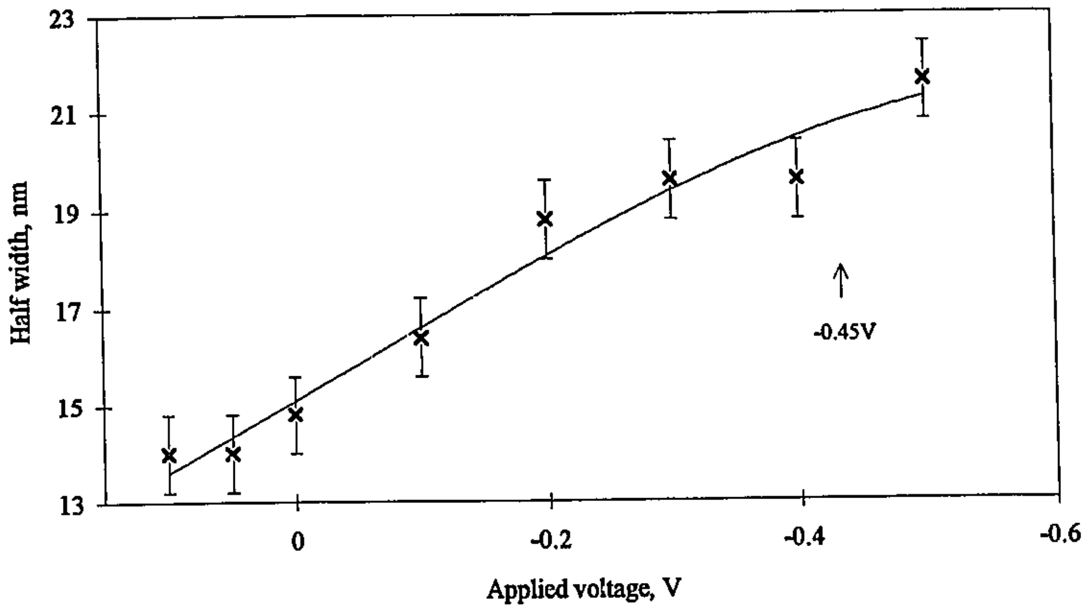

Fig. 4.18 Broadening of the excitonic *11H* peak of sample 1 at 212K

electron and the hole are increasingly separated. Beyond approximately V=-0.45V (F=1.17x10^{4}V/cm) the half width half maximum signal increases rapidly and the peak disappears, indicating ionization of the exciton. This break down field is in good agreement with the theoretical predictions given by eq. 2.38 which gives the critical field of F_c=(1.02÷1.21)x10^{4}V/cm. The broadening effects at 96K and 300K are not well resolved, because of the small PV signal in the exciton region and are not included in fig.4.18.

The excitonic shifts with the increase in the field at 96K and 212K for sample 1 are shown in fig.4.19 and fig. 4.20. The position of the *11H* peak at each applied voltage is determined. A total spectral shift of approximately 3meV is measured for each temperature. The shift observed at 212K is oriented to higher energies contrary to the one at 96K, which is oriented to lower energies. In the theoretical part we discussed the contribution of the subband energies and the exciton binding energy to the ground state exciton shift which is shown in eq.2.37. The reason that the exciton peak shows reversed

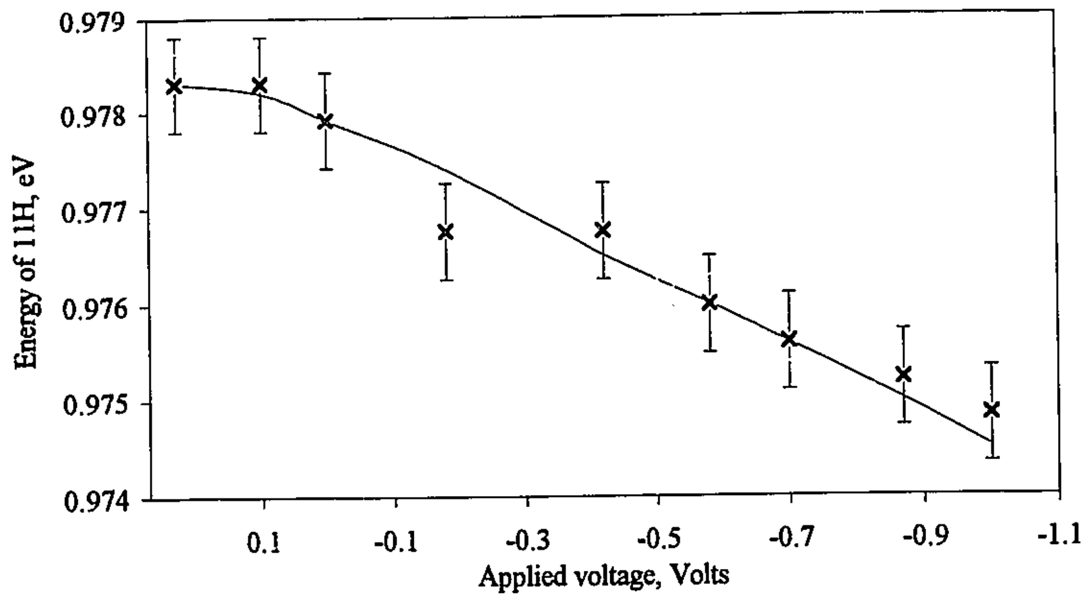

Fig.4.19. Position shifts of the excitonic peak *11H* with an applied electric field for sample 1 at 96K.

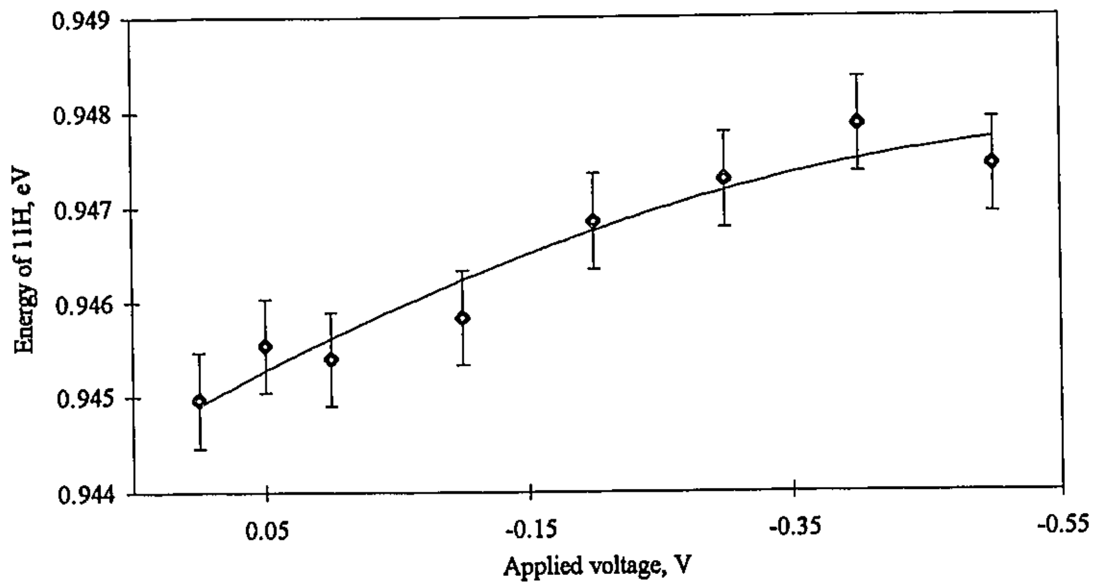

Fig. 4.20. Position shifts of the excitonic peak *11H* with an applied electric field for sample 1 at 212K.

displacement at 212K is possibly due to the fact that the exciton binding energy is affected by the field to a greater extent than the effective band gap for higher applied reversed bias

voltages. The resultant excitonic peak shifts also to higher energies at this temperature. The actual influence of the exciton binding energy in the observed shifting is not known for the quaternary *InGaAsP/InP* MQWs and we can only estimate it from our experimental observations. Our results are similar to the behavior of some semiconducting superlattices of *GaAs/AlGaAs* under a strong applied electric field, where the Stark shift is oriented to higher energies, due to an increase in the exciton binding energy[63] or field tunneling processes between the different wells[64].

At electric fields below 7.7x10^{3}V/cm, the PV spectrum of sample 1 at 212K shows the *11H* exciton peak corresponding to an allowed transition -fig.4.16. As the electric field increases, a new peak appears in the spectral region between the *11H* and *11L* allowed transitions, and is identified as *12H* forbidden transition with an energy of 0.966eV at 212K, compared to 1.029eV at 4K from the theoretical calculations. The appearance of the $j \neq i$ transition can be explained in terms of deformation of the well potential by the electric field. At zero applied field, the well wavefunctions are orthogonal and the selection rules are valid for optical transitions between hole and electron subbands. When an electric field is applied perpendicular to the well, the electron and hole wave functions in the QW are no longer orthogonal. The deformation of the potential increases with the increase in the electric field, which results in greater probability for the appearance of forbidden transitions. In addition, the subbands near the band edge are affected to a greater extent by the potential deformation and transitions close to it are more easily observed. This is consistent with the experimental results shown in fig. 4.16. The *12L* transition is the first forbidden transition from the band edge and is clearly observed.

Electric field effects on *InGaAsP/InP* MQW p-i-n structures using electroabsorption techniques have been studied by J. E. Zuker et al.[12] and the measured Stark shift of the *11H* excitonic transition was found to be enhanced over that of the corresponding ternary wells . A comparison with our results is difficult to make, since our well and barrier thicknesses are different. In the case of ref.12, the observations were

made on high quality samples with intense exciton absorption peaks and the energy shift exceeded the excitonic linewidth; the photocurrent spectra of *InGaAsP/InP* MQWs also showed red shift with increasing reverse bias voltage.

Sample 2 displays similar behavior as sample 1 at 212K. The PV spectra in the *11H* region for different applied voltages at 212K and 300K are shown in fig.4.21. The electric fields are varied between F=8.3x10^{3}V/cm and F=3x10^{4}V/cm, at 300K and between F=5.6x10^{3}V/cm and F=2x10^{4}V/cm, at 212K. The existence of an insulating layer explains the exciton resistance up to much higher applied voltages. We assume that most of the voltage is applied across the insulating layer and that the actual field applied across the quantum well is relatively small. This is consistent with the small energy shift of the *11H* exciton. No appearance of forbidden transitions is noted, confirming that there is small change in the electric field across the MQW. The spectral shift is less than 1meV for

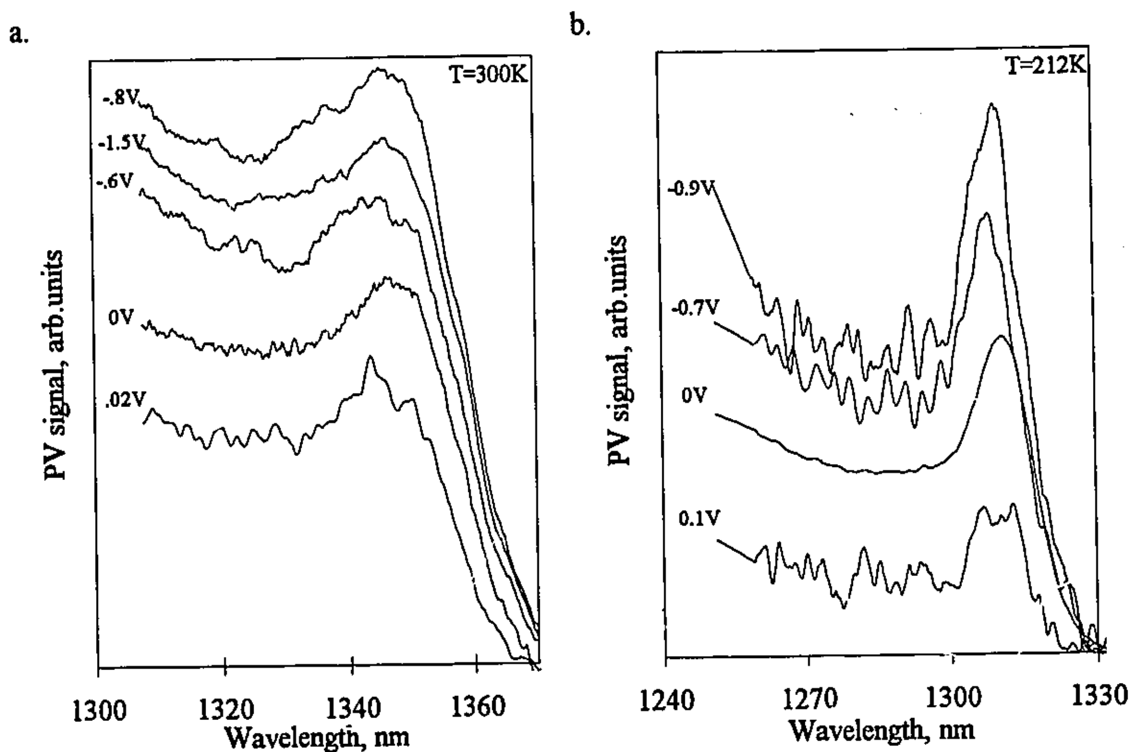

Fig. 4.21 The effect of an applied electric field of the *11H* excitonic peak for sample 2: a.-at 300K and b.-at 212K.

both temperatures and is again oriented to the higher energy side. For the observation of more pronounced changes in the exciton peak much higher voltages need to be applied; however as the field increases, the signal/noise ratio also increases and makes accurate measurements impossible.

We have also studied the electric field effects on the strained sample (*InGaAsP/InP* MQW). Fig.4.22 shows the effect of the applied field on the *11H* and *11L* transitions at 100K. The field is varied between F=2.8x10^{3}V/cm and F=1.1x10^{4}V/cm (V=0.1V-V=-0.5V). With the increase of the reverse bias voltage, the light hole transition disappears (beyond V=-0.2V) and the heavy hole transition becomes stronger; also the *11L* peak shifts to lower energies and the *11H* experiences small blue shift in consistence with the other samples.

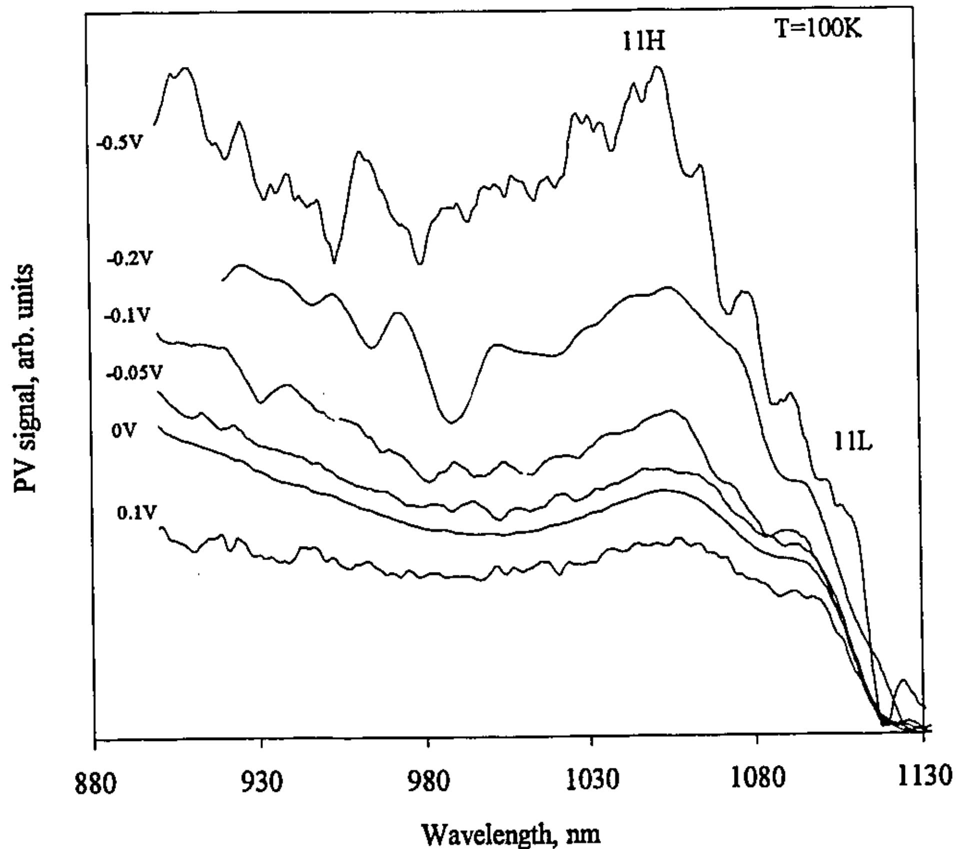

Fig. 4.22 PV signal of sample 3 for different applied voltages.

4.3.2 The integrated photovoltaic signal as function of the applied voltage and temperature

In this section we will present the change in the amplitude of the photovoltaic signal with the applied voltage for sample 1 in the vicinity of the *11H* transition. Also the thermal ionization of the exciton at zero applied voltage will be analyzed. The electric field is applied in the direction perpendicular to the layers of growth. Fig. 4.23 presents the corrected PV signal amplitude corresponding to the *11H* excitonic transition for sample 1. With the increase in the reverse bias voltage, the PV signal increases steeply up to about -0.1÷-0.2V at 300K and -0.2÷-0.35V at 212K, where it reaches a maximum. Beyond these

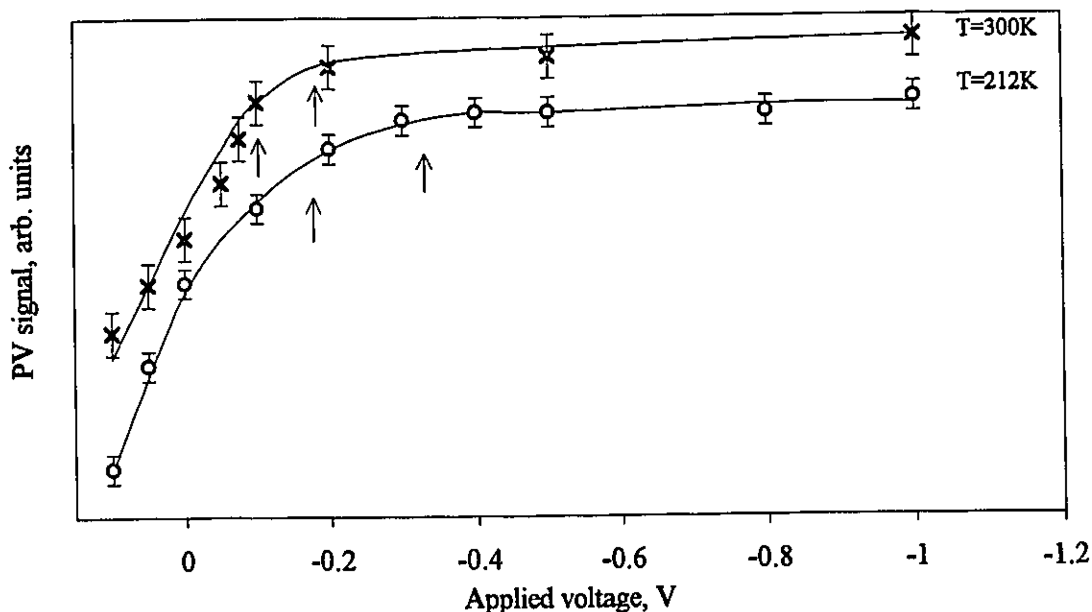

Fig. 4.23 Maximum of the PV signal at the *11H* peak for sample 1 as function of the applied voltages

voltages, the signal varies slowly with the increase in the field, as a result of Ohm's law. The error bars indicate the experimental uncertainty in the determination of each point. The saturation point for each temperature is different; it appears that at higher temperatures the field ionization of the exciton becomes easier, due to the thermal

broadening effects and the saturation point moves towards lower applied fields - fig.4.23. Our observed values for the critical reverse biases needed to dissociate the exciton are approximately -0.2÷-0.4V at 212K and -0.1÷-0.2V at 300K. These values give critical fields of F=8.2x10^3÷1.1x10^{4}V/cm at 212K and F=9.0x10^3÷1.0x10^{4}V/cm at 300K, which show good agreement with the theoretical one: F_c=(1.02÷1.21)x10^{4}V/cm. The results in fig.4.23 are also consistent with the electric field dependence of the half width half maximum of the excitonic peak studied in section 4.3.1. The same general behavior of the photogenerated signal with the applied voltages has been observed in *InGaAs/GaAs* QWs and a saturation point found at about -0.2V at 77K[65, p.51].

The area of the excitonic *11H* peak at different applied voltages was examined also for sample 1-fig.4.24. The experimental results show again a saturation point for the collected PV signal at about -0.4V at 212K, -0.3V at 300K, and beyond -1V at 96K.

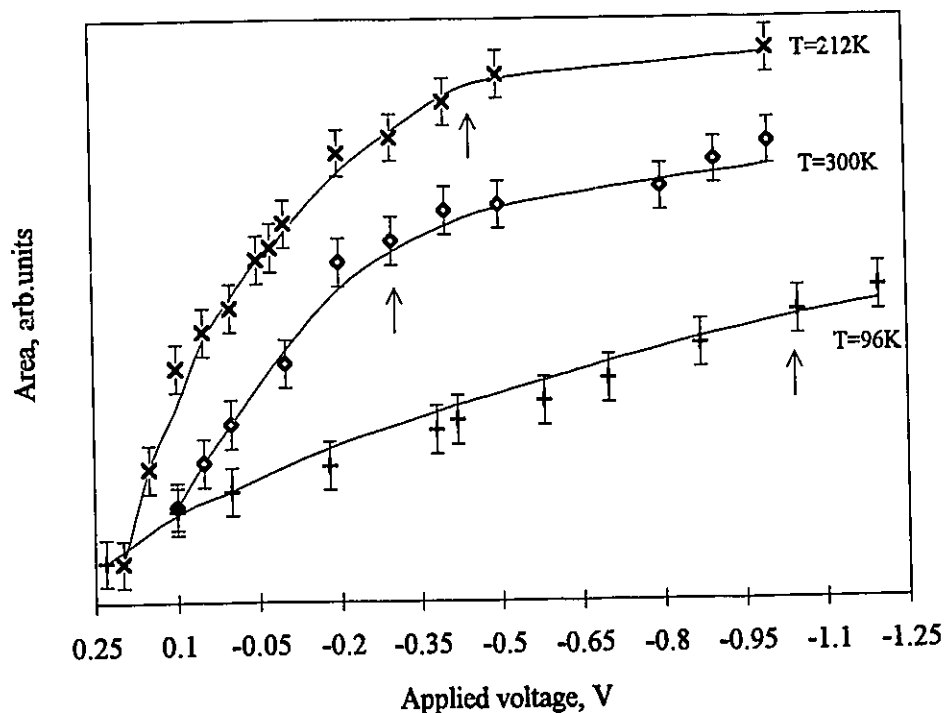

Fig. 4.24 Area change of the excitonic *11H* peak with the applied voltage for sample 1 at 96K, 212K, and 300K.

To find the thermal ionization energy, the integrated area of the excitonic peak was studied as function of temperature at zero applied field. The PV measuring technique was used to detect the *11H* peak response to the temperature changes between 22-275K. The results of these observations are summarized in fig. 4.25. From the experimental data, the PV signal starts to saturate at approximately 150-180K. Therefore, the critical temperature T_c at which thermal ionization becomes important correspond to an energy of $T_c k$=12.9÷15.5meV. This experimental finding is within experimental error of the ionization energy calculated in section 2.2 (E_{ion}=12.8÷15.3meV). T_c for *InGaAs/GaAs* QWs found by the same technique was 81K corresponding to the exciton binding energy of 7meV in those samples[67].

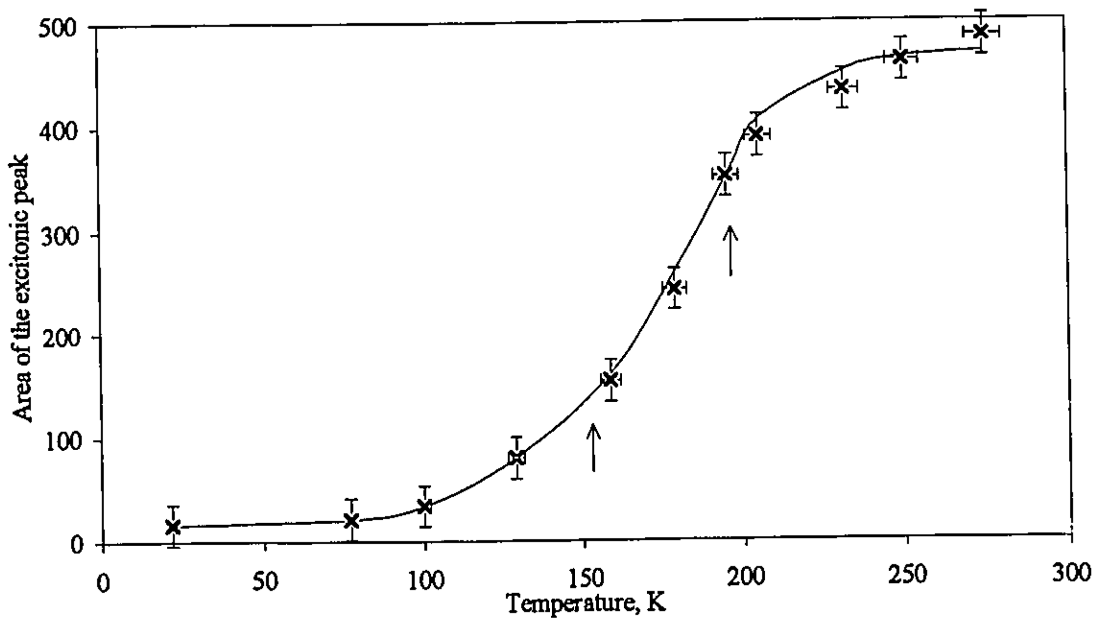

Fig. 4.25 The area change of the excitonic *11H* peak with temperature at zero applied voltage for sample 1.

transitions - the increase in the PV signal with the increase in the reverse bias voltage, the broadening and spectral shifting of the excitonic peak are analyzed and summarized. We show that the total dissociation of the exciton, caused by an external electric field leads to PV signal saturation at bias voltages of about -0.2÷-0.4V at 212K, and -0.1÷0.2V at 300K (corresponding to fields of $8.2 \times 10^3 \div 1.2 \times 10^4$V/cm at 212K, and $9.0 \times 10^3 \div 1.0 \times 10^4$V/cm at 300K). We also find 12.9÷15.5meV thermal ionization energy for the exciton at zero bias, which is in good agreement with the theoretically calculated value of 12.8÷15.3meV. The field dependent reduction of the exciton binding energy has been measured for *InGaAs/GaAs* single QWs and found to be of the order of a millielectron volt for fields reaching 8×10^4V/cm[66].

4.4 The double beam experiment

Recently, there has been considerable interest in the experimental[50,67-72] and theoretical[69,71-75] studies of nonlinear optical effects in QWs. The combination of nonlinear optics and quantum confinement gives physical insight into the unusual and practically useful properties of quasi-bidimensional semiconductor heterostructures.

Excitation-dependent optical effects in semiconductors, called optical nonlinearities, arise when the excitation intensity is sufficiently strong to modify the optical properties of the material. This normally occurs when the optical fields are of the order of or larger than the internal fields that exist in the material[67]. In linear optics for example the absorption coefficient α and the refracting index n depend on the frequency of the incident radiation and a second low intensity beam focused on the surface of the semiconductor will not influence α or n. This will no longer be the case in nonlinear optics, where intense beams interfere within the sample and create states with new properties. The basic mechanisms responsible for the nonlinear effects are different,

depending on the spectral region and type of excitation, which generate real or virtual excited-state populations.

The experimental and theoretical research shows that semiconductor QW structures exhibit unusually large optical nonlinearities[67,68]. In QWs, the internal fields (section 4.3) can be screened by photogenerated carriers changing the absorption coefficient at wavelengths near the band edge. Thus, the photomodulation of the internal electric fields through photocarrier creation causes effective nonlinearities[68].

In a typical nonlinear optical experiment the intense beam called "the pump" is used to modify the properties of the sample. The changes are measured by applying the second weak beam called "the probe". The photomodulation in our study is defined as the changes in the internal field of the sample introduced by the pump beam intensity variation. The results presented in this section were obtained on *InGaAsP/InP* MQWs (sample 1 and 2). A *He-Ne* laser (λ=632.8nm) with total beam output of 10mW is provided as the pump beam; the intensity on the sample was varied by inserting different neutral density filters. We use the PV technique to generate the probe beam with an intensity of I_p=1.5x10^{-5}W/cm^2, which is five magnitudes less than the pump beam and obviously too weak to introduce any nonlinearities (see section 3.4 for the experimental set-up diagram). The changes in the PV signal collected from the Schottky electrodes in the presence of the pump and probe beams near the *11H* exciton peak are measured at 212K and at 300K. The experimental results obtained for sample 1 at 212K and 300K, are shown in fig.4.26. The spectral interval 1280nm-1380nm (0.966eV-0.896eV) represents the region of *11H* exciton transition. The photogenerated signal scanned at four pump beam intensities, I=1.3W/cm^2, I=0.13W/cm^2, I=13mW/cm^2, and I=6mW/cm^2 , is well resolved at both temperatures. For clarity the spectra are equally displaced to each other without taking into account their real amplitude. An actual decrease of three times at 300K and of 1.3 times at 212K for the overall collected PV signal is measured, as the intensity of the second beam increases from I=6mW/cm^2 to I=1.3W/cm^2 (fig. 4.27a). This

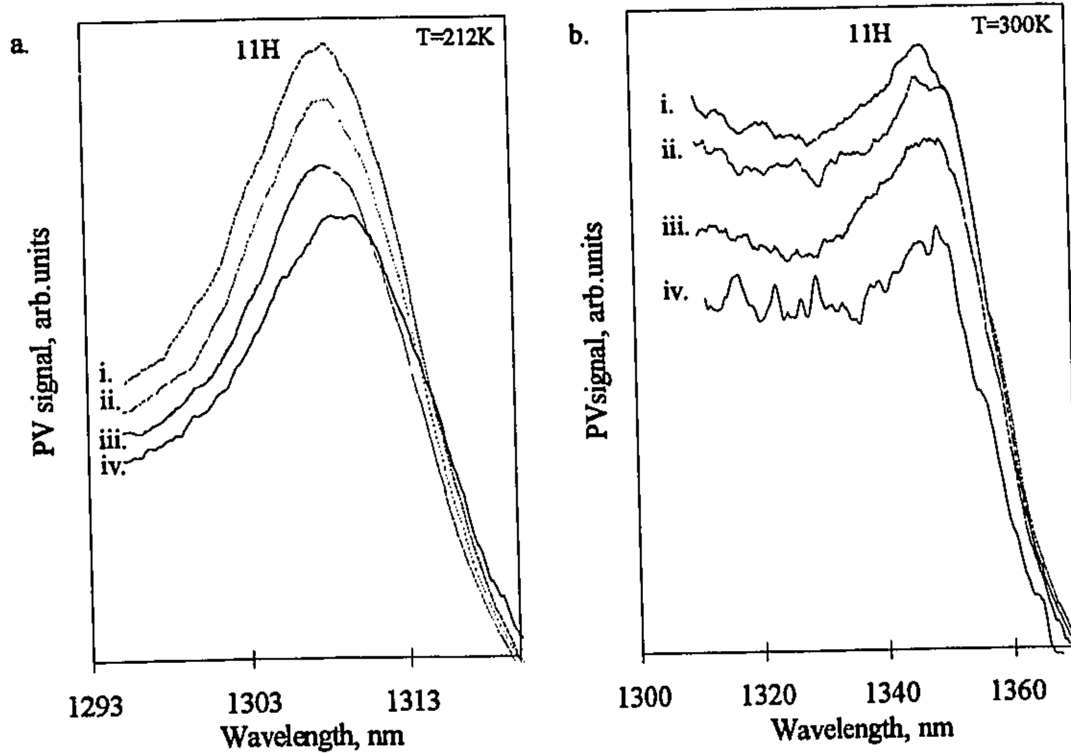

Fig. 4.26 The *11H* excitonic peak dependence on the pump beam intensity for sample 1: a.-212K and b.-300K; i-I=6mW/cm^2; ii-I=13mW/cm^2; iii-I=0.13W/cm^2; iv-I=1.3W/cm^2.

screening could be associated with a change in the internal electric field, defined in the sample by the Schottky barrier. In our case, the photoexcitation by the pump beam has the same effect as an applied positive D.C. bias in the direction opposite to the direction of the internal field of the sample, and as a result, the total field decreases. This process affects the photogenerated carriers and consequently the PV signal collected at the electrodes. At both temperatures, 212K and 300K, the PV signal follows an approximate exponential decay as the intensity of the pump beam increases. The position of the exciton peak for each intensity is measured and small red shifts of ≈1.2meV at 212K and ≈0.9meV at 300K are observed as the pump beam intensity increases from I=6mW/cm^2 to I=1.3W/cm^2. This shift is a consequence to the field induced absorption changes for photon energies close to the band gap energy. To evaluate the internal field changes,

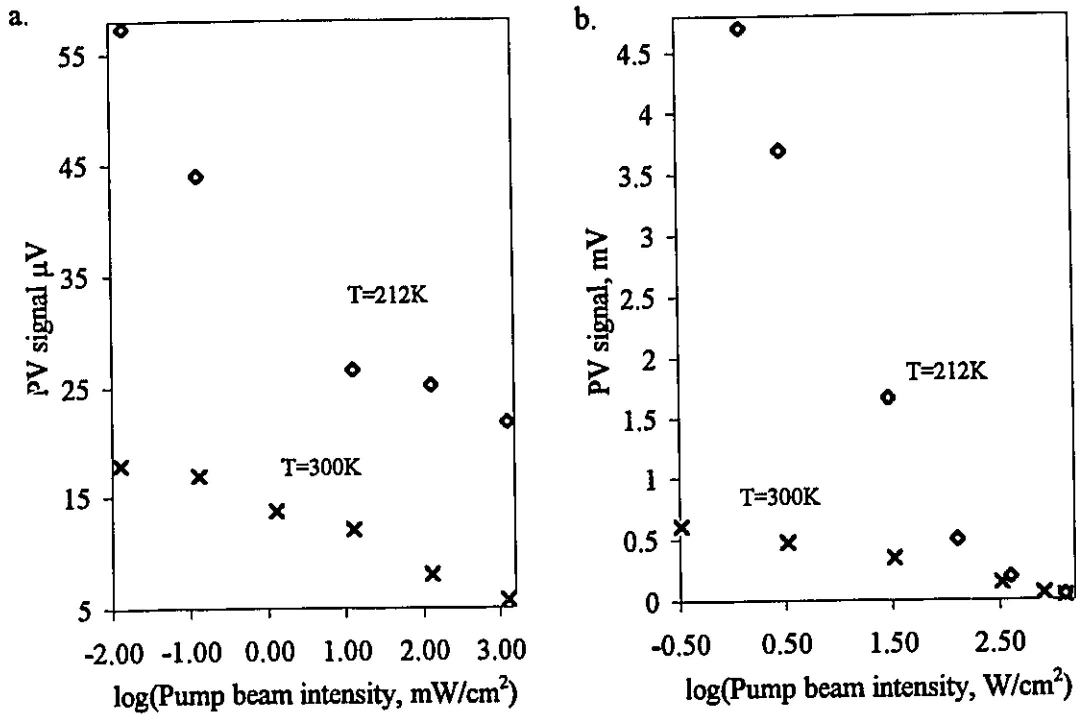

Fig. 4.27 PV signal dependence on the pump beam intensity for a.-sample 1 and b.-sample 2.

caused by the pump beam, the open-circuit voltage is measured, using the pump source - 10mW *He-Ne* laser. Log(PV) vs. Log of the relative illumination intensity at the two temperatures-212K and 300K is shown in fig.4.28a.. The values of the PV signal at the intensity saturation points correspond to applied positive voltages of 0.1V at 212K and 0.04V at 300K, and applied in eq.4.5 give field changes from F_0=5.3x10^{3}V/cm to F=3.8x10^{3}V/cm at 212K and from F_0=7.6x10^{3}V/cm to F=7.0x10^{3}V/cm at 300K. These changes are quite small and result in negligible shifts, due to the small modulation of the internal field[76]. The observed shifts of the ground state exciton to lower energies with the decrease the of internal field are in good quantitative and qualitative agreement with the ones measured previously, where the electric field dependence of the *11H* exciton peak was studied (section 4.3.1).

a.

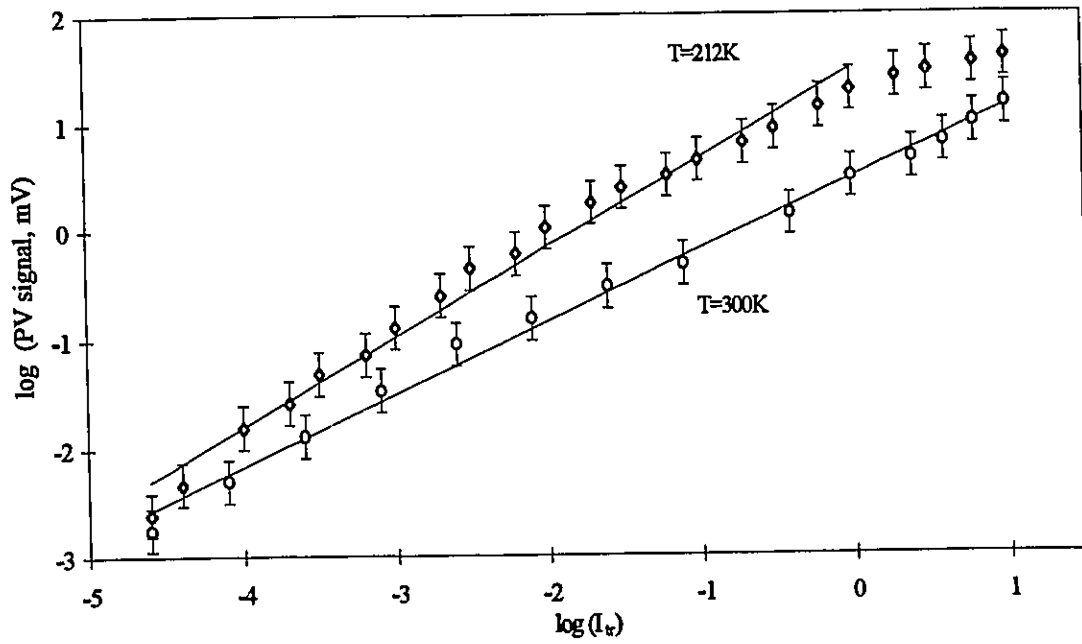

b.

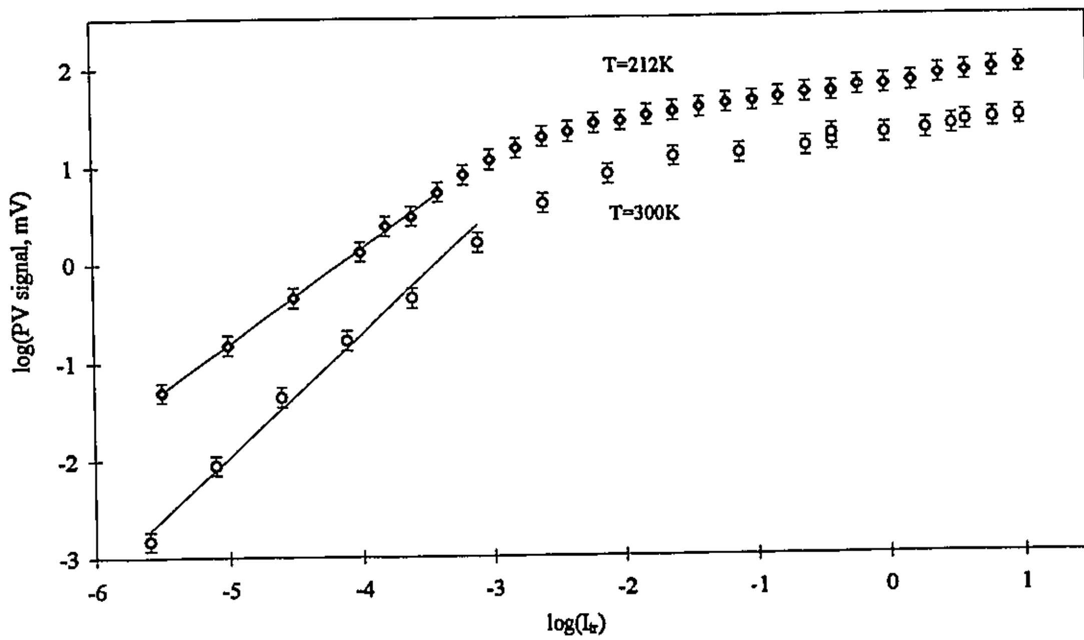

Fig. 4.28 The open-circuit PV signal vs. the illumination intensity $I_{tr}=I/I_o$, where I_o is the intensity given by 10mW *He-Ne* laser: a.-sample 1 and b.-sample 2.

The same type of experiment was conducted for sample 2 again at 212K and at 300K. The results shown in fig.4.29 represent the PV signal detected in the spectral region of the *11H* exciton peak. For clarity, the spectra are again equally displaced to each other without taking into account their real amplitude. The intensity of the second beam was varied between I=3mW/cm^2 and I=1.3W/cm^2. The actual decrease of the PV signal with the increase in the pump beam intensity is shown in fig. 4.27b. An approximate exponential decrease is recorded at both temperatures (more evident at 212K) indicating the nonlinear response of the sample beyond the pump beam intensity of I=1.5W/cm^2. Relatively large red shifts of ≈1.9meV at 212K and ≈0.3meV at 300K were measured. To evaluate the change of the internal field for sample 2, the open-circuit voltage was

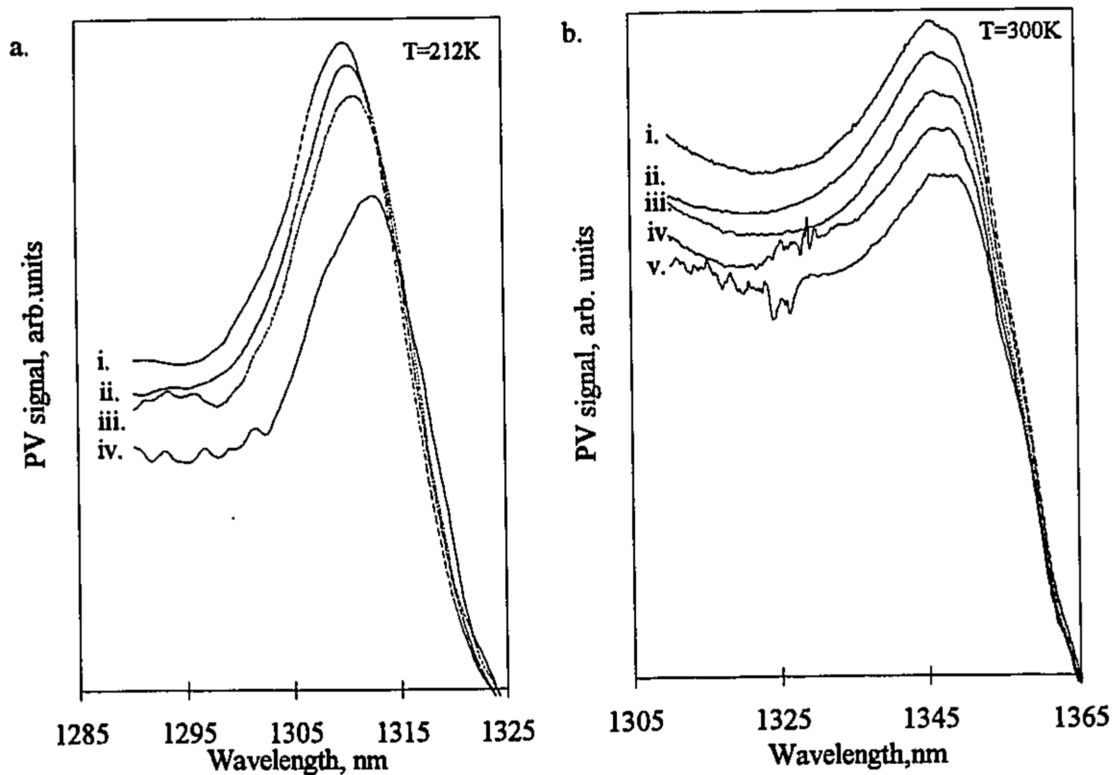

Fig. 4.29 The *11H* excitonic peak dependence on the pump intensity for sample 2: a.-212K; i-I=3mW/cm^2; ii-I=33mW/cm^2; iii-I=0.33W/cm^2; iv-I=.82W/cm^2 ; v-I=1.3W/cm^{2}and b.-300K i-I=3mW/cm^2; ii-I=13mW/cm^2; iii-I=0.41W/cm^2; iv-I=1.3W/cm^2.

measured again at both temperatures. The results shown in fig. 4.28b. correspond to applied positive voltages of 0.2V at 212K and 0.03V at 300K, or to internal field changes from F_o=7x10^{3}V/cm to F=4.1x10^{3}V/cm, at 212K and rom F_o=8.6x10^{3}V/cm to F=8.1x10^{3}V/cm, at 300K. The saturation of the open-circuit photovoltage occurs at lower intensity for this sample. This could be the reason for the larger screening of the PV signal and the relatively higher decrease in the field of the sample in the double beam experiment. The red shifts observed for sample 2 are again consistent with the electric field effects studied in section 4.3.

The shifts of the spectra observed in the above experiment are approximately the same that would be expected in simple heating of the sample by the pump beam; thus care had to be taken to determine if this shift has thermal origin. First, we calculated, that shift of 1.2meV for sample 1 and 1.9meV for sample 2, would correspond to a temperature change of 4K and 6K, respectively (using the temperature coefficient $dE_{g(InGaAsP)}/dT$=-3.4x10^{-4}eV/K). The temperature sensor was tested under the same conditions of illumination and no change of temperature caused by the pump beam was recorded. These reasons eliminate the thermal effects as cause for the observed red shift.

Summarizing the results presented in this section, we show that the D.C. photoexcitation of *InGaAsP/InP* MQWs has the potential for observing nonlinearities by effectively modulating their internal electric field. Illumination by pump beam in the PV geometry used here is an attractive non-contact method of studying field-induced effects in MQWs; in contrast to the external applied voltage technique of section 4.3.1, it introduces no additional noise to the PV signal.

Conclusions

In this study we carried out an extensive research into the opto-electrical properties of lattice matched *InGaAsP* quaternaries grown by Chemical Beam Epitaxy. We wanted to achieve better understanding of this system based on more experimental data and to correlate the obtained results for future practical applications in opto-electrical devices. We also studied the temperature and the electric field dependence of the *InGaAsP/InP* MQW features, as well as the photomodulation of the internal field of the samples .

The experimental data was collected by spectral observations on *InP* substrate, *InGaAsP* epilayer and *InGaAsP/InP* MQWs using the photovoltaic effect. We determined directly the barrier heights ϕ_B for the epilayer from the PV spectrum, and by applying a second technique (I-V measurements) ϕ_B for the MQWs. We found out that a thin interfacial insulating layer leads to enhancement of the barrier heights of the Schottky diodes. The features of the temperature-dependent PV spectra for the quantum wells were identified and all of them were found to follow the same temperature coefficients and their energy variation with temperature to differ by only the zero Kelvin energy. The application of a bias voltage to MQW samples, resulted in effects such as an increase in the collected PV signal, as well as quenching, broadening and ionization of the excitonic resonances. Contrary to the expected red Stark shifting, our observed shift at 212K was oriented to the higher energy side. We found that the changes in the carrier density induced by optical photoexcitation at milliwatt pumping power can influence the excitonic peak, even at room temperature and modulate the internal field of the heterostructure.

The development of sophisticated layered semiconductor growth technologies offers new opportunities for semiconductor physics and opto-electrical devices. For instance recent experiments have shown an 80% efficiency on biased MQW based solar cells[77] and almost 100% efficiency of *InGaAs/InP* MQW p-i-n laser structure operating

at 1.54μm[78]. The ability to produce structures that can confine excitons within dimensions less than its Bohr radius is one of the greatest achievements for this growth. Our present knowledge of the opto-electrical properties of lattice matched *InGaAsP/InP* MQWs is still far from being sufficiently complete, despite the important role this physical system has in device technologies. Although *InGaAsP* is still challenging for the optimization of the lattice match factor, it offers a wide range of band gaps and is a very suitable material for the construction of optical modulators operating in the infrared spectral region. With an appropriate design the internal field modulation of the *InGaAsP* quaternary system can be used in optical resonators or in pin MQW modulator devices.

References

1. G. A. Antypas, R. L. Moon et al., III-V quaternary alloys, Gallium Arsenide and Related Compounds, 1972, Institute of Physics, Bristol, Conf. series no.17, 48(1973).
2. H. Temkin, D. Gershoni, and M. B. Panish, Appl. Phys. Lett. 50, 1776 (1987).
3. IEEE J. QE vol.17 Special issue on quaternary compound semiconductor materials and devices-sources and detectors, 117-167; 217 (1981).
4. Y. Takanashi, M. Kawashima, et al. ,paper OQE80-13, Technical group meeting of IECE Japan, Optics and Quantum Electronics (1980).
5. R. Yeats and S. H. Chiao, Appl. Phys. Lett. 36, 167 (1980).
6. S. Chelles, R. Ferreira et al. Appl. Phys. Lett., 64, 3530 (1994).
7. R. J. Nicholas, A. M. Davidson et al., IEEE QE-17, 145 (1981).
8. S. J. Pearton, C. R. Abernathy et al., J. Appl. Phys. 74, 1610 (1993).
9. S. Juodkazis, M. Petrauskas et al., Phys. Stat. Solidi(a)140, 439 (1993).
10. B. Reid, R. Maciejko, and A. Champagne, Can. J. Phys. 71, 410 (1993).
11. K. Tappura, J. Appl. Phys., 74, 4565 (1993).
12. J. E. Zucker, I. Bar-Joseph et al., Appl. Phys. Lett. 54, 10 (1989).
13. S. Shim and E. H. Lee, Appl. Phys. Lett. 63, 2887 (1993).
14. K. Satzke and G. Weiser et al., J. Appl. Phys. 63, 5485 (1988).
15. M. A. Littlejohn J. R. Hauser, and T. H. Glisson, Appl. Phys. Lett., 30, 243 (1977).
16. S. Adachi, Phys. Rev. B39, 12612 (1989).
17. S. Adachi, J. Appl. Phys. 53, 8775 (1982).
18. R. E. Nahory, Appl. Phys. Lett. 33, 659 (1978).
19. S. Adachi, Physical properties of III-V semiconductor compounds, Wiley, New York, 1992.
20. T. P. Pearsall, Ed., *GaInAsP* Alloy Semiconductors, Wiley, New York, (1982).

21. K. Nakajima, A. Yamaguchi et al., J. Appl. Phys. 49, 5944 (1978).

22. J. A. Lahtinen and T. Tuoni, Phys. Status Solidi B130, 637 (1985).

23. L. L. Chang and L. Esaki, Physics Today, October, 36 (1992).

24. N. Schulman and Yia-Chung Chang, Phys. Rev. B31, 2056 (1985).

25. M. Jaros, K. B. Wong and M. A. Gell, Phys. Rev. B31, 1205 (1985)

26. G. Bastard, Wave Mechanics Applied to Semiconductor Heterostructures. Monographies de Physique, Les Éditions de Physique, Paris, 1988.

27. C. Fouillant and C. Alibert, Am. J. Phys., 62, 564 (1994).

28. A. Roth, Program for calculation the energy transitions of InGaAsP quaternary systems, 1994.

29. A. D'Andrea, R. del Sole, et al. ed., Optics of excitons in confined systems, Proceeding of the International Meeting, Giardini Naxos, Italy, 24-27 September 1991, Conf. Series no.123, Institute of Physics, Bristol, 1991.

30. D. S. Chemla, Helvetica Physica Acta, 56, 607 (1983).

31. J. O. Dimmock, Semimetals and semiconductors, vol.3, Optical properties of III-V compounds, Academic press, New York and London, (1967), p.276.

32. R. S. Knox, Theory of Excitons, Academic Press, New York, 1963.

33. S. Nikitine, Semicond. 6, 233 (1962).

34. N. Peyghambarian, S. W. Kosh and A. Mysyrowicz, Introduction to Semiconductor Optics, Prentice Hall, New Jersey, 1993, p.210.

35. C. Weisbush and B. Vinter, Quantum Semiconductor Structures, Academic Press, New York, (1991), p.71.

36. A. G. Milnes and D. L. Fencht, Heterojunctions and Metal-Semiconductor Junctions, Academic press, New York and London, (1972), p.171.

37. S. Sze, Physics of Semiconductor Devices, Wiley, New York, 1969, p.645.

38. P. Rochon, E. Fortin and J. C. Woolley, Can. J. Physics 55, 1145 (1977).

39. T. S. Moss, ed., Handbook on Semiconductors, vol.2, North-Holland, Amsterdam, 1980.

40. D. A. B. Miller, D. S. Chemla et al, Phys. Rev. B32, 1043 (1985).

41. R. T. Collins, K. v. Klitzing and K. Plog, Phys. Rev. B33, 4378 (1986).

42. M. G. Shorthose, A. C. Maciel et al., Appl. Phys. Lett. 51, 493 (1987).

43. E. Fortin, B. Y. Hua and A. P. Roth, Phys. Rev. B39, 10887 (1989).

44. K. Yamanaka, T. Fukunaga et al., Appl. Phys. Lett. 48, 840 (1986).

45. S. Fafard, E. Fortin and A. Roth, Phys. Rev. B47, 10588 (1993).

46. Y. Takahashi, Y. Kato et al., J. Appl. Phys. 76, 2299 (1994).

47. J. A. Brum and G. Bastard, Phys. Rev. B31, 3893 (1985).

48. G. Bastard, E. E. Mendez et al., Phys. Rev. B28, 3241 (1983).

49. Y. P. Varshni, Physica 34, 149 (1967).

50. D. A. B. Miller, D. S. Chemla et al. Appl. Phys. Lett. 41, 679 (1982).

51. M. A. Herman, D. Bimberg and J. Christen, J. Appl. Phys. 70, R1 (1991).

52. J. S. Escher, L. W. James et al., J. Vac. Sci. Technol. 13, 874 (1976).

53. H. Morkoc, T. J. Drummond, and C. M. Stanchak, IEEE Transaction on el. devices ED-28, 1 (1981).

54. P. K. Bhattacharya and M. D. Yeaman, Solid State Electronics ,296 (1980).

55. Z. Ouennoughi, K. Boulkronn et al. J. Phys. D27, 1014 (1994).

56. E. Fortin and A. Serpi, Solid State Comm. 85, 287 (1993).

57. S. Fafard, Ph. D. Thesis, University of Ottawa, 1992.

58. P. Rochon and E. Fortin, Phys. Rev. B12, 5803 (1975).

59. T. S. Moss, Photoconductivity in the Elements, Butterworth, London, 1952, p.31.

60. B. Y. Hua, E. Fortin, A. P. Roth, and R. A. Masut, Appl. Phys. Lett. 53, 1062 (1988).

61. Y. Wang, Ms. Sc. Thesis, University of Ottawa, 1992.

62. J. I. Pankove, Optical Processes in Semiconductors, Dover Publications. Inc., New York, 1971.

63. E. E. Mendez, F. Agulló-Rueda, and J. M. Hong, Phys. Rev. Lett. 60, 2426 (1988).

64. A. Hernández-Cabrera, P. Aceituno, and H. Cruz, Appl. Phys. 76, 4983 (1994)

65. G. Lafrenière, Ms. Sc. Thesis, University of Ottawa, 1994 p.51.

66. K. Gibb, C. Lacelle et al., Can. J. Phys., 69, 447(1991)

67. D. S. Chemla, Phys. Today, June, 46 (1993).

68. E. Garmire, Phys. Today, May, 42 (1994).

69. D. S. Chemla and D. A. B. Miller, Opt. Soc. Am. B2, 1155 (1985).

70. G. Bongiovanni, J. Moser and J. L. Staehli, Helvetica Physica Acta 62, 650 (1989).

71. H. Hang, Optical Nonlinearities and Instabilities in Semiconductors, Academic Press, San Diego, 1988.

72. J. M Wiesenfield and A. J. Taylor, Phys. Rev. B34, 8740 (1986).

73. S. Schmitt-Rink, D. S. Chemla and D. A. B. Miller, Phys. Rev. B32, 6601 (1985).

74. E. Hanamura, Phys. Rev. B38, 1228 (1988).

75. S. Malzer, H. Böhner, et al., Proceedings of Int. Semic. Conf., Vancouver, P1.106, 328(1994).

76. S. Malzer, N. Linder et al. Phys. Stat. Solidi (b)173, 459 (1992).

77. J. M. Mohaidat, K. Shum et al., J. Appl. Phys., 76, 5533 (1994)

78. S. Charbonneau, G. C. Aers et al., Appl. Phys. Lett. 63, 12 (1993).